Microstructural Characterization and Damage Detection in Steels with Linear and Nonlinear Ultrasonic Test

by

Niloofar Nabili Tehrani
B.Sc. (Iran University of Science and Technology) 2014

Thesis submitted in partial fulfillment of the requirements
for the degree of Doctor of Philosophy in Materials Engineering
in the Graduate College of the
University of Illinois at Chicago, 2019

Chicago, Illinois

Defense Committee:
J. Ernesto Indacochea, Chair and Advisor
Didem Ozevin
Sheng-Wei Chi
Matthew Daly
Reza Shahbazian-Yassar, MIE Department

To my *Dad*,

My Angel in the Sky

&

To my *Mom*,

My Angel on Earth

ACKNOWLEDGMENTS

First and foremost, I wish to express my deepest respect and sincere gratitude to my advisor, Professor Ernesto Indacochea for his constant encouragements, insightful guidance, and supporting me through all my ups and downs during my study at UIC. Not only he taught me the fundamentals of conducting scientific research, but also his advice enriched my life in many other aspects. I will forever be grateful for having the opportunity to learn from him.

I would like to extend my appreciation to my Doctoral Committee Members Professor Didem Ozevin, Professor Sheng-Wei Chi, Professor Matthew Daly, and Professor Reza Shahbazian-Yassar for their time to evaluate this work and their useful suggestions which definitely improved this dissertation.

Special thanks to my colleagues at UIC, Dr. Vineeth Kumar Gattu, Dr. Xin Chen, and Javier Obregon for their generous helps in taking SEM images and also their encouragements during my study. Thanks to Amir Mostavi for his efforts during our project and providing us with the raw data of the Nondestructive Testing.

I am thankful for my friendship and collaboration with Negar Kamali and Reyhane Abbasi, for their kind heart and their motivation to live a healthier life.

I am thankful for the friendship of all the amazing SWE UIC board and, especially Elsa Soto for all her help and support for making GradSWE UIC happen.

ACKNOWLEDGMENTS (Continued)

I am beholden to my friend, Mina, for being there for me from 10,445 kilometers away and for staying up all night to talk to me in the other side of the world whenever I needed her to unburden.

I am thankful, and always indebted to my aunt and uncle, Mahboube Haghighi and Farzad Ahmadpour, for their infinite support and encouragements before and after I started my Ph.D. studies in the United States. This journey would not be possible without their help and heart-warming presence.

And last, but certainly not least, I want to get all the words in the world together to thank my parents, and my little sister, Bahar, who selflessly encouraged me to pursue my life far away from them for a better future. My dad, whom I forever lost the chance to hug again, to write this dissertation, and my mom, who is my only reason to still rise above the hardest times.

CONTRIBUTION OF AUTHORS

Chapter 1 is a literature review including stating the problem in the non-destructive evaluation (NDE) field, the goals and objectives on how to approach this problem, and the explanation of the key concepts that have been used in this research. Chapter 2 represents two published manuscripts [1, 2] for which I was the second and third author. For both publications, Amir Mostavi contributed to the Ultrasonic testing and analysis of its results and Negar Kamali generated the numerical simulation data. My contribution to these two publications was related to the section of materials characterization and damage assessment and I played a major role in the writing of the manuscript along the other authors and our research advisors Prof. Didem Ozevin, Prof. Sheng-Wei Chi, and Prof. J. Ernesto Indacochea. The raw data acquired by Amir Mostavi helped me in generation of Figures 23-26, and 31. Chapter 3 represents a work under review in the journal of Materials Engineering and Performance for which I was the primary author and the major driver of the research. Reyhane Abbasi assisted me in the experiments related to the Ultrasonic testing and Acoustoelastic Coefficient measurements as well as writing the manuscript. Our research Advisors, Prof Ozevin and Prof. Indacochea, guided us through the writing of the manuscript. Chapter 4 represents a series of my own unpublished experiments related to the last damage type (creep damage) that was the subject of my research. This research will be published upon the completion of the manuscript for which I will be the primary author. Amir Mostavi assisted me in generation of the raw Ultrasonics data and Prof. Indacochea guided me through the writing of the manuscript. In Chapter 5, the

CONTRIBUTION OF AUTHORS (Continued)

summary and conclusions based on the previous chapters are presented. The future directions of this research are also discussed as a part of the last chapter.

ABSTRACT

The objective of this research is to study the potential of using nonlinear ultrasonic testing (NLUT) to detect damage early due to mechanical deformation or creep, as well as using it as a mean to assess microstructure changes. A comparison is also undertaken between the sensitivity of the NLUT (using nonlinearity parameter and acoustoelastic constant) and linear ultrasonic testing (LUT) technique (using wave velocity), for each damage type and microstructure assessment.

This investigation consists of three different parts. In the first part of the investigation, assessment of the mechanical damage in a single-phase metal, Al-1100, was conducted to associate the strain directly with the NLUT and LUT parameters. In the second part, both NDE techniques were correlated with changes in the microstructure of the alloy after heat treatments; an A572 steel was intercritically annealed at different temperatures to generate different volume fractions of ferrite and martensite. In the third part of this study AISI 410 stainless steel specimens were submitted to different levels of creep; such damage includes both mechanical straining and microstructure changes due to exposures to different creep times and total strains.

The results showed that the NLUT has the potential to detect the most minute changes in the microstructure with a sensitivity about 150 times more effective than LUT. However, using the LUT methods can still be beneficial in mapping the localized damage especially with the immersion techniques such as Scanning Acoustic Microscope. In the case of mechanical damage, the NLUT showed a continuous increase or decrease depending on the damage. For

the case of creep damage assessment more work is needed to interpret the results due to the complexity of this type of damage due to mechanical and microstructural changes that occur simultaneously. There needs to be caution when interpreting the results since several factors are influential, particularly the initial condition of the component before service.

TABLE OF CONTENTS

TABLE OF CONTENTS (Continued)

CHAPTER **PAGE**

TABLE OF CONTENTS (Continued)

CHAPTER **PAGE**

LIST OF TABLES

LIST OF FIGURES

LIST OF FIGURES (Continued)

LIST OF FIGURES (Continued)

LIST OF FIGURES (Continued)

LIST OF FIGURES (Continued)

LIST OF FIGURES (Continued)

INTRODUCTION

Linear ultrasonic testing (LUT) methods have been used traditionally to evaluate the materials condition by identifying the presence of various flaws such as cracks, corrosion, delamination in steel alloys [3–5] . Recent developments in UT methods e.g. high frequency non-linear ultrasonic and non-contact ultrasonic, have made it possible to assess the systematic evolution of damage of materials at early stages, such as in the case of fatigue and creep [6, 7]. Material components operating at different conditions and locations in existing structural systems, power plants, aerospace, petrochemical, and chemical industries have experienced premature failures that are often attributed to thermal degradation, fatigue, or creep [8–14]

Creep damage is a complex phenomenon related to metal degradation at high temperatures, particularly in ferrous alloys which is associated with both microstructural changes such as increases in grain size, carbide coarsening or dissolution, and plastic deformation [13]. This study assesses the sensitivity of both linear and nonlinear UT techniques to evaluate creep damage. More than a decade of research on the damage assessment with UT has demonstrated that this NDE technique is an important tool to detect microstructural and assess structural damage of components [15–18]. However, most of these investigations have been focused on fatigue damage detection, and less data is available on the applicability of UT for creep damage detection.

This investigation looks at three cases of damage assessment using linear and nonlinear UT. In the first instance plastic deformation is measured by means of UT inspection by mechanically

deforming Aluminum 1100 at room temperature by uniaxial testing, submitting the alloy to different levels of uniform uniaxial straining. This metal is single-phase, and it was selected in order to eliminate or minimize possible microstructural interference during the NDE measurements. In the second case, a high strength low alloy steel, A572, primarily used in highway bridges, was submitted to different heat treatments to introduce different volume fractions of pro-eutectoid ferrite and martensite. UT is then being used as a metallographic tool to assess the changes in microstructures and estimate the amounts of both phases. The changes in the microstructure of the steel alloy, as well as the variations in volume fraction of phases are correlated with the signal changes using linear and nonlinear UT. The third component of this investigation combines both the changes in microstructure and straining levels by focusing on creep. 410 stainless steel samples were submitted to different levels of creep damage at a constant load and elevated temperature with different degrees of straining, i.e., different creep times. 410 stainless steel has been selected for this portion of the study since this steel is used in many heat resistance applications such as steam and gas turbines, valves, and nozzles and hence is subjected to creep deformation. During the creep test some blank samples were also exposed to the same temperature and time of each specific creep test, in order to decouple the microstructural changes from microstructure-plastic deformation and thus studying the aging effects on the microstructure damage due to the high temperature and time exposure. Therefore, by knowing the sensitivity of the nonlinear UT to the minor changes in the microstructure, the underlying factors for the creep rupture in the 410 SS can be investigated.

INTRODUCTION (Continued)

This thesis contributes to the understanding of the sensitivity of linear and nonlinear ultrasonic (both with nonlinear parameter and acoustoelastic coefficient) techniques to evaluate the changes in microstructure and phase volume fraction, plastic deformation, and the combination of these two factors in terms of creep damage. In this investigation an acoustic microscope has also been used to assess the mechanical and creep damage by immersing the specimens in water and assessing the damage by linear UT. All the NDE results are verified with traditional destructive tests such as optical microscopy, SEM, XRD, and hardness testing.

This dissertation provides information on the background of the analytical NDE methods and experimental techniques used to introduce damage and/or microstructure changes to demonstrate the sensitivity of the UT techniques for progressive damage assessment. The organization of this dissertation is outlined as follows:

Chapter 1 presents the background on the significance of research on the nonlinear UT techniques as well as more advanced linear methods. The linear and nonlinear techniques that are used in this study are compared and explained in detail. Information regarding the previous studies on detection of different damage sources, both mechanical and thermal, with ultrasonic methods is also reviewed.

Chapter 2 examines the effect of plastic deformation in aluminum 1100 on the linear and nonlinear UT by considering the time of flight (TOF) and nonlinear parameter , respectively. The results obtained with NDE are confirmed by using optical microscopy (OM), scanning electron microscopy (SEM), X-ray diffraction (XRD), and hardness, as well as using an extensometer to monitor the strain during tensile testing.

INTRODUCTION (Continued)

Chapter 3 examines the use of UT as a tool to conduct metallographic analysis. An A572 steel was submitted to intercritical heat treatment to generate different phase volume fractions of martensite and ferrite. The effect of these different phase volume fractions on the wave velocity and acoustoelastic coefficient was studied. In depth investigation of the reasons behind the change in the UT results by the ferrite and martensite volume fractions is reported and has been proved by image processing techniques as well as hardness mapping.

Chapter 4 focuses on the combination of plastic deformation and thermal aging in the microstructure by submitting 410 SS samples to different levels of creep damage and assessing the damage via UT techniques.

Chapters 2, 3 and 4 starts with a brief introduction on the specific damage or microstructural feature in focus as well as the material used; continues with the experimental procedure followed to introduce the damage or microstructure changes as well as the NDE and destructive tests carried out; and ends with specific conclusions related to the subject investigated in each chapter.

The last chapter summarizes the important results and contributions of this work. Conclusions drawn from this investigation are also provided in this chapter, along with the scope of future work.

CHAPTER 1

BACKGROUND

1.1 Nondestructive Ultrasonic Testing: Importance and Challenges

A large number of thermal power plants around the world are over 50 years old and have exceeded their design lives of 100,000 hours and are subjected to aging from fatigue, creep, corrosion or a combination of them. These damage mechanisms can deteriorate the mechanical properties of components and shorten their lifespan [19, 20].

The components that are exposed to high temperatures for long duration of time become susceptible to creep damage. Energy saving, decrease in CO_2 emission, and improvements in thermal efficiency requires an increase in steam pressure and temperature which leads to even faster degradation in the material [21, 22].

In-situ assessment of the structures can play an important role in predicting the remaining life [22]. In addition, early creep damage detection is the key to prevent catastrophic failures and ensure safe and economic operations by scheduling opportune maintenance work [23]. Traditionally, creep damage in steels utilized in the power generation industry has been assessed by replica metallography which needs a meticulously polished and etched surface. Additionally, it only gives information about the direct surface state rather than the volumetric damage (such as creep) and can only analyze the tested spot [18, 19, 23]. Hardness testing is also another conventional method considered for creep damage detection, but these results can be affected

by the surface decarburization in an alloy steel or the local microstructural variations near the surface resulting from processing of the alloy. All these factors combine to yield deficiencies that will cause large scattering and poor reproducibility in the measurements that may lead to erroneous assessments [18]. The shortcomings of these methods and other traditional creep detection techniques have made the search for nondestructive testing necessary [18, 24]. The tendency to use Nondestructive evaluation (NDE) techniques to characterize microstructure, damage initiation and growth is growing every day due to its numerous benefits in performance monitoring of in-service components. In the past, NDE techniques have been used only to evaluate the current condition of the component, however over the past decades there has been a significant effort in using such tests as health monitoring tools and to predict the remaining life of structures or components. Many techniques have been advanced over the past decades to investigate the creep damage in materials nondestructively [21, 25, 26]. Among the different NDE methods, ultrasonic testing has been used to evaluate internal damage of components reaching greater depths due to improvements in instrumentation sensitivity and better data analysis and interpretation [21, 23, 27–32]. Figure 1 shows a typical creep curve and various destructive or nondestructive techniques that can be used for damage detection with their damage detection capability corresponding to different stages of creep. As can be seen in this figure, among all the techniques, ultrasonics is known to be the most sensitive technique to detect creep damage earlier [18].

Linear ultrasonic testing (LUT) has been a promising NDE technique in both lab and in-situ conditions, but its applicability in early damage detection for components under creep is still

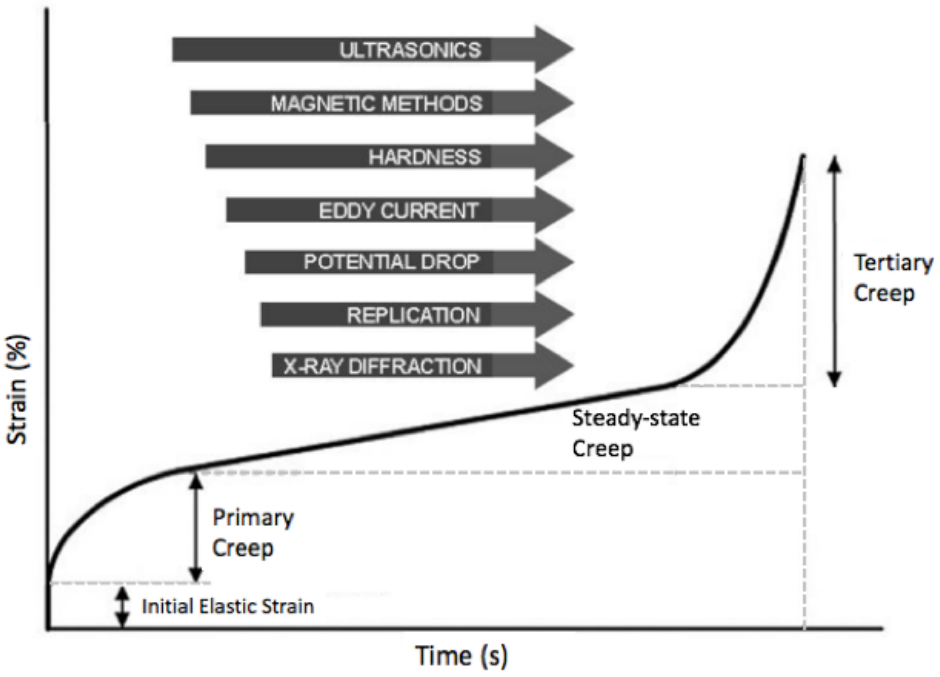

Figure 1. Typical creep curve with evolution of microstructural damage along with the various techniques studied.

questionable [22, 24, 33]. Linear ultrasonic techniques such as sound velocity and attenuation are based on the back-wall echo measurements from a contacting piezoelectric transducer. This technique can give averaged results over the thickness and can be used for volumetric creep detection [21, 24]. It has been reported that the increase in porosity and damage level of the components leads to a monotonic decrease in longitudinal wave velocity. However, the change in the velocity in the primary stages is in order of magnitude 0.1% which makes the in-situ detection of the damage difficult. This small change can be also attributed to the

inhomogeneity of the material even in one sample [24]. On the other hand, the formation of microcracks decreases the velocity to a greater extent, about 2-5%, and there are some claims that this method can give a quantitative estimate of porosity in the late stages of creep [24,34]. While it has been shown that the ultrasonic velocity is more sensitive than the attenuation, the limitation of these conventional ultrasonic methods is that the defect generated during the creep should be so obvious and large that the method can be sensitive to it and detect it. The problem becomes more pronounced when the creep damage is in the early stage and reveals in the form of microstructural changes [22, 33]. Therefore, the linear method may be insufficient for detection of localized creep damages.

It has been stated that nonlinear ultrasonics is more sensitive to the early stages of creep damage and can even detect the micro void nucleation and growth [22]. Ogi et al. [35] evaluated the effect of aging and fatigue damage on harmonic generation in precipitation hardenable 2024 aluminum alloy and found a good correlation between the remaining life and the surface wave nonlinearity. It has been shown that the nonlinearity detection in the material by ultrasonic has the potential of becoming the primary means of characterizing the creep damage since it is sensitive to the change in dislocation structure during the creep damage [21, 36].

The microstructure of the material and its changes with time is an important factor in service life calculation which depends on the type and thermal history of the alloy, thus it is necessary to evaluate the effectiveness of one technique for the specific material of interest. In addition, the majority of the previous research is focused on fatigue damage detection by linear and nonlinear techniques and fewer studies have been reported concerning creep damage.

1.2 Objectives

The objective of the proposed research is to predict the behavior of nonlinear ultrasonic waves due to creep damage in 410 SS. This model will be validated experimentally with microstructural characterization and finally, a correlation between the predictions and the experimental results will be made. Since creep damage is complicated due to both plastic deformation and microstructural aging occurring concurrently, it is important to first investigate the effect of each of these factors in simpler conditions and materials to prove the sensitivity of the technique to small changes. Three different damage or alloy conditions will be investigated using (non-contact) linear and nonlinear ultrasonics. UT evaluations were conducted by considering: (1) different damage levels due to plastic deformation at room temperature in a single-phase alloy (Al 1100), (2) production of ferrite and martensite microstructures of different volume fractions based on heat treatments without any stresses, and (3) creep damage by combining different levels of plastic deformation (i.e. different creep times) at an elevated temperature and constant load. For this last condition some samples were aged at the same temperature and same creep times without any applied load.

1.3 Nondestructive Ultrasonic Technique

Ultrasonic Testing (UT) is a well-established nondestructive evaluation (NDE) method that measures the material condition by monitoring the changes in the propagation of high-frequency elastic waves within the material. The frequency of the sound waves used in this method is above the audible range i.e. more than $\sim$ 20 kHz ranging from 0.1 to more than 15 MHz with the wavelengths ranging from 1 to 10 mm [37].

Any disturbance in one end of a solid cause a sound wave to travel through it in a finite time by vibrating the molecules, atoms, or particles in the material. However, the velocity of the propagating wave in the material depends on the medium, i.e., material type, microstructure, presence of defects, etc. Wave propagation in solids depends on the resistance of the atoms to vibration when a force is applied known as impendence (Z). The cracks, boundaries, and inclusions can be detected in the materials because of the different impedance between these defects and the material matrix. These defects can be located by the reflection, scattering or transmission of the waves [37].

There are two general testing methods that can be used to evaluate the presence of inhomogeneities in a material. Pulse-echo (PE) and through transmission are the most common techniques. The application of these methods depends on the accessibility to both or only one side of the specimen. Figure 2a shows PE method using only one transducer and access to only one side of the specimen. As is shown in this figure, the pulse is reflected either from a defect or the back wall of the sample. The defect gives rise to the signal before the rear surface reflection and by having the thickness and sound velocity in the material, the reflection time on the oscilloscope can be translated to the location of the defect in the bulk of the material. Figure 2b shows through transmission method which requires two transducers and access to both sides of the specimen. Figure 2c and d correspond to the angular reflection method and the transmission-reflection method requiring only one side of the specimen. In through transmission, the intensity of the signal is reduced in the presence of the defects which makes this method more capable of detecting smaller defects compared to the PE method. The capability

of ultrasonic wave to detect the defects depends on the wavelength, defect orientation and the beam diameter [37]. In addition, it is important that the coupling transducer-specimen should be very good to detect the smallest defects. Alternatively, the sample and the probe can be immersed in the water for the immersion test. In the case of the immersion inspection, the probe coupling to the specimen surface is maintained uniform by water which makes it easier to use complex shape specimens and results in increased sensitivity.

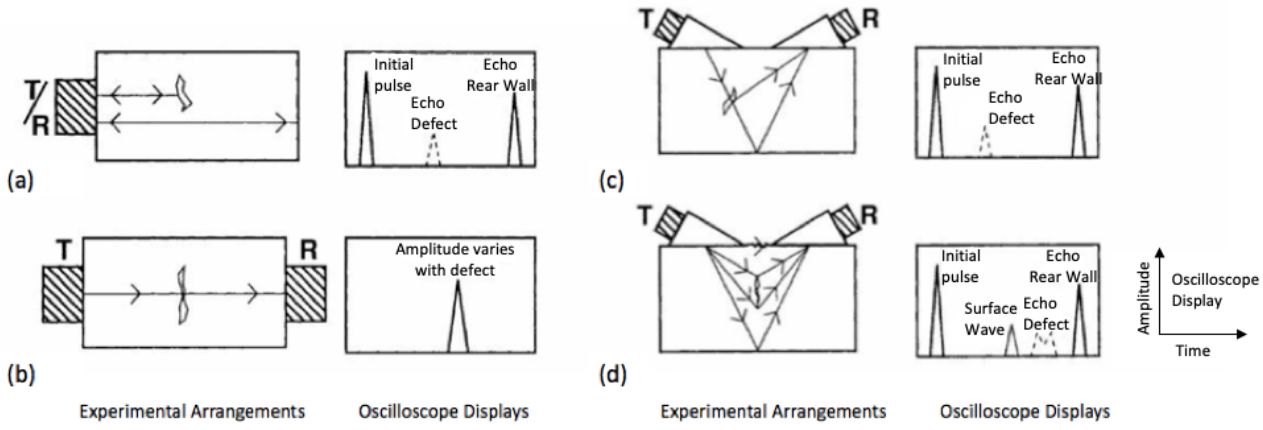

Figure 2. Ultrasonic test arrangements (a) Pulse echo technique (PE), (b) The transmission method, pulsed through-transmission, (c) Reflection method, (d) an alternative transmission-reflection crack tip diffraction technique. (Note: T, transmitter transducer; R, receiver transducer; T/R transmitter and receiver transducer) [37].

In addition to different testing methods, there are various types of waves that can propagate in the material. This includes the longitudinal, transverse, surface, Lamb, and Raleigh waves. In NDT, the longitudinal and the transverse wave modes are the most commonly used wave modes. If the oscillation of the particles is parallel to the direction of the sound propagation, it generates the longitudinal wave. In this wave mode, the energy travels through the material by compression and expansion movements. On the other hand, the oscillation perpendicular to the direction of the sound waves produces transverse waves. This wave mode requires an acoustically solid material for propagation and is relatively weaker than the longitudinal waves [38]. The schematics of the particle movement corresponding to the propagation of the longitudinal and transverse waves are illustrated in Figure 3.

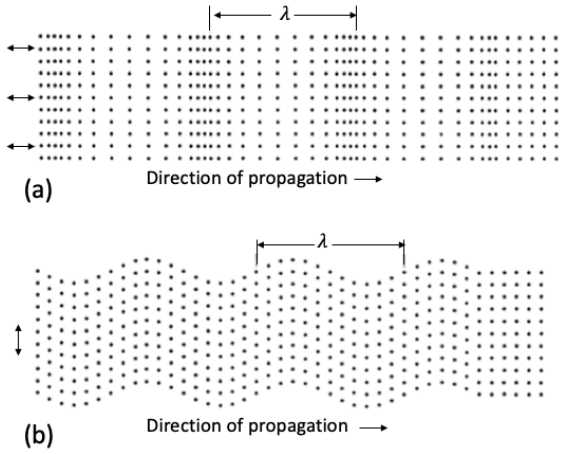

Figure 3. Wave modes (a) longitudinal wave, (b) transverse wave [38].

In the next sections, some fundamental theories on linear and nonlinear UT will be discussed.

1.3.1 Linear Ultrasonics

Linear Ultrasonic Testing (LUT) is one of the most traditional methods in NDE which uses the linear theory and is based on the wave properties such as velocity, attenuation, and transmission or reflection coefficients. These properties can be correlated to the elastic properties of the material and assist in finding the defects in it. It should be noted that in LUT, the transmitted and received signal have the same frequency, but different phases or amplitudes will be generated based on the defects present [39, 40].

1.3.1.1 Wave Velocity

Ultrasonic wave velocity depends on the physical properties of material such as density and the elastic modulus i.e. the microstructure [24, 41]. This can be explained by Newtons second law and Hookes law. According to the Newtons second law, force will be balanced by the particles mass and its acceleration ($F = ma$). In addition, Hooks law shows the relation between the restoring force, the spring constant and displacement($F = -kx$). The applied and the restoring forces are equal which leads to $ma = -kx$. Since k and m are constant for any given material, a and x will be directly proportional and the force does not have any impact on the time that it takes for the particle to move and goes back to the equilibrium condition. Therefore, the sound velocity in the material is independent of the applied force. However, m is related to the density of the material and k depends on the elastic constants of the material [41]. Therefore, the wave velocity for the longitudinal wave (V_L) can be written as:

$$V_L = \sqrt{\frac{C_{ij}}{\rho}} \tag{1.1}$$

where C_{ij} is the elastic constant of the material including E (Young's Modulus) and ν(Poisson's ratio) and ρ is the material's density. λ and μ are the Lame's constants which are derived from E and ν. It should also be noted that wave properties such as the wave mode, wave polarization, propagation direction, and the applied stress can also affect the wave velocity [18]. Therefore, the ultrasonic velocity can be re-written as Equation 1.2 and Equation 1.3 for longitudinal and shear wave, respectively [42]:

$$V_L = \sqrt{\frac{E}{\rho}\frac{1-\nu}{(1+\nu)(1-2\nu)}} = \sqrt{\frac{\lambda+2\mu}{\rho}} \tag{1.2}$$

$$V_T = \sqrt{\frac{E}{2\rho(1+\nu)}} = \sqrt{\frac{\mu}{\rho}} \tag{1.3}$$

Shear wave velocity is usually half of the longitudinal wave velocity. For surface waves, the motion is the combination of both longitudinal and shear waves.

The other important concept is the frequency, wavelength, and velocity relation in ultrasonic waves which is shown in Equation 1.4:

$$\lambda = \frac{C}{f} \tag{1.4}$$

Where λ = wavelength, C = velocity, and f = frequency. Since the velocity in a certain material only depends on its own properties and the wave mode, it can be inferred from this equation that the wavelength decreases by increasing the frequency [37, 42]. It has been mentioned in the literature that the defect size should be larger than one-half of the wavelength in order to have a high chance of being detectable. Increasing the frequency can increase both sensitivity and resolution of defect detection. However, increasing the frequency more than a certain level, can impose negative effect which depends on the material grain structure, thickness, and the defect characteristics. As the frequency increases, the penetration power of the wave reduces which reduces the chance of deeper flaws to be detected [41].

Although ultrasonic wave velocity is usually used in NDT of materials, Time of Flight (TOF) is usually the measured value which carries information about both velocity and the thickness of the sample. When the precise value of thickness or velocity in a certain material is known, the other can be easily calculated. Thus, it is important to separate the velocity and thickness contribution to TOF change. This is important when the damage includes plastic deformation and the thickness varies spatially or it is not known precisely [43].

1.3.1.2 Wave Attenuation

When the wave propagates in the material, its intensity can be reduced by distance which can be measured as a loss of amplitude or energy [19]. The mechanisms of energy loss can be categorized as absorption and scattering [37, 44]. Scattering can be explained as the sound reflection in directions other than its original propagation direction and can be triggered by grain boundaries, voids, inclusion, second phase particles and micro and macro cracks. On the

other hand, absorption refers to the conversion of the sound energy to other forms of energy and can happen due to the dislocation damping, magnetic domain damping and thermoelastic interactions [41, 44]. Over the years, attenuation has been used as a measurement tool to investigate the physical or chemical properties of the materials. However, there are some drawbacks on using the wave attenuation for creep or fatigue damage detection. This is due to the high sensitivity of the wave attenuation to small difference in grain size compared to the wave velocity [18]. The other drawback of this method, especially in the conventional contacting methods, is the high background noise that can decrease the sensitivity to small microstructural evolution. The mechanical contacts in the contact UT methods are essential for wave propagation in the sensors, couplant, and the material which leads to large absorption of the acoustic energy [19].

1.3.2 Nonlinear Ultrasonics

In LUT, the wavelength of the ultrasonic signal should be smaller than the size of the defects in order to detect them. This requirement limits the capability of linear UT to assess the material condition involving microstructural defects such as early stages of fatigue and creep damage. For example, in one of the previous studies on the fatigue crackdetection with LUT [6], it has been reported that the smallest crack that can be detected by this method is about 1 mm (1/32 inch) which is large enough to cause a failure before any preventive action can be taken. However, when there are some microscopic nonlinearities even in the early stages of the damage in the material, its strength would be degraded. These early stage nonlinearities are in sub-micron scale and may be even smaller than the ultrasonic wavelength in the frequently

used in the linear ultrasonic measurements and makes the utilization of the nonlinear ultrasonic necessary [28]. Therefore, despite of LUT capability to detect cracks, voids, or inclusions, it has some deficiencies in detecting small damage prior to the crack initiation [45]. On the other hand, further advancement of UT instrumentation and nonlinear wave propagation theory made the investigation on microstructural defects possible [15–17, 19, 46]

Originally, the nonlinear ultrasonic technique was used to determine the third-order elastic moduli of single crystals [33]. However, in the last decades, the focus has been shifted to its applications for nondestructive evaluation of degradation in engineering materials especially the mechanical properties [7] such as precipitation hardening in aluminum [47], or the diffusion bond integrity in copper alloys [48], etc.

The theory behinds the nonlinear acoustics is based on the nonlinear theory of elasticity developed by Murnaghan [49] which shows that there are three independent "third order" elastic constants (Murnaghan's constants) in addition to the two "second order" elastic constants (Lame's constants).

Based on the Murnaghan's theory, there are two methods to measure the material nonlinearity using nonlinear acoustic effects: the stress-dependent ultrasonic wave speed known as acoustoelasticity [44–47] and the detection of higher harmonics [18, 39, 50–53]. These two techniques are shown to be sensitive to the minute changes in the microstructure such as the increase in dislocation density and other subtle lattice imperfections that may not be detectable with conventional linear ultrasonic methods [18].

1.3.2.1 Acoustoelasticity

Acoustoelasticity constant (AEC) is a well-studied subject with a wide range of applications in nonlinearity detection in metals [26, 54–58]. Acoustoelasticity theory explains the change in the wave velocity when it propagates through the stressed material based on the relation between the nonlinear elasticity [49] and the elastic plane waves [59–61]. In order to obtain the AEC, wave velocity is measured while the structure is under the stress [26, 57, 62–64]. This is due to the fact that the stresses in the material affect its elastic, mechanical, and acoustic behavior. Therefore, when the ultrasonic is propagated in the stressed volume, its velocity and attenuation can vary based on the amount of the stress [55]. However, the magnitude and the nature of this variation can be influenced by the wave mode [26, 65], direction and polarization [61], frequency [58], and temperature [66, 67].

One of the most important applications of the acoustoelastic method is to determine the residual or applied stresses in a component. There are several advantages associated with this method compared to the other methods (e.g. X-ray diffraction, and magneto-elastic methods) such as deeper penetration for stress evaluation, easier in-situ testing arrangements, etc. However, it should be noted that the change in the ultrasonic velocity is only about 0.001% for each MPa of applied stress. Thus, precise measurement of the velocity is necessary to obtain the acoustoelastic coefficient [60, 64].

In the case of a homogenous isotropic material under uniaxial stress, the longitudinal and transverse wave velocities propagating in the direction of the applied stress are [55, 59, 61, 68, 69] defined as:

$$V_L^\sigma = V_L^0(1 + K_L\sigma) \tag{1.5}$$

$$V_T^\sigma = V_T^0(1 + K_T\sigma) \tag{1.6}$$

where, σ is the applied tensile stress, V_L^0 and V_T^0 are the velocities in unstressed state as specified in Equation 1.2 and Equation 1.3, respectively. K_L and K_T are introduced as the longitudinal and transverse acoustoelastic coefficients, which based on the wave velocity in the stressed-medium can be written as:

$$K_L = \frac{1}{2(\lambda + 2\mu)(3\lambda + 2\mu)}\left[\frac{\lambda + \mu}{\mu}(4\lambda + 10\mu + 4m) + \lambda + 2l)\right] \tag{1.7}$$

$$K_T = \frac{1}{2\mu(3\lambda + 2\mu)}\left[4\lambda + 4\mu + m + \frac{\lambda n}{4\mu}\right] \tag{1.8}$$

where, λ and μ are Lame's elastic constants, l, m ,and n are Murnaghan's third order elastic constants.

When the material under uniaxial tensile stress, the acoustoelasticity coefficient K is negative, showing the decrease in the wave velocity with increase in stress [55].

The velocity is indirectly measured by time of flight change when the distance between transmitter and receiver is constant for stress-free and stressed states, such that Equation 1.5 or Equation 1.6 can be rewritten as:

$$t_0 = t_\sigma(1 + K\sigma) \tag{1.9}$$

Different types of ultrasonic waves (longitudinal, Lamb, or Rayleigh waves) can used to determine the acoustoelastic coefficient by applying an ultrasonic wedge adjusted to different angles (e.g., the first or second critical angle) as shown in Figure 4.

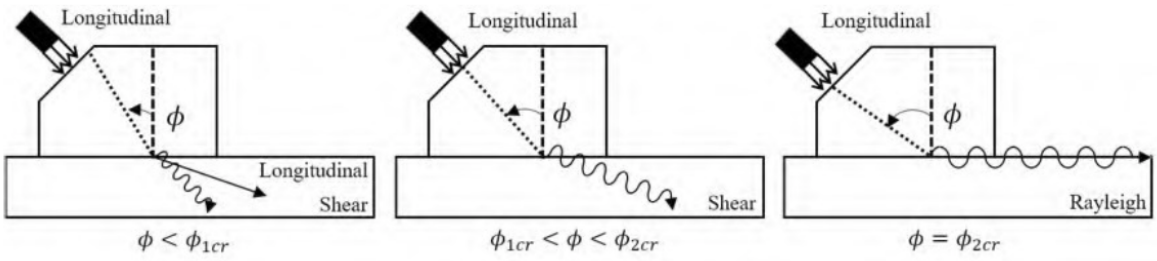

Figure 4. Various wave mode generation for (a) incident angle smaller than first critical angle, (b) incident angle between two critical angles, and (c) incident angle equal to second critical angle.

In the case of Lamb waves propagating in a plate with finite thickness, depending on the product of excitation frequency and thickness, the dispersion curves can be used to determine the acoustoelastic coefficient. For high values of frequency and thickness, the velocity converges

to the Rayleigh wave velocity for the first symmetric and antisymmetric modes, and for the higher modes it converges to shear velocity. In the case of bulk waves, it has been shown that the longitudinal waves are more sensitive to changes in the wave velocity upon mechanical loading [55].

As mentioned before, the ultrasonic velocity in a stress-free medium only depends on the second order elasticity constants, while the ultrasonic velocity in a stressed medium depends on the second and third order elasticity constants.

1.3.2.2 Higher Harmonics

Harmonic generation is another effect of nonlinear acoustics in which, energy of the wave traveling with the frequency of the transmitted wave is pumped into the second and higher harmonics [53].

The higher harmonics can be due to the lattice anharmonicity or to the microstructural defects [45]. Cantrell et. al [70, 71] and Kim et. al. [72] showed a direct correlation between acoustic nonlinearity and the accumulated plasticity or straining in a metal. This accumulated plasticity can be a quantitative evaluation of the amount of damage in the metal and it can be induced by a monotonic or a cyclic loading. The acoustic nonlinearity can be measured in the form of higher harmonics and it is shown to be sensitive to subtle damages occurring at an early stage even when there is no significant change in the linear ultrasonic properties such as velocity and attenuation [6, 7, 46, 72]

One of the most important advantages of this method over the acoustoelastic coefficient measurements is that it does not need an applied stress which makes it much more practical.

It can also be used at temperatures other than the room temperature [73]. Therefore, it is easier to handle and has the potential to be utilized in the field applications in future [74]. In higher harmonics nonlinear UT, a single frequency wave (excitation frequency) with a finite amplitude propagates inside the material. Upon the existence of microstructural defects inside the material, this single-frequency wave will interact with them and generates higher-frequency components called higher harmonics. The excitation frequency is called the fundamental wave frequency and the higher harmonics are integer multiples of the excitation frequency. In nonlinear UT, a sinusoidal excitation signal is utilized to have a narrower bandwidth of frequency in the solution, while in linear ultrasonic a pulse signal is usually used. In the case of instrumentation, the transmitting and receiving transducers are both tuned to the same frequency in linear ultrasonic. However, in nonlinear ultrasonic the receiving transducer should be tuned to the second or third harmonic frequency of the transmitting transducer to detect the weak nonlinearity due to the microstructural defects. The nonlinearity will then be quantified by monitoring the amplitudes of higher harmonics and can be correlated to the level of damage inside the material microstructure [2, 73]. To extract the amplitudes of the fundamental and second harmonic frequencies, the most common signal processing method is to transform the time domain signal into the frequency domain by fast Fourier transform (FFT) and read the amplitude of each frequency from the frequency spectrum [38–41]. Usually, the nonlinearity is explained based on measuring the acoustic nonlinearity parameter (β), which is given in Equation 1.10 [28, 33, 62, 75, 76].

$$\beta = \frac{8A_2}{A_1^2 x k^2} \tag{1.10}$$

in which x is the propagation distance, k is the wave number, and A_1 is the fundamental amplitude while A_2 is the second harmonic amplitude. Since the frequency and the transmitting distance is fixed for the transmitted longitudinal wave, the equation can be simplified to A_2/A_1^2, the ratio of the second harmonic amplitude A_2 to the square of the first harmonic (fundamental frequency) amplitude A_1 [6, 28, 76, 77].

Various wave types can be utilized for detecting microstructural damage using NLUT such as longitudinal waves [76, 78, 79], Rayleigh waves [52, 80, 81], or Lamb waves [45]. Longitudinal waves (bulk wave) are used to assess the defects along the thickness of the specimen and Rayleigh waves (surface wave) can test the specimen along its gage length [74].

There are several applications of nonlinear ultrasonics to assess microstructural changes in metallic alloys, such as fatigue damage [45,82] creep damage [22,28] [79], radiation damage [52], thermal aging [11,83], and cold work [84]. Baby et al. [22] showed that there is a good agreement between the second harmonics and the data obtained from metallographic studies in titanium alloys. In general, the acoustic nonlinearity parameter rises with an increase in the density of microscopic heterogeneities, e.g., dislocation density, precipitates, or porosity.

1.4 Creep Damage

Creep damage, a time dependent plastic deformation of metal alloys exposed to both high temperature and mechanical load, is a critical issue in the design and remaining life assessment of the components in the power generation industry [24, 85, 86]. Creep deformation drew atten-

tion because of the demand for higher operating temperatures in electricity generating plants, chemical installation, and aero engines. Thus, there is an urge among these industries to have new alloys with improved high-temperature properties, but also resistant to degradation in harsh environments and elevated temperature for long periods of times up to, or even higher than their designed lives [13, 21, 85].

In the creep process, grain boundary sliding leads to dislocation or wedge cracks which is a source of cavity nucleation. These cavities, later form micro voids which align themselves orthogonally or sometimes in 45° with respect to the applied stress [18, 86, 87]. At the end, the coalescence of these micro voids leads to the formation of micro cracks and macro cracks, and eventually failure [7, 87, 88]. The simultaneous microstructural change and strain accumulation makes the creep deformation one of the most dominant sources of failure in high-temperature applications [21].

Detection of creep damage in early stages is critical since propagation and growth of the cracks can happen so quickly that failure occurs unexpectedly. If the component is under uniform mechanical and thermal stresses, the creep mode will be a volumetric creep which means the damage will be widespread and multiple cracks may be generated within a relatively large area. However, there may be some critical locations such as stress concentration sites or pre-existing defects regions which require a close monitoring to prevent the failure. For example, premature creep may happen in weldments due to localized creep [24] that may occur as a result to the elevated temperatures associated with the welding process.

The basic information that can be derived from a simple creep test is to record the changes in the sample strain with time at a constant temperature and load. The total strain is the sum of the initial strain on loading and the creep strain over time as shown in Equation 1.11 and Equation 1.12.

$$\varepsilon_0 = f_1(\sigma, T) \tag{1.11}$$

$$\varepsilon_c = f_1(t, \sigma, T) \tag{1.12}$$

In addition, creep behavior can be described by variations in creep strain rate during time as [85]:

$$\dot{\varepsilon_c} = f_3(t, \sigma, T) \tag{1.13}$$

The creep temperature for any alloy is related to the metals melting temperature, as the ratio of T/T_m, where T is the creep temperature and T_m is the melting point of the material. The same normalization can be done for the stress level, by dividing the creep stress to the elastic modulus of the desired material to have a reliable comparison between the strength of different materials [85].

When the creep temperature is lower than the temperature needed for diffusion ($<0.3T_m$) and the stress is higher than the yield stress, the material experiences some strain hardening and dislocation movement until the flow stress becomes equal to the applied stress. In these

low temperatures, dislocations can only overcome short-range obstacles and the instantaneous strain of the sample includes both elastic and plastic deformation. The instantaneous strain magnitude can be determined from the stress-strain curve of the material while the subsequent time-dependent strain follows a logarithmic equation. The overall strain can be represented by the logarithmic relation shown in Equation 1.14, thus creep rate which corresponds to the derivative of this equation will decrease continuously with time. The overall strain will stay so low that it does not lead to fracture (Figure 5a). In this equation, ε_1 and t_0 are constants [89].

$$\varepsilon = \varepsilon_0 + \varepsilon_1 \left[ln(t + t_0)\right]^{\frac{2}{3}} \tag{1.14}$$

On the other hand, for creep temperatures above $0.4T_m$, the creep curve does not follow a logarithmic form and is in the form of a strain-time plot with three regions corresponding to three different stages of the creep, as shown in Figure 5b.

In this case, the creep curve will have an instantaneous strain upon loading at the beginning of the creep after which, the creep rate decreases gradually. This decrease is due to the strain hardening mechanism which slows down any strain brought about by temperature softening of the material due to an instant recovery or dynamic recrystallization. This stage is known as primary creep. The primary stage ends when the steady state rate is reached in the secondary stage of creep. The secondary stage of creep is known as the longest stage in which the plastic flow of the material is slow but constant (κ). This stage of creep often obeys the following relation [90]:

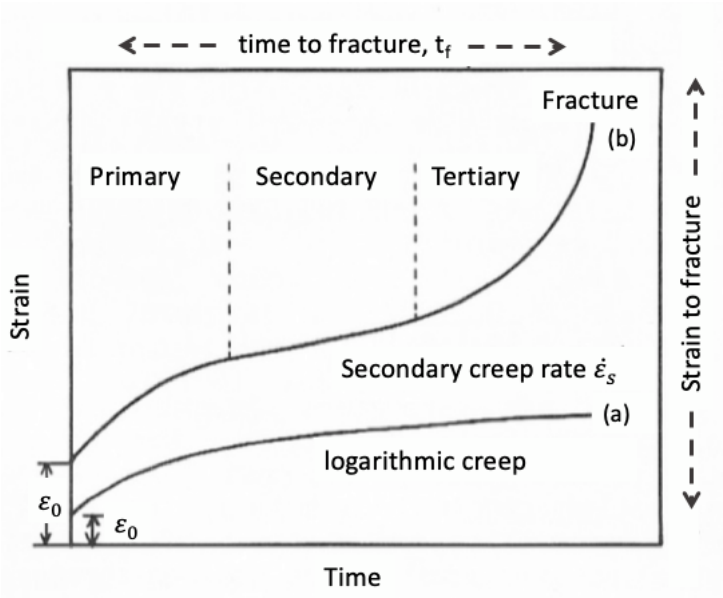

Figure 5. Schematic representation of the strain/time curves in (a) logarithmic creep at low temperatures and (b) creep at temperatures above $\sim 0.4T_m$ [85]

$$\varepsilon = \kappa t \tag{1.15}$$

where ε is the strain and t is the time under high temperature and stress. In this stage of creep, the rate of recovery i.e. the decrease in strength $(d\sigma/dt)$ is fast enough to balance the work hardening rate $(d\sigma/d\varepsilon)$. If $\boldsymbol{r}$ is the rate of recovery and $\boldsymbol{h}$ is the work hardening rate, then the strain rate at the steady-state becomes:

$$\frac{d\varepsilon}{dt} = (\frac{d\sigma}{dt})/(\frac{d\sigma}{d\varepsilon}) = \frac{r}{h} \tag{1.16}$$

The recovery process happens when the dislocations are able to escape the tangled or piled-up regions controlled by the rate of dislocation climb. Dislocation climb itself, is dependent on stress and temperature as shown in Equation 1.17 [86, 90, 91]:

$$r = A(\frac{\sigma}{E})^p D = A(\frac{\sigma}{E})^p D_0 exp[\frac{-Q}{kT}] \tag{1.17}$$

In this equation, D is the diffusion coefficient, which is defined based on Arrhenius equation, Q is the activation energy for steady-state creep (which is related to self-diffusion), T is the temperature, k is the Boltzmann constant, σ is the applied stress, and E is the Young's modulus. The higher the stress level, the closer the dislocations are which leads to the increase in recovery rate. Dislocation climb phenomena will be explained further in 1.4.1.

In addition, the work hardening rate, $\boldsymbol{h}$, decreases compared to the initial rate h_0 by increasing stress as follows:

$$h = h_0(\frac{E}{\sigma})^q \tag{1.18}$$

if $B = \frac{A}{h_0}$ nad $n = p + q$, then the strain rate in the steady-state stage of the creep is summarized as:

$$\dot{\varepsilon}_{ss} = \frac{r}{h} = B(\frac{\sigma}{E})^n D \tag{1.19}$$

The creep rate in the steady state region is the minimum strain rate in the entire creep process which is usually chosen as the material's representative in certain creep conditions [85].

However, it will not continue indefinitely, and the creep rate starts to increase again at some point and enter the tertiary stage and eventually fails. In this region, several independent mechanisms such as recrystallization, grain growth, precipitate coarsening, and cavity formation are responsible for the increase in creep rate. The tertiary stage can also be accompanied by necking and/or crack development which eventually leads to failure of the piece. The creep strain can be large at the end of creep and as the temperature or stress increase, the rupture life decreases [24, 85].

Although the general shape of the creep curve is known, there might be several variations in practice and that is why there is no general agreement on constitutive equations to describe the strain change as a function of stress and temperature. Therefore, actual creep measurements up to a certain strain or time are required for design and quality purposes for every specific condition.

Generally, there are three main approaches to determine the remaining life of a component under creep conditions including calculation techniques based on the thermal-mechanical history of the component, accelerated creep rupture test, and non-destructive evaluation techniques (NDE). One of the drawbacks of calculation method is that it does not consider the environmental effects such as oxidation and oxide build-up which ends up in large errors in creep life calculation. The other method, accelerated creep rupture test, can only be used for a limited number of samples and the extrapolation of the laboratory data needs great care since the lab results cannot always represent the real stress and temperature conditions. The last technique used to detect the creep damage, is nondestructive evaluation of the damage which

takes place by continuously or periodically monitoring the component to detect the presence of any voids or cracks. Since the alloy type and its thermal history can play an important role in microstructure variations, each technique needs to be evaluated for its effectiveness for a certain type of material under tspecific service conditions [24].

In order to evaluate the results of NDE technique after the creep damage, it is important to have a more detailed understanding of the controlling mechanisms during the creep damage. There are several basic mechanisms that govern creep in materials including (i) dislocation slip (glide), (ii) dislocation climb, (iii) grain-boundary sliding, (iv) diffusion flow cause by vacancies. Depending on the creep conditions (temperature and stress) and the material, one or a couple of these mechanisms may contribute to the damage evolution [7, 92]. Fig shows an Ashby-type deformation mechanism map for a range of stresses and temperatures and a constant grain size. This diagram is based on the applied stress (σ) divided by shear modulus (μ) and the temperature (T) divided by melting temperature (T_m). Using this map, the creep mechanism(s) explained below can be predicted for a specific material at certain creep conditions [93].

1.4.1 Dislocation Creep

Dislocation slip (glide) and dislocation climb mechanisms are both under the general category of "Dislocation Creep" with some differences. Dislocation slip in a crystalline material is defined as the movement of dislocation in which, one part of the dislocation moves one lattice point along the slip plane. Dislocation slip contributes to the overall creep deformation and requires the bonding between the atoms to be broken for the dislocation to move. This creep mechanism can occur in all temperature ranges from absolute zero to melting temperature with

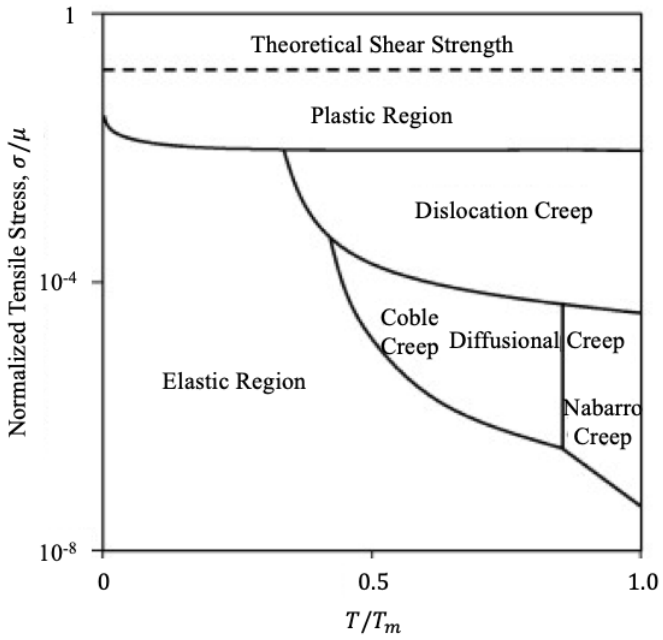

Figure 6. Ashby-type deformation mechanism map [93]

more pronounced contribution at higher temperatures. However, less stress is required for the dislocation creep at higher temperatures. It has been reported that the stress required for the dislocation slip is about one tenth of the theoretical shear strength ($\sim G/10$) [92,94]. Figure 7 shows the schematic of the dislocation slip in a crystal.

At lower stresses, the creep rate is governed by the rate of dislocation climb over the obstacles which itself depends on the vacancy diffusion [92]. There are usually many obstacles on the way of dislocation motion which is the basis of strengthening mechanisms in metals. However, as mentioned in section 1.4 and Equation 1.16, recovery process happens when the metal is

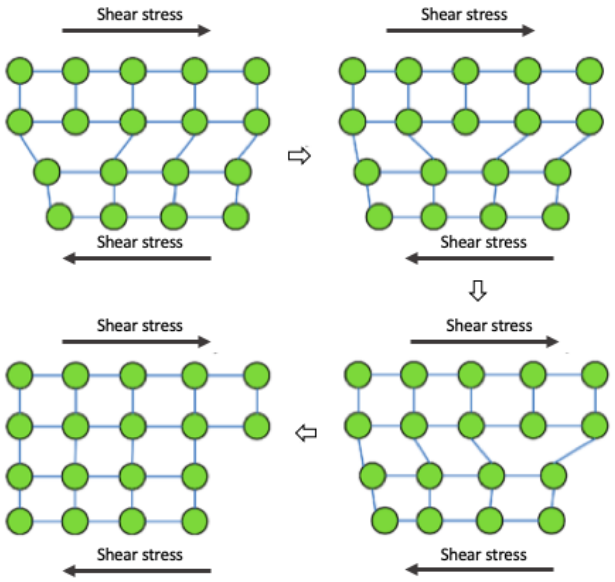

Figure 7. Schematic of the dislocation slip mechanism in a crystal [95].

exposed to high temperatures during the deformation. The strain energy stored in the material during the steady-state stage in addition to the high temperature, supply the driving force for the recovery process. Although work hardening and recovery happen at the same time during the steady-state stage, there is a balance between these two. During the recovery, the dislocation density decreases, or dislocations are rearranged into lower energy arrays e.g. subgrain boundaries. This requires the dislocation climb, as well as slip which are dependent on the atomic movement and self-diffusion in the crystal lattice [92]. Figure 8 schematically show the dislocation climb in the crystal lattice. As seen in Figure 8, the presence of vacancies

is necessary in the vicinity of the dislocation to enable climb by vacancy-atom exchange. The equilibrium concentration of vacancies increases exponentially with temperature according to equation Equation 1.20 in which, N_V is the number of vacancies, N is total number of lattice sites, Q_v is the vacancy formation energy, T is temperature, and k is Boltzmanns constant [94].

$$N_V = Nexp(-\frac{Q_\nu}{kT}) \tag{1.20}$$

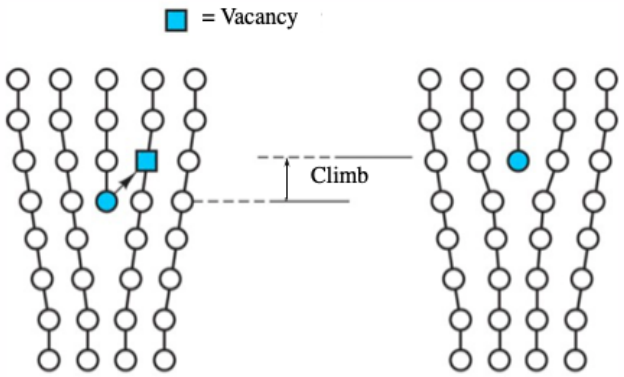

Figure 8. Schematic of the dislocation climb mechanics in a crystal.

Mott [96] also suggested that the rate-controlling process in dislocation climb mechanism of steady-state creep is the diffusion of vacancies. Therefore, increasing the temperature in-

creases the number of vacancies necessary for the effective vacancy-atom exchange for the climb mechanism which further leads to increase in the steady-state creep rate [92].

1.4.2 Diffusional Creep

In conditions of high temperature and low stress, the stress-directed vacancy flow can lead to deformation in the absence of dislocation movement. As the tensile stress is applied during creep deformation, the distance between atoms on the grain boundaries perpendicular to the stress axis increases. At the same time, the distance between the ones on the grain boundaries parallel to the stress axis decreases according to the Poisson contraction. This produces a driving force for the diffusion of the atoms from the grain boundaries parallel to the stress axis to the one perpendicular to it. This creep mechanism was first introduced by Nabarro and Herring [97] [98], which explains that the strain accumulation during creep at low stress and high temperature happens by the diffusional transport between the material and the sinks such as grain boundaries or external surfaces. This phenomenon shown in Figure 9 is the reason for the elongation during the creep or tensile stretching of the material. However, depending on how the atoms are diffusing from one grain boundary to the other one, there are two different types of diffusional creep. If the diffusion happens through the lattice, it will be *Nabarro-Herring (N-H) creep* in which, the strain rate of the creep depends on the stress σ, the lattice diffusivity D_L, and the diffusion distance d with A_L being a constant, as shown in equation below [85, 99]:

$$\dot{\varepsilon}_{N-H} = A_L(\frac{\sigma}{d^2})D_L \tag{1.21}$$

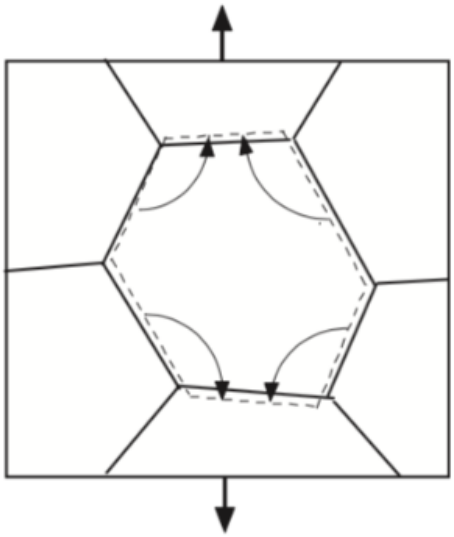

Figure 9. Nabarro - Herring model of diffusional flow. Arrows indicate the flow of vacancies through the grains from boundaries lying normal to the tensile direction to parallel boundaries. Thicker arrows indicate the tensile axis [99].

On the other hand, if the diffusion occurs along the grain boundary, it is called *Coble creep* with the same driving force as N-H creep. In this mechanism, the grain size plays an important role as it determines the number of the grain boundary diffusion paths. Therefore, the strain rate is controlled by the stress, diffusion distance, and the diffusivity along the grain boundaries D_{gb}, with A_G being a constant as follows [99]:

$$\dot{\varepsilon}_C = A_G(\frac{\sigma}{d^3})D_{gb} \tag{1.22}$$

As the creep temperature increases, the chance of creep diffusion through the lattice increases since the activation energy for grain boundary diffusion is lower than the lattice. Thus, the creep mechanism is more toward the Coble creep at low temperature, and more of the Nabarro-Herring at high temperatures [90, 92, 99].

1.4.3 Grain-Boundary Sliding

Grain size plays an important role in strengthening mechanisms according to the Hall-Petch relation:

$$\sigma_y = \sigma_0 + \frac{k_y}{\sqrt{d}} \tag{1.23}$$

where σ_y is the yield stress, σ_0 is the resistance to dislocation glide, k_y is a measure of the dislocation pile-up behind an obstacle such as grain boundary, and d is the grain size. According to Hall-Petch equation, the strength of the material is increasing with decreasing the grain size. Although it is expected that the material with smaller grain size demonstrate a higher strength; smaller grain size has a detrimental effect when it comes to creep resistance. This is because of the undesirable processes that occur at the grain boundaries during the creep such as being a source of vacancies. Therefore, grain size has a dual effect in creep damage, where smaller grain size increases the strength due to barriers to dislocation glide, and at the same time, increases the number of the vacancies which are the prerequisites for dislocation climb [90, 92, 99].

Grain boundary sliding is an important factor in creep damage, where two grains slide past each other along the common boundary. Thus, mechanism is the same as the viscous flow in amorphous materials. Most significant changes in the microstructure start at the tertiary

stage, with initiation of rounded (r-type) or wedge-shaped (w-type) cavities. Usually, the wedge-shaped cavities are seen at the grain boundaries which can be a sign of an upcoming creep rupture. The coalescence of these cavities will further lead to creep fracture. This implies that the grain boundary sliding is a critical factor in nucleation of voids and cavities. As the strain increases during the creep, the more cavities are formed under the shear stress acting on the boundaries. Figure 10 is showing the schematic of the w-type cavity induced by the grain boundary sliding. Zener also suggested that the wedge-type crack can happen at triple points under tensile stress and sufficiently high temperature, where the boundaries behave in a viscous mann-r. In this model, the crack nucleates at dislocation pile-ups due to the stress concentration and grows by the coalescence of two or more dislocations as shown in Figure 11 [92].

In addition, it has been seen that the cavities preferentially form at grain and phase boundaries. This is due to the fact that the cavitation process tends to occur at the stress concentration points in the sliding boundaries or interfaces. In addition, there is always a chance that the pores or voids exist in the material from the manufacturing process which can reduce the creep life of the component even less than the designed life. As a conclusion, the nucleation, growth and coalescence of the pre-existing cavities or new ones formed at the grain boundaries mainly perpendicular to the applied stress is an important factor for creep failure, especially at high temperature and stress combined with smaller grain size. The greater the creep time, the higher the number of the cavitated boundaries, and thus the higher the possibility of creep failure [92].

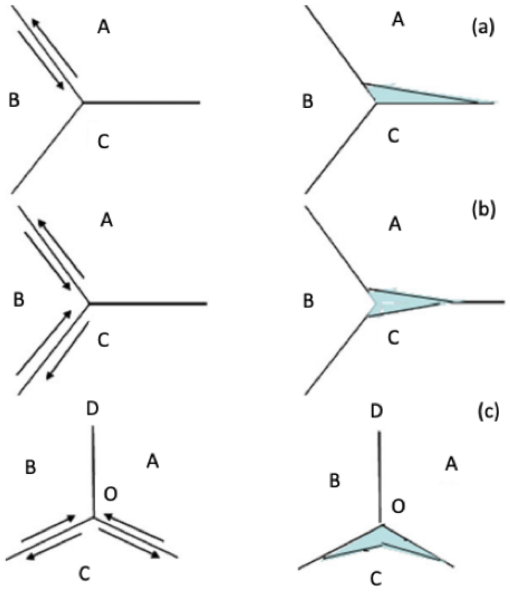

Figure 10. Schematic of a w-type cavity formed by grain boundary sliding mechanism [100].

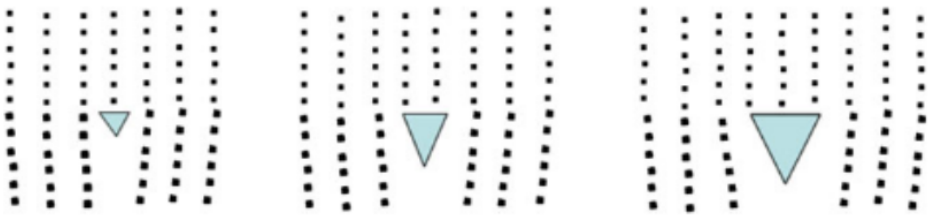

Figure 11. Schematic of the Zener's idea for nucleation and grow of the cracks at dislocation sites [92].

CHAPTER 2

PLASTIC DEFORMATION DETECTION IN ALUMINUM 1100 BY LINEAR AND NONLINEAR ULTRASONICS [1]

2.1 Background

One of the most critical goals of engineering science is to build mechanical systems which are both reliable and economic. The performance of mechanical systems depends on the life expectancy of their parts which are related to the applied load and their mechanical or structural response. Occasionally, overloading may occur on some parts, increasing the internal stresses or mechanical damage in the material that would eventually lead to catastrophic failures. In order to avoid the occurrence of overloading and possible premature failures, periodic assessment of the internal stresses or damage of the structural components such as in nuclear reactor parts, railroad wheels, and pressure vessels is necessary [26]. In the following section, investigations undertaken in the past two decades regarding the effect of plastic deformation on the linear and nonlinear ultrasonic parameters are described.

Early research on using ultrasonic velocity for detection of plastic deformation in materials, stated that plastic deformation results in the increase in dislocation density which will further

---

[1]The content presented in this chapter was previously published in the Journal of Measurement as "Wavelet Based Harmonics Decomposition of Ultrasonic Signal in Assessment of Plastic Strain in Aluminum," [2] and in the Journal of Nondestructive Evaluation as "Influence of Mesoscale and Macroscale Heterogeneities in Metals on Higher Harmonics under Plastic Deformation" [1]

lead to a decrease in the ultrasonic velocity [101]. Therefore, the higher the plastic deformation, the slower the sound velocity. On the other hand, it is known that in the case of plastic deformation introduced by cold work followed by recrystallization, smaller size sub-grains may be produced. A study related to the effect of cold work and recrystallization on the sound velocity in cast steels by Prasad et al. [102] suggests that the longitudinal sound velocity can change from grain to grain due to grain-misorientation especially after cold work and recrystallization. This change can be due to the variation in the elastic constant of each grain in the wave propagation direction. Consequently, the decrease in the velocity at larger deformations can be related to both dislocation density increase and grain misorientation. Palanchamy et al. [103] studied the effect of cold work and annealing on Ti-modified austenitic stainless steel using shear wave velocities. They found out that the velocity increases slightly during the recovery stage followed by a significant increase during the recrystallization stage. An optimum point was observed for the velocity corresponding to the completion of recrystallization. In addition, Salinas et al. [104] proposed a method to measure the change in dislocation density using shear wave velocity in aluminum. They attributed the change in velocity to the interaction of the elastic waves with the oscillating dislocations, specifically dislocation density and dislocation length.

Although sound velocity has been used in many investigations to evaluate the plastic deformation in the material, its sensitivity relative to the nonlinear ultrasonics is still questionable especially when the damage is small or in early stages. Even in the case of more pronounced damages such as fatigue damage, the most significant change in the microstructure before crack

initiation is the increase in the dislocation density. However, the microplastic deformation (generated by dislocations) will not affect the microplastic properties such as modulus of elasticity, sound velocity, and attenuation; their effect is so small that is hard to be accurately measured by these techniques [6]. Hikata et. al. [105] first introduced the contribution of the dislocations to the harmonic generation because of the displacement due to bowing out of dislocations, U_d which is defined based on the Koehler-Granato-Lücke vibrating string model [106, 107]. The reason why the dislocations are easier to detect via nonlinear techniques is that there is a slightly nonlinear stress-strain relationship produced in a localized volume near a single dislocation or pair of dislocations. When millions of dislocations are accumulated in a localized volume with increasing the plastic deformation, a nonlinear distortion is introduced in the ultrasonic wave propagating in that volume which will further emerge as higher harmonic components in an initially monochromatic wave [6]. Herrmann et al [6] used nonlinear Rayleigh surface waves to quantify the amountdth of dislocations generated during fatigue damage and detect the presence of dislocations in the very early stages of fatigue. In addition, they calculated the nonlinear parameter in the case of monotonic loading for the same samples since it is believed that the cyclic loading is the strongest source of nonlinearity among all other potential sources [70]. The increase in stress from undamaged to 145% of σ_{yield} of the material (before UTS) showed about 35% increase in the nonlinearity parameter β with significant increase for up to 125% of σ_{yield} and less increase at higher stresses. Xiang et al. [79] explored the role of dislocations on acoustic nonlinearity even further and modeled the β nonlinearity parameter based on the Poisson's ratio, fraction, and type of the dislocation. They also found a higher sensitivity of β

to edge dislocations for the materials with large Poisson's ratio. Their model was verified on cold-rolled 304 stainless steel plates and plastically deformed 30Cr2Ni4MoV.

The effect of plastic deformation in aluminum alloys and its correlation to the acoustic nonlinear parameter has also been investigated by some researchers. For example, in the study conducted by Rao et al. [74], they assessed the effect of plastic deformation on AA7175-T375 aluminum alloy with longitudinal and guided surface waves to quantify the residual strain in the materials. In this study, they showed that there is a gradual increase in β up to about 2% strain and then it increases significantly for higher strain levels. They attributed these two stages of increase to the increase in dislocation density and formation of cellular dislocation patterns (or sub-grains), respectively. In addition, the nonlinearity parameter was measured at 6 different points along the gage length of the dog bone sample, and a maximum β was observed at each strain level, even though the material was under uniform plastic deformation. AZ31 magnesium-aluminum alloy was studied by Shui et. al. [76], in which they used longitudinal bulk waves to measure the nonlinearity parameter for the monotonically loaded samples at different strain levels. They performed tensile tests both in the elastic and plastic regions of the stress-strain curve and found out that the β parameter only varies slightly when the stress is below the σ_{yield}, while increases rapidly for the stresses after the yield point. Razvi et. al. [108] determined the effect of the second phase particles on Acousto Elastic Coefficient (AEC) and nonlinearity parameter in heat treatable and work hardenable aluminum alloys such as Al 7075 and Al 5086. They found out that the AEC in work hardenable alloys is neither affected by the increase in the volume fraction of the second phase particles, nor by the size and the distribution

of the particles. However, in the case of heat treatable alloys, Razvi and Salama et. al. [109] both agreed on the increase of AEC with the volume fraction of particles, while reaching a plateau at higher volume fractions. In the case of β nonlinearity parameter, its sensitivity to the second phase particles was proven for both work hardenable and heat treatable alloys. Furthermore, nonlinear longitudinal and surface waves were utilized to assess the effect of plastic deformation on β in aluminum alloy 7009 by Zhang et al. [110]. Their results revealed an increase in β with increase in plastic strain for both wave types which could be fitted by a simple power-law relation. They attributed the difference in the stress exponent in the derived power law for two wave types, to the microstructural difference between the near surface and the material away from the tested surface. In a recent study by Espinoza [111], the relative dislocation density in aluminum and copper samples was measured using Nonlinear Resonant Ultrasound Spectroscopy (NRUS) method, and second harmonic generation measurements. The change in the dislocation density was introduced by thermomechanical treatments on the samples. They found that NRUS has the highest sensitivity by a factor of two to six, and second harmonic generation by 14-62% while the harmonic generation technique is much faster and simpler.

Other nondestructive techniques or wave modes have also been utilized in the past years to investigate the effect of damage evolution during the plastic deformation in Aluminum alloys. Lugo et. al. [112] studied the damage evolution in Al 7075 by acoustic emission technique. The acoustic emission counts were found to have a strong correlation with the number of the cracked particles in this alloy during the monotonic tensile loading. In addition, the acoustic emission counts helped them to understand that the greatest number of the particle cracking

happen at the initial stage of deformation. In addition, the level of plasticity in the metal specimen was researched by Pruell et al. [75] using acoustic nonlinearity in Lamb wave. They concluded that even though Lamb waves are considered as multimodal and dispersive, they can have a good interaction with the material's plasticity the same as the longitudinal and Rayleigh waves. Therefore, Lamb waves can be used to assess the plastic deformation in the material quantitatively, using higher harmonic generation. In another study, Sgalla et al. [66] investigated the effect of uniaxial stress on aluminum and steel specimens using ultrasonic critical-angle refractometry (UCRfr) technique. In this method, they measured the stress level in the material using the variations in the velocity of longitudinal, shear, and Rayleigh waves by measuring the changes in angle of refraction at the interface with a second medium. Their method showed to be a promising technique to measure the amount of the stress in the materials which can be further used to calculate the acoustoelastic constants of the longitudinal waves.

2.2 Technical Approach

2.2.1 Materials and Sample Preparation

Aluminum 1100 (Al 1100) was used in this investigation with a composition shown in Table I. Nine tensile specimens were machined from a 6.3 mm (0.25 in.) thick cold rolled plate according to ASTM standard E8 [113] to the dimensions shown in Figure 12. All samples were stress relieved at 250°C for 15 min prior to tensile testing.

2.2.2 Systematic Deformation of Aluminum Samples to Different Strains

A model 1125 MTS tensile machine was used for the tensile tests using a strain rate of 2.54 mm/min. The first sample was tested to failure to obtain the stress-strain curve and to

TABLE I. Chemical composition of Al 1100 according to ASTM standard B221-14 [114]

Aluminum 1100	**Al**	**Cu**	**Mn**	**Si + Fe**	**Zn**	**others**
Weight%	99 min	0.05 - 0.2	0.05 max	0.95 max	0.1 max	0.15 total

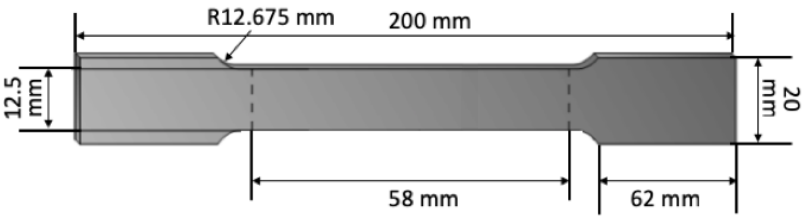

Figure 12. Tensile test sample dimensions for Al 1100

determine the yield and tensile strengths, as well as the Young's Modulus and the strain at the ultimate tensile stress (UTS), which are reported in Table II.

The remaining samples were plastically deformed between 0.5% and 4% at 0.5% strain increments to produce different uniform plastic strains in the gauge length and to avoid non-uniform (localized) plastic deformation at the onset of necking when reaching to the ultimate tensile strength (UTS). Figure 13 shows the stress-strain curves for all the samples tested.

After tensile testing, the microstructures of four selected samples were examined by cross sectioning the specimens into small pieces ($6.0 \times 6.0 \times 5.0$ mm^3) from the middle of the gauge

TABLE II. Experimentally determined mechanical properties of Al 1100

Yield stress	90 MPa
Ultimate Tensile Strength (UTS)	120 MPa
Strain at UTS	0.048
Young modulus	72.0 GPa

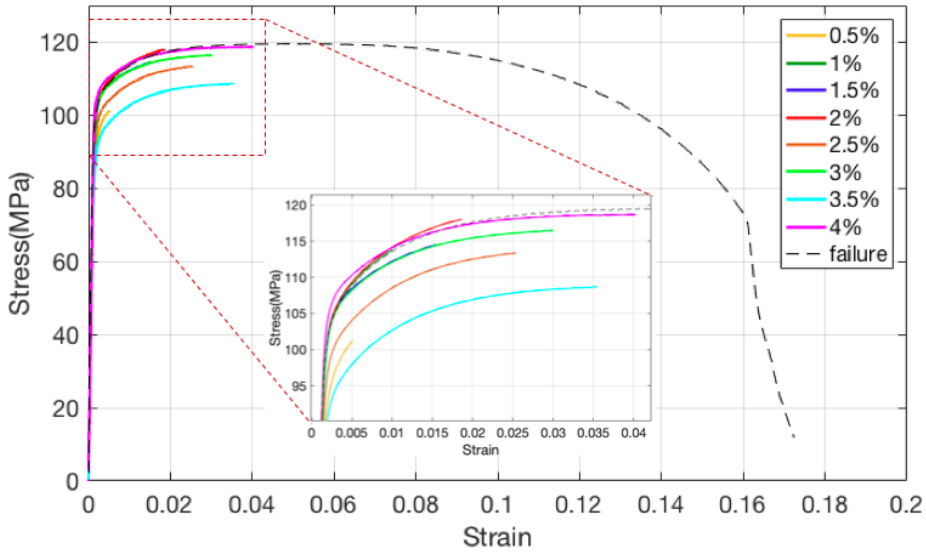

Figure 13. Stress-strain curves depicting the different strains applied to the tensile specimens.

length. The samples were prepared using standard metallographic procedures and etched in a solution of 12 parts of hydrochloric acid, 6 parts of Nitric acid, 1 part of hydrofluoric acid, 1 one part of distilled water. The microstructure of the selected samples was examined using light

optical microscopy and Scanning Electron Microscopy (SEM) to identify the presence of precipitates in the matrix. Quantitative metallography was conducted using ImageJ software [115] to measure the population of these precipitates due to impurities, both in size and in volume fraction. This measurements were conducted based on a previous study to establish if the presence of precipitates is a parameter affecting the acoustic nonlinearity measurements [108]. Figure 14 illustrates the sequential image steps followed in the ImageJ software to calculate the volume fraction of the second phase. More than 20 optical microscopy images were used for each strain level in order to assure the statistical reliability of the results.

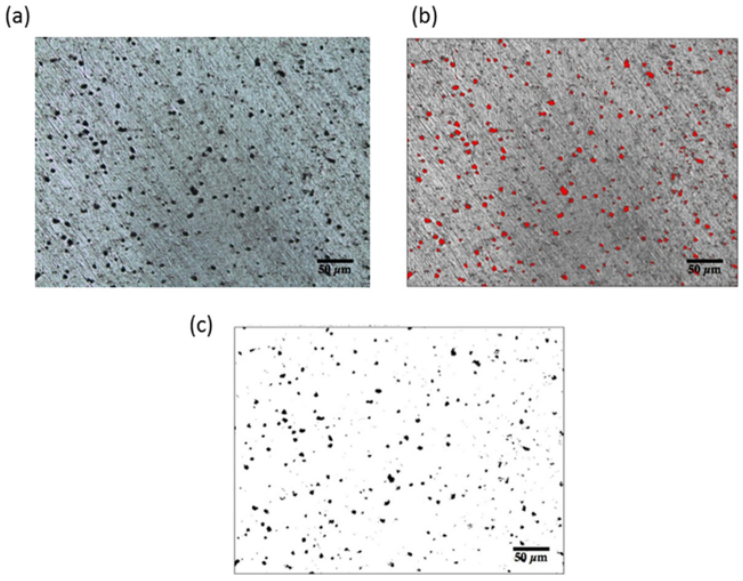

Figure 14. (a) Original micrograph of aluminum 1100, (b) and (c) imaging steps by ImageJ software to calculate volume fraction of second phase.

2.2.3 Ultrasonic Testing

2.2.3.1 Immersion Linear Ultrasonics (Acoustic Microscope)

An experimental study was carried out to examine the plastic deformation using immersion ultrasound. The equipment and the procedures for the linear ultrasonic testing is the same for all samples in the next chapters unless otherwise noted. The ultrasonic system used is the Sonoscan Gen6 C-mode Scanning Acoustic Microscope (C-SAM) with transducers of up to 400 MHz and a resolution of 3 μm and 100 gates for multi-dimensional analyses. The method is based on immersion ultrasonics, which utilizes de-ionized water as a coupling medium as shown in Figure 15. In this study, the reflection mode was selected using 15 MHz transducers for mapping the change in thickness and thus, detection of any localized damage.

Before the test, the surfaces of all the samples were ground using a 600-grit grinding paper to create a smooth surface and prevent wave distortion. The samples were then submerged in water and any traces of air bubbles on the surfaces were eliminated. The pulse-echo mode was utilized to measure the reflection time from the back-wall, which provides the indirect measurement of wave velocity in solid and thickness change. The arrival time was then used to generate the acoustic imaging.

2.2.3.2 Nonlinear Ultrasonics Measurements

Since the nonlinear ultrasonic method is based on detecting higher-harmonic signals, the through-transmission mode was selected for tuning the receiving transducer to the higher harmonics of the transmitting transducer as shown in Figure 16b and c. The specimens with different levels of plastic deformation are placed between transmitter and receiver. A light oil

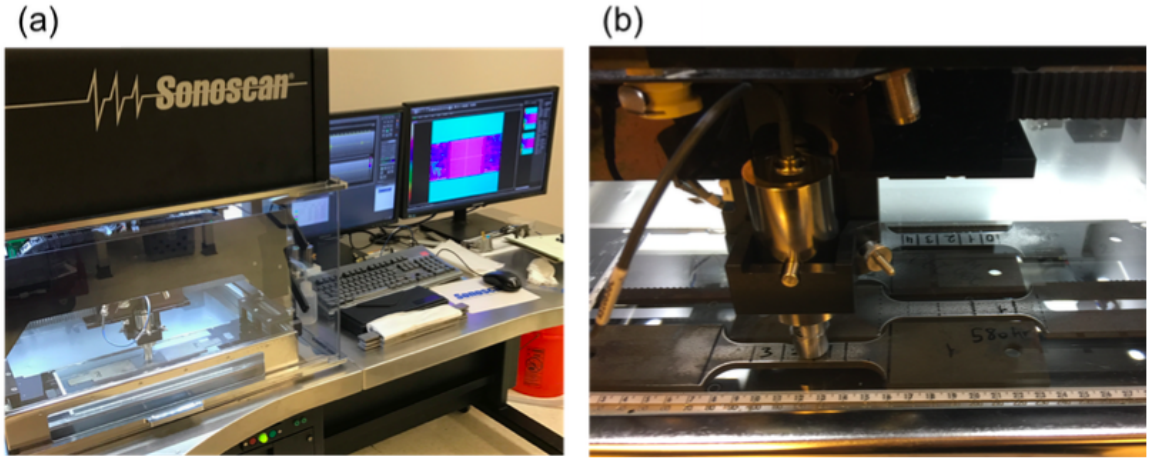

Figure 15. (a) Test set up for immersion linear ultrasonic measurement, (b) The immersion tank filled with water.

lubrication is utilized as coupling medium between the transducers and the test specimen and a weighted grip (24.5 N) was used to hold the transducers aligned to each other (Figure 16b) and to provide a consistent coupling force and minimize coupling errors as discussed by Liu et al. [116].

The major inputs to the data acquisition of nonlinear ultrasonic testing operating in through-transmission mode are input voltage, excitation frequency, and cycles in harmonic loading. In this study, the input signal was a 10-cycle, 100-volt tone burst (i.e., harmonic signal with 10 cycles as shown in Figure 16c) at 2.25 MHz, which was generated by a pocket UT system manufactured by MISTRAS Inc. The time-history signal of the 5 MHz receiver was recorded

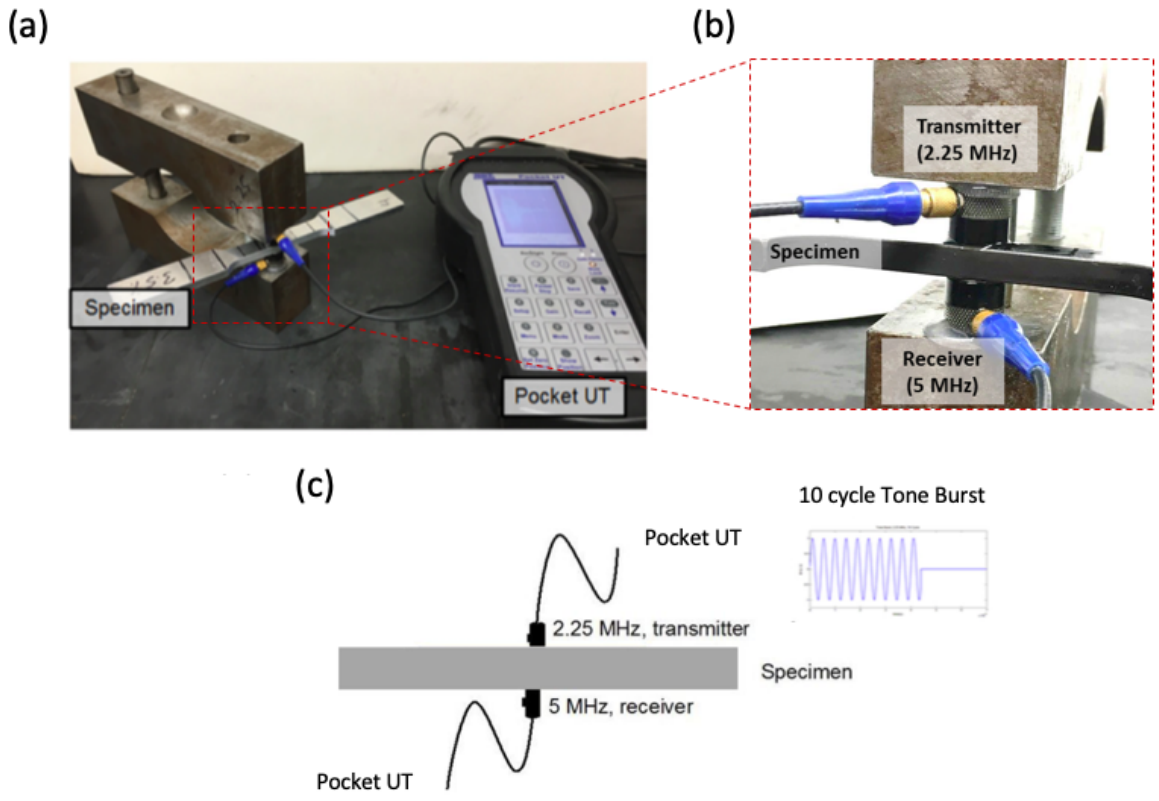

Figure 16. Ultrasonic testing of aluminum specimens, (a) experimental setup, (b) ultrasonic transmitter and receiver in through-transmission mode, (c) schematic diagram.

using the same UT system with the sampling frequency of 100 MHz and a band-pass filter of 120 MHz. This transducer has a bandwidth in the range of 3.287.67 MHz such that the second harmonic frequencies could be measured. The transmitting and receiving transducers used in this study were piezoelectric transducers manufactured by Olympus with the effective diameter of 0.95 cm (0.375 in.).

The measurements were performed three times by recoupling the ultrasonic transducers between each measurement to check the repeatability of the results. To improve the signal to noise ratio (SNR), twenty signals were averaged in each testing. The signal processing was performed using MATLAB software to change the received signal from the time-domain to frequency-domain signal using an FFT-based method. Figure 17 shows an example of time-domain and frequency-domain waves for one sample before plastic deformation.

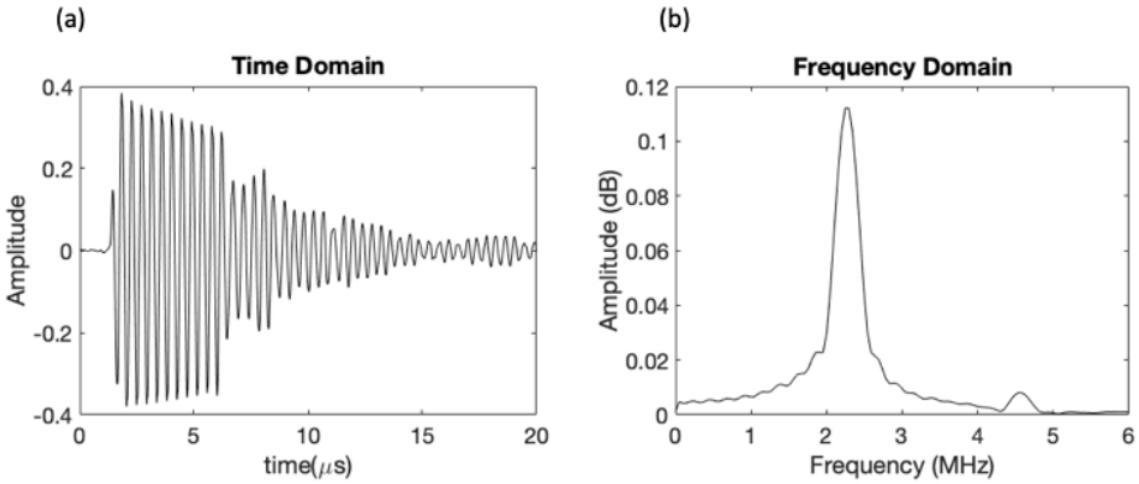

Figure 17. (a) Typical time-domain waveform and (b) its frequency spectra for a sample before plastic deformation.

2.2.4 X-ray Diffraction (XRD)

The X-ray diffraction technique was used to assess the plastic deformation in the materials with different strain levels and at two different locations, the shoulder of the tensile sample and at the center of the gage length for each strain as shown in Figure 18. For this purpose, 15×15 mm^2 samples were cut from the same place. The uniform and non-uniform plastic deformation was examined by full width at half maximum (FWHM) of XRD profile. XRD was carried out on a Siemens D5000 X-ray Powder Diffraction (XRD) system with Cu-Kα radiation ($\lambda = 1.5418$ $\mathring{A}$). The X-ray generator was run using a voltage of 40 KV and a current of 30 mA, with the samples scanned at 0.02°/step and 3s/step using a 2θ angle diffraction ranges from 30° to 80°.

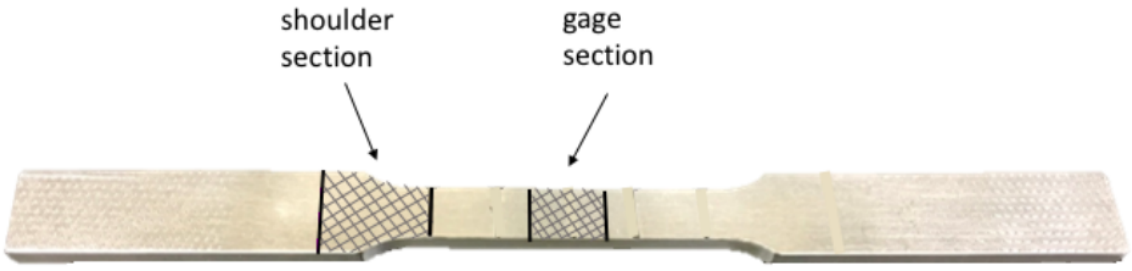

Figure 18. Shoulder and gage sections used to study the effects of uniform and non-uniform deformation.

2.3 Results and Discussion

2.3.1 Optical Microscopy and Second Phase Precipitates

Figure 19 shows the typical microstructure of Aluminum 1100 analyzed for this investigation which consists of an aluminum matrix with embedded second phase precipitates. In addition, the SEM pictures of the sample strained to 0.5% is shown in Figure 20. Energy-dispersive X-ray spectroscopy (EDS) analysis was done on the sample and it confirmed to be pure Al. SEM micrographs did not show presence of second phase particles, which might have been pulled out of the matrix during polishing.

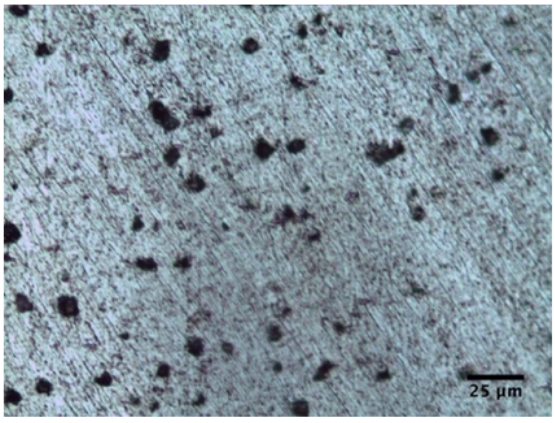

Figure 19. Typical microstructure of Al 1100 used in this study after stress relief.

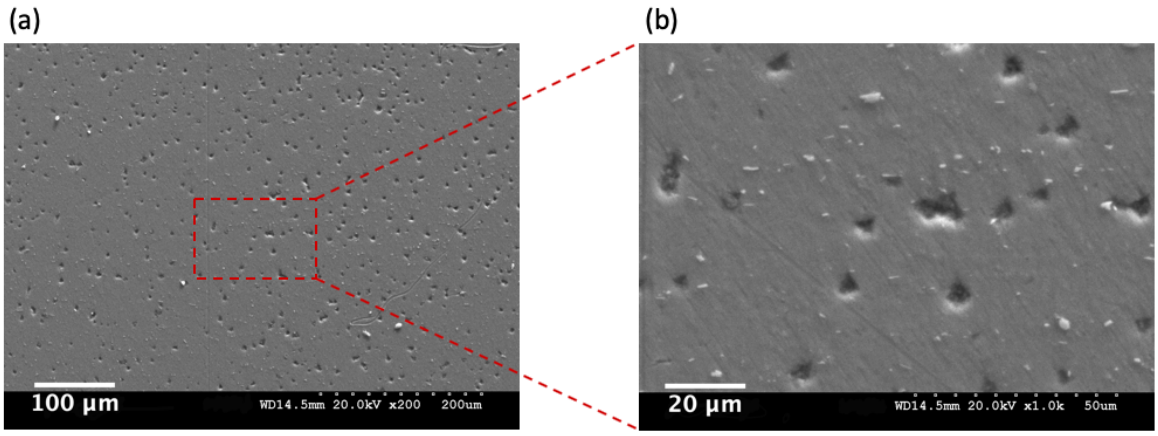

Figure 20. SEM images of the Al 1100 plastically deformed to 0.5% at (a) 200X and (b)1000X.

As mentioned before, regardless of the precipitate's type, it is important that their volume fraction remains the same for all the samples. Figure 21 shows that the volume fraction of the second phase precipitates remains constant for all test specimens, which eliminates the possible effect of second phase presence on the nonlinearity parameter.

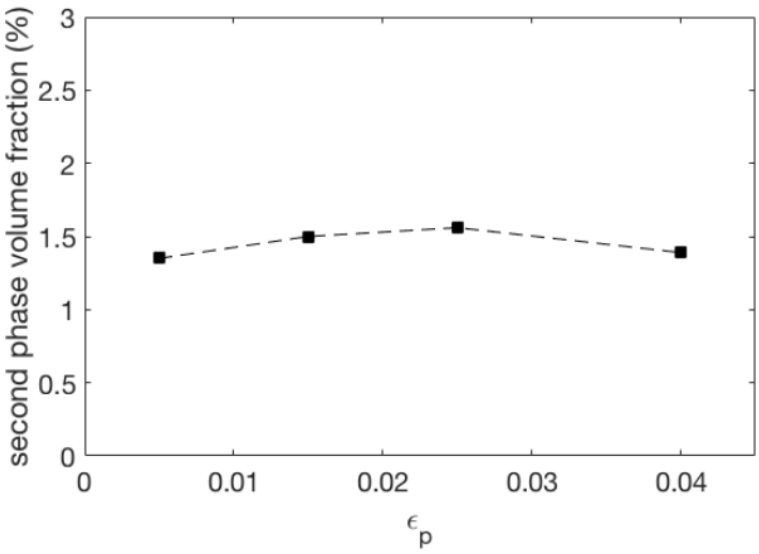

Figure 21. Second phase volume fraction measurements for four aluminum 1100 samples.

2.3.2 Plastic Deformation Detection with Ultrasonics

2.3.2.1 Linear Wave Velocity

During the tensile tests it was determined that the necking or beginning of localized deformation occurred at a strain of 4.8%. Since all test samples were strained to levels below necking (see Table II), it is expected that the deformation along the gage length of the samples would be uniform. Figure 22 shows the variations in the color map corresponding to the time of flight for the samples with different strain levels. In addition, three TOF readings along the gage length has been added to the image for each sample to give a better reading. The uniformity

in the colors assigned to the TOF of the samples also supports the uniform plastic deformation in these samples.

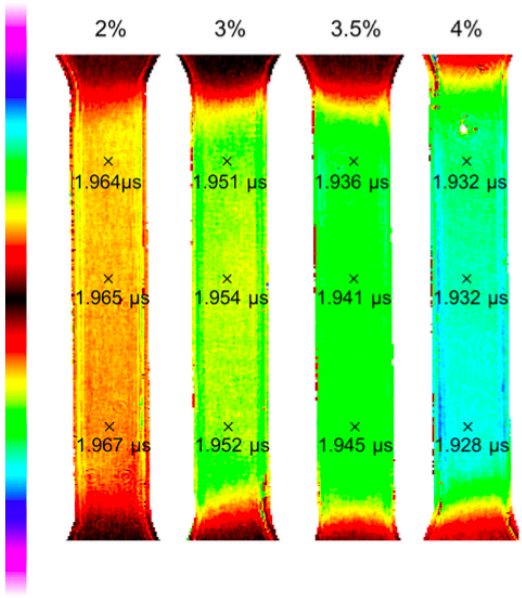

Figure 22. Color map of time of flight change for the sample with different strain levels shown at top.

As seen in Figure 23, the average time of flight decreases with the plastic deformation. However, it should be noted that this decrease can be attributed to the diminishing of thickness due to the plastic deformation. Therefore, to investigate the effect of thickness changing throughout the gage length, the thickness was precisely measured along the gage length in increments of

10 mm using micrometer with precision of 0.025mm. The results are shown in Figure 24 with the actual sample showing the locations where measurements were obtained. Based on this figure, the sample thickness along the gage length decreases with higher strain levels. However, the gage length thickness for each strain level is almost constant with some minor fluctuations which indicates the uniform plastic deformation and the absence of necking.

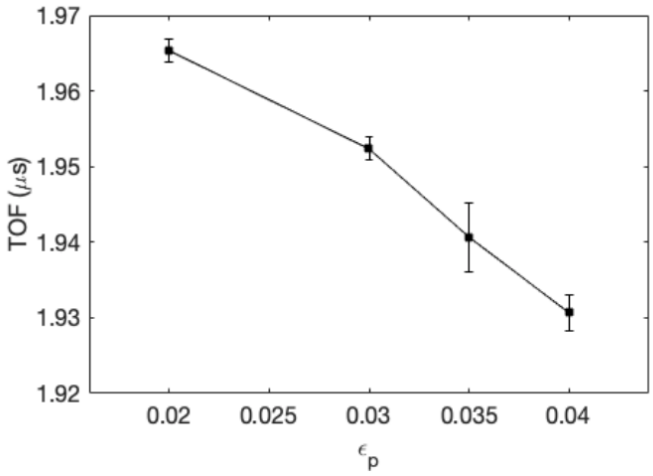

Figure 23. Change of TOF with plastic deformation for Al 1100.

Having the exact TOF and thickness of three points along the gage length, the velocity was measured and shown with filled triangle (▲) markers in Figure 24. Some small fluctuations in the velocity measurements could be observed along the gauge length, while based on the

thickness results, they all were expected to have similar magnitudes. Such discrepancies for each specific strain might be due to experimental errors such as surface heterogeneities caused by machining of the specimens.

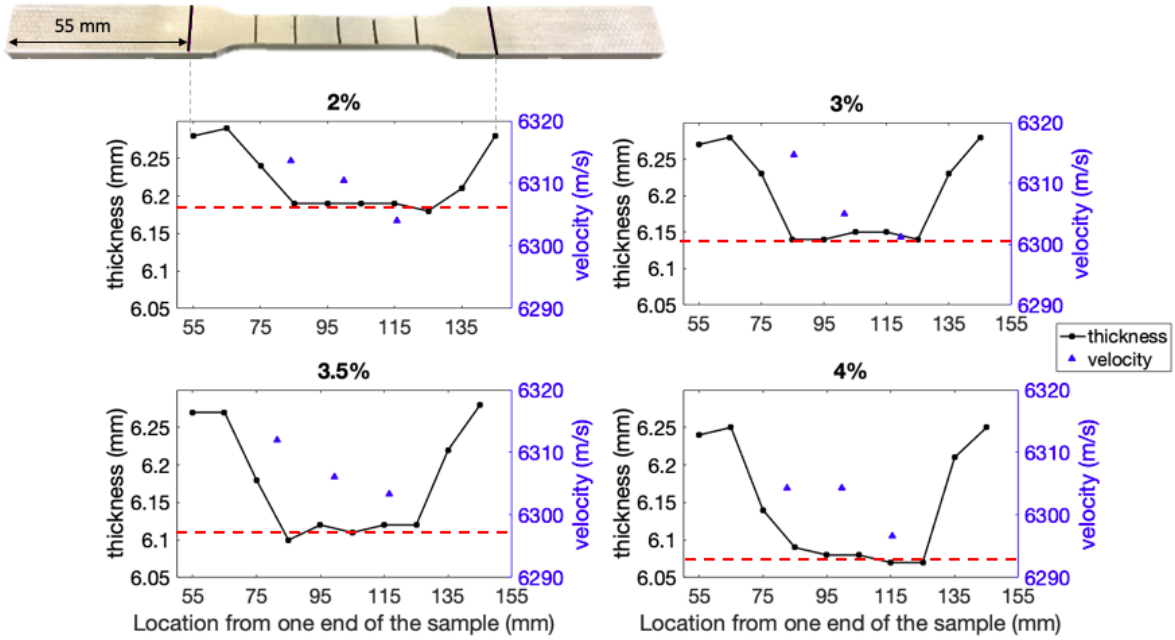

Figure 24. Change in the thickness and velocity along the gage length for samples with 2, 3, 3.5, and 4% strain.

An average velocity was calculated using the measurements obtained for each strain level and plotted versus the strain as shown in Figure 25. The velocity was observed to decrease as

the strain increased. Therefore, there is something else other than decrease in the thickness contributing to the velocity change, which can be the increase in the damage level i.e. increase in the dislocation density due to the higher levels of plastic deformation. The error bars for the velocity measurements are significantly large at each strain which can question the reliability of this specific method to detect small deformations. In addition, the overall change in the velocity is just about 0.12% for 2% change in plastic deformation which is so low and questions the sensitivity of the linear wave velocity in damage detection. The linear wave velocity measured with acoustic microscope, may not be a suitable technique for detecting early damage in the material, but its sensitivity to the change in the thickness is so high that it can detect the localized damage easily even though it is not detectable by visual inspection.

2.3.2.2 Ultrasonics Nonlinearity Parameter β

The aluminum specimens were plastically deformed to different strain levels and then tested using longitudinal ultrasonic waves in a through-transmission mode to correlate the plastic deformation with the acoustic nonlinearity parameter (β). This parameter, as discussed in the first chapter, depends on the amplitude ratio of the first and second harmonic frequencies (Equation 1.10). Figure 26 shows how this parameter changes with the degree of strain present on each sample. It was observed that those samples strained to levels up to 0.15 strain do not show significant increase in β. These consistent β values are likely an indication of the limited resolution of this technique at this strain level, due to the low density and uniform distribution of dislocations. However, after 0.2 strain, there is a notable increase in β with a decrease at the end which can be due to the saturation of the nonlinear UT close to the necking point. The

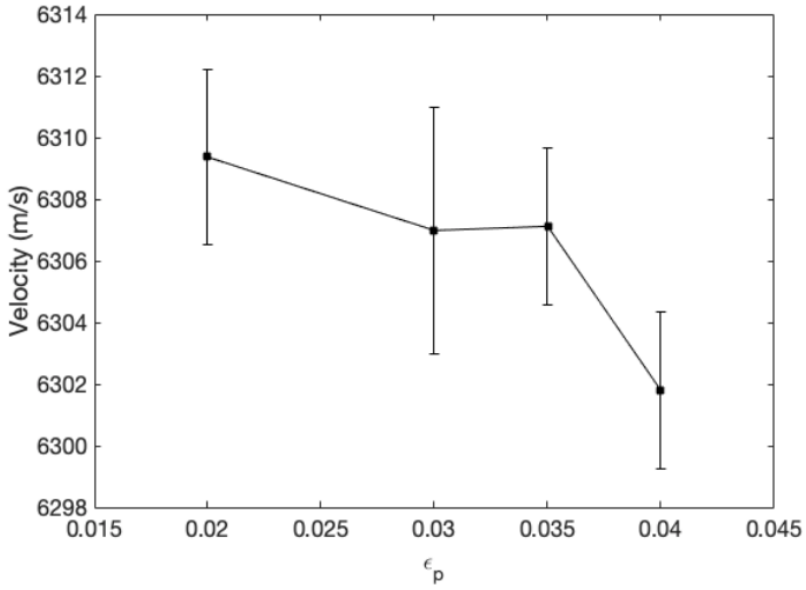

Figure 25. Velocity change for the samples with different %strain (error bars are indicating the standard error of the mean).

error bars in the figure are obtained by repeating the ultrasonic measurements three times for each strain level.

The total change in the nonlinearity parameter due to the plastic deformation in the Aluminum 1100 is about 40% for 4% strain. Compared to the linear wave velocity in the previous section, the change in for the samples with 2 and 4% is about 19% while 0.12% for the linear wave velocity. As mentioned before, the change in the β parameter in the case of plastic deformation is due to the increase in dislocation density and formation of microcracks as the deformation becomes localized during necking in the gauge length.

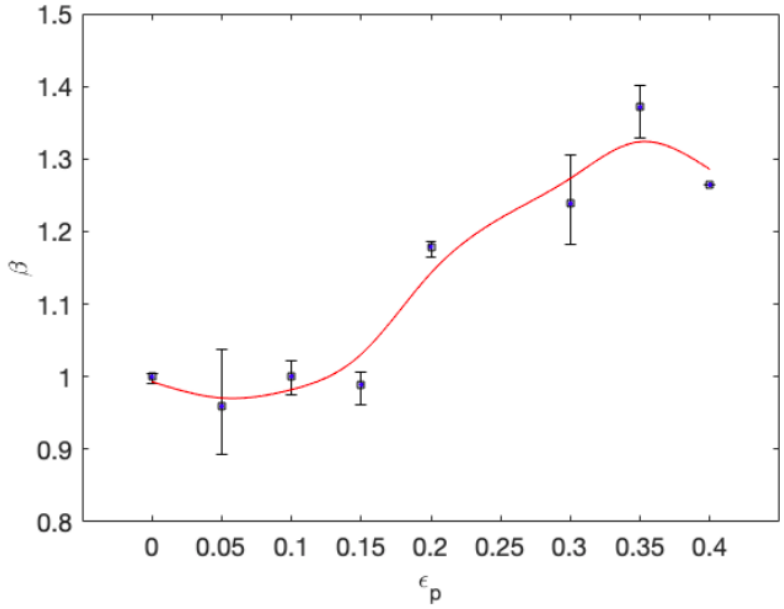

Figure 26. Acoustic nonlinearity parameter obtained by FFT method.

2.3.3 Effect of Geometry on Nonlinear Ultrasonics

The effect of geometry on β nonlinearity parameter was also investigated since residual non-uniform plastic deformation in the material may occur due to geometric changes, such as sharp corners or significant reduction in cross sections, that will respond differently to deformation introduced during processing. Figure 18 in the previous section shows two segments of the tensile sample, gage length and shoulder area, deformed differently as a result of changes in cross sectional area and curvature during deformation. This was used to understand the influence of uniform and non-uniform deformation on the acoustic nonlinearity parameter. In the next

two sections, the middle of the gage length is referred to as the gage sample, and the two shoulders, one at the left side and one at the right, if not averaged, are referred to as S1, and S2 respectively.

2.3.3.1 X-ray Diffraction

The nonuniformity of plastic deformation between the shoulder area and gauge length following a tensile test was verified by submitting specimens from both locations to an X-ray diffraction (XRD) analysis. The XRD results are ultimately correlated with the results of the β nonlinearity parameter discussed in the previous section.

X-ray diffraction is one of the techniques frequently used to measure the local strains and to distinguish between uniform and non-uniform plastic deformations. The peak shift is usually associated with uniform strains and peak broadening is caused by non-uniform strains. This information on the plastic deformation in the material is due to changes in the crystal interplanar spacing and other lattice imperfections such as an increase in dislocation density. However, one major weakness of this method is its low penetration depth of the X-ray beam, which is about 10μm in most metals that makes the measurements only reliable at the surface of the material [24].

Figure 27 shows the full X-ray diffraction pattern of two samples, one from the center of the gage length and the other from the shoulder location of the specimen strained 2.5%. It is seen that all peaks shifted to higher 2θ angles compared to the strain-free sample (according to standard XRD pattern for Aluminum, PDF#04-0787), and this shift is larger in the shoulder compared to the center of the gage length. This indicates that the residual stresses are larger

at the shoulder. The variations in peak intensities for shoulder and gage samples can be due to different orientations of crystals in the testing direction.

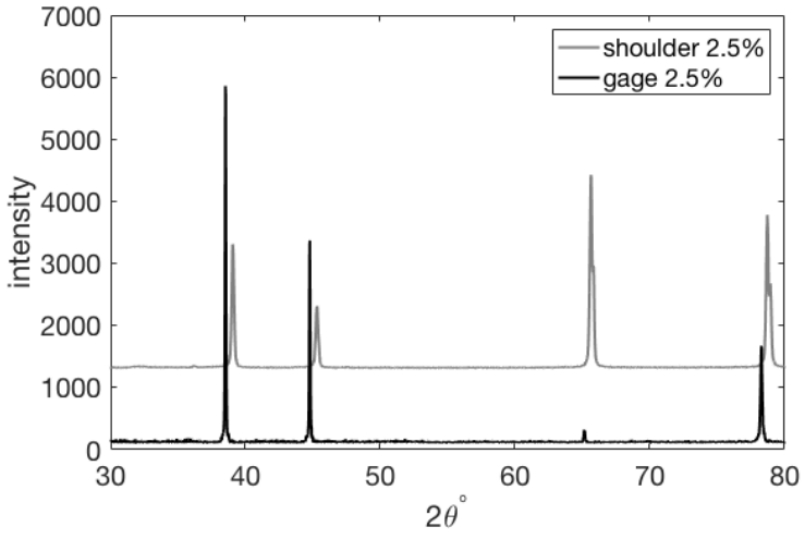

Figure 27. XRD patterns of the 2.5% strain sample at two locations: gage and shoulder.

In assessing the gradual deformation produced by the systematic increments in strain, all samples were scanned near $2\theta = 78°$. This range was selected since the interplanar spacing of the high index planes are much smaller and any small fluctuations are easier to detect. Based on Braggs law ($\lambda = 2dsin\theta$), since λ is constant for all the samples, there is a reverse relation between the interplanar d-spacing and 2θ. Figure 28 shows that 2θ shifts to higher angles as

the space between the planes decreases due to the applied tensile stress for all the locations. The doublet peak in this XRD pattern is due to non-monochromatic radiation.

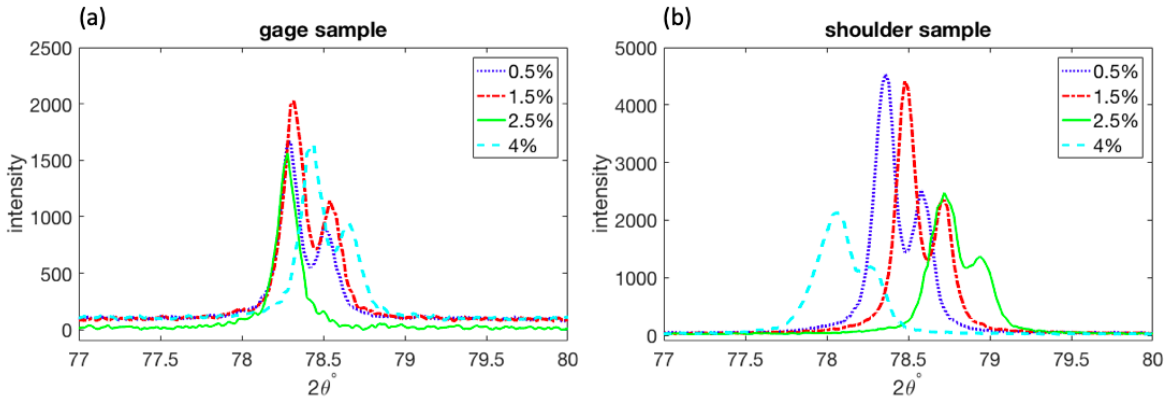

Figure 28. XRD patterns of all the samples at about $2\theta = 78°$ for (a) gage, and (b) shoulder.

The displacements for shoulder samples were larger as shown in Figure 29, as well as the increase in $\Delta 2\theta$ displacement for higher strains. Note that the peak for the shoulder area strained to 4% shifted to angles lower than 2θ of the standard aluminum 1100 peak at this particular 2θ angle. This can be due to the fact that at this strain level, the tension and compression stresses are both present because of the non-rectangular shape and drastic geometric change of the specimen from shoulder to gage length. In this case, the compression strains may have become dominant and shift the peak to lower 2θ values. In addition, although the samples are all from

the same plate, the rolling might not be uniform, and the machining of the specimen might leave residual stresses that already can affect the crystals d-spacing for each sample before any applied strain.

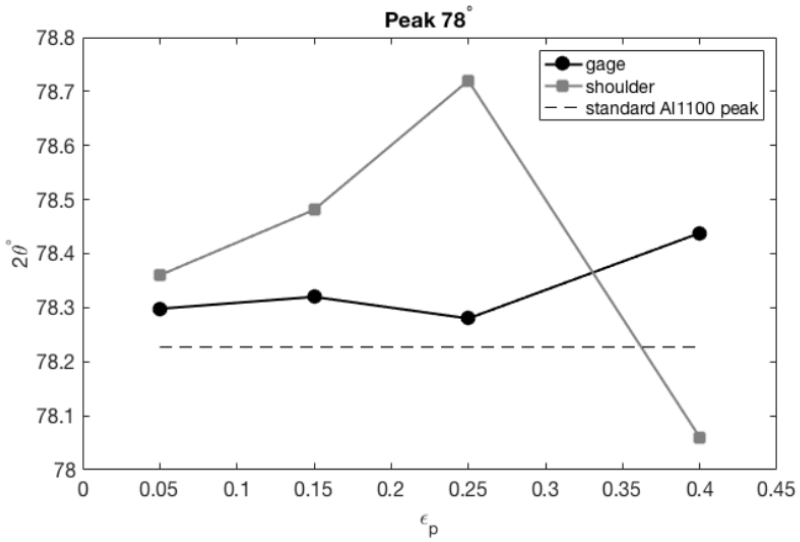

Figure 29. Displacements with degree of strain for gage and shoulder.

Figure 30 shows the results of the line broadening effects. As indicated earlier, line broadening in X-ray peaks is associated with non-uniform strains. In this investigation, it is expected to have non-uniform plastic strain in shoulders of the tensile specimen caused by the geometrical changes from the grip section into the gage length. The line broadening was calculated

using full width at half maximum (FWHM). FWHM can be used to determine the relative non-uniform plastic deformation. As the amount of non-uniform plastic deformation increases, the broadening in the peaks increases. In the cases that the uniform and non-uniform plastic deformations are both present, a mixture of peak shift and broadening can be observed.

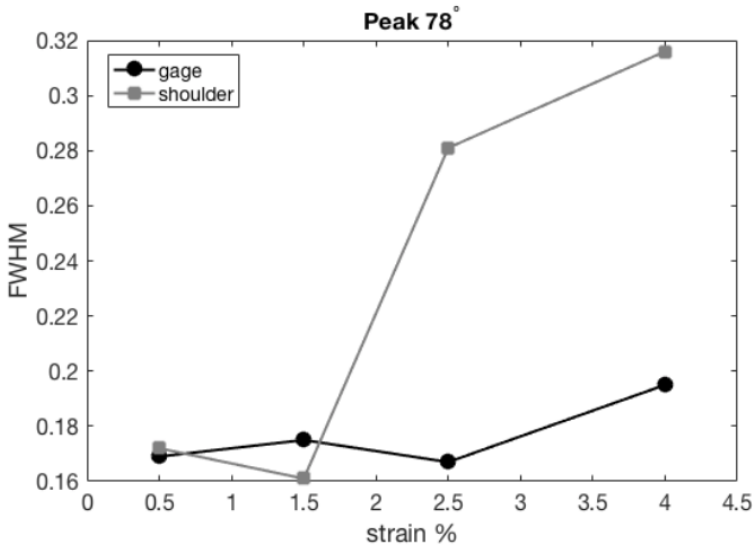

Figure 30. FWHM of the samples with different strain levels at $2\theta = 78°$.

Based on the observations in Figure 30, the FWHM for the shoulder area is larger than the gage area for each sample at different strain levels (except at the strain level 0.15), which indicates higher non-uniform plastic deformation in this region. The small increase in line

broadening observed for samples extracted from the gage length ($\sim$ 15% increase) is further evidence that a uniform straining occurs at the gage location. On the other hand, the shoulder sample shows an 83% increase in FWHM from 0.5% to 4% strain. This high increase in broadening re-confirms the presence of non-uniform plastic deformation in the shoulder compared to the gage length. These results were also confirmed with numerical simulation of the dog-bone sample to check the amount of tensile and compression stresses in different locations in the samples. The results are presented in a paper previously published [1].

2.3.3.2 Non-uniform Plastic Deformation Detection by β Parameter

Figure 31 shows the results of the NLUT measurements for the specimens subjected to different levels of plastic deformation. The data points represent the mean value of the repeated measurements normalized by the pristine specimen for each location, and the error bars represent the range of variation in the repeated measurements. Comparing the values of for two specimens obtained from the two shoulders and the gage after 4% strain, it is observed that increases about 2.7 times more in the shoulder area than the gage area. The non-uniformity of stress results in localized plastic deformation and contributes to the higher nonlinearity of the material in the shoulder area which can be assessed with the nonlinear ultrasonic testing.

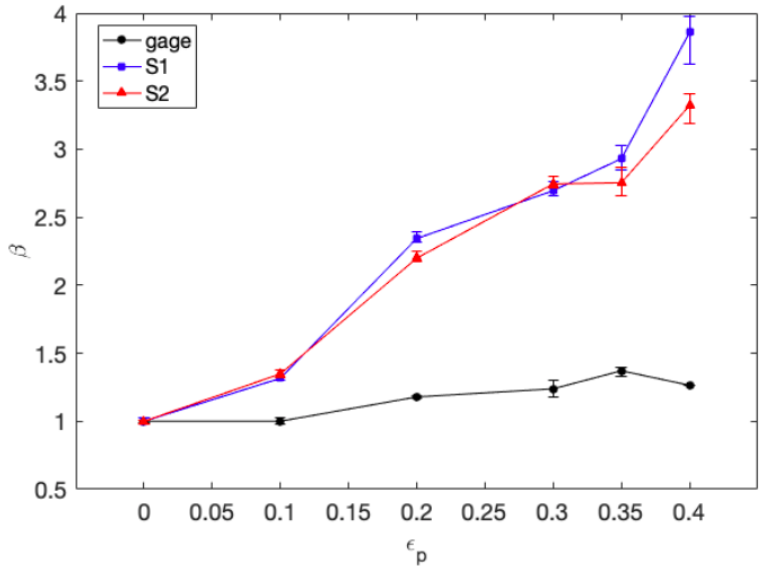

Figure 31. Acoustic nonlinearity coefficients experimentally measured for the gage area and the shoulder area.

CHAPTER 3

METALLURGICAL CHARACTERIZATION OF A572 STEEL MICROSTRUCTURE USING LINEAR AND NONLINEAR ULTRASONICS[1]

3.1 Background

The power generation industry is an industry experiencing constant innovations and developments. However, due to the extreme cost of most power generation equipment, that equipment must perform well for long periods, often under harsh conditions. Alloy steels used in such applications are exposed to high temperatures resulting in changes of microstructure that eventually weakens the mechanical strength of the metal component and could result in a system shutdown or possible catastrophic failure. It is then necessary to conduct routine non-destructive inspections to assess the mechanical integrity of the part or material. The state of the microstructure can provide such measurement, indirectly. The same problem arises in the manufacturing of critical components, where not only cracks, cavities, or surface defects need to be evaluated, but also the mechanical properties of the final product. Standard mechanical testing procedures, such as tensile testing or Charpy V-notch tests are not possible to make such an evaluation because of their destructive nature. It is through a microstructure assessment

[1]The content presented in this chapter is under the review in the Journal of Materials Engineering and Performance as "Metallurgical Characterization of a Low-carbon Steel Microstructure Using Linear and Nonlinear Ultrasonics"

using NDE methods that an indirect assessment of the mechanical reliability of the final part can be made.

Ultrasonic testing has been used to evaluate the microstructure and changes in the mechanical properties of materials where changes in ultrasonic velocity and attenuation of the waves are measured [102, 117]. The ultrasonic signal is influenced by the cumulative effect of Youngs Modulus change, orientation of grains, grain size, and density of the material. The problem arises when the received signal from the inspected area is influenced by the heterogeneity and anisotropy of the material [118, 119]. For example, the complexity of the microstructures in alloy steels, particularly in components that have undergone heat treatments or rolling during processing complicates the interactions between the ultrasonic variables and steel as observed by other investigators [120–122]. For example, in one of the early studies done on the effect of grain size and crystal texture on acoustic properties of 304 stainless steel, Grayeli et al. [123] found out that the wave velocity is higher in the outer surface of the annealed rolled bar than the center, while the attenuation was twice as large in the center as in the outer surface. They attributed these variances to the grain size and the crystal texture at these two locations.

The effect of material microstructure such as prior austenite grain size, grain size distribution, presence of inclusions, and phases on the linear ultrasonic wave velocity and attenuation has been extensively studied [67, 118, 124–126]. Ahn and Lee [124] studied the ultrasonic attenuation in low, medium, and high carbon steel. They observed that in the case of pure iron, the attenuation is influenced by the average grain size and that the scattering due to the presence of pearlite is greater than ferrite in hypo-eutectoid steels. Another study reported the

possibility of obtaining materials hardness by longitudinal and transverse wave velocities due to the microstructure heterogeneity in a half-cylindrical Jominy specimen [121]. Prasad and Kumar [102] determined that the deformation level and thermal treatment of forging, affect the UT velocity and attenuation, where the harder the material the fastest the velocity and it increased as the material was annealed. The attenuation was found to rise with increase in tempering temperature.

The type and volume fraction of phase in an alloy influences the mechanical properties of materials. In steels, strength, ductility, and hardness are affected by the ferrite volume fraction (which depends on carbon content) [73]. Heyman et al. [127, 128] studied the relationship between carbon content and higher order ultrasonic properties in four different types of steel samples and obtained the variations of ferrite phase content as a function of acoustoelastic coefficient for transverse wave propagation. In another study, Hurley et al. [33] discovered that β increases monotonically when the carbon content is increasing from 0.1 to 0.4% wt. while longitudinal wave velocity remained almost the same. They associated this change to the increase in the dislocation density imposed by the increase in the carbon content in martensitic steels. Salama et al. [109] studied engineering materials such as steel and aluminum alloys and concluded that both the acoustoelastic coefficient and the nonlinearity parameter decreased with the decrease of second phase precipitates in aluminum alloys.

Although there are several studies on the effect of material properties and type of microstructures on ultrasonic velocity and attenuation, there is lack of knowledge on the direct effect of phase volume fractions on the ultrasonic wave properties. The main objective of this study

is to correlate the volume fraction of ferrite and martensite in a heat-treated A572 Grade 50 steel with the ultrasonic parameters. The heat treatments were performed to ensure a fix prior austenite grain size and just varied the amounts of ferrite and martensite. Ultimately, the goal is to determine if UT technique can be used to do qualitative and quantitative metallography.

3.2 Technical Approach

3.2.1 Sample Preparation and Heat Treatments

A572 Grade 50 low alloy steel plates 9.53 mm thick with a chemical composition presented in Table III were machined to dimensions 225 × 50 mm^2. Figure 32 shows the geometry of the test samples used in this investigation; the two prongs sticking out of the test samples were machined to attach the samples to the grips of the tensile machine. The standard mechanical properties for this steel are shown in Table IV.

TABLE III. Chemical composition of A572 Grade 50 [129]

A572 Grade 50	C	Mn	P	S	Si
Weight %	0.23 max	1.35	0.03	0.03	0.4

Four samples were heat treated at different temperatures, three were intercritically annealed and quench in water to room temperature generating microstructures with different amounts of ferrite and martensite. One sample was completely austenitized at 980°C and quenched

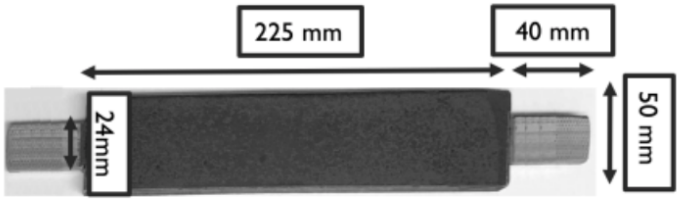

Figure 32. Sample dimensions used for the ultrasonic testing of A572 steel.

TABLE IV. Mechanical properties of ASTM A572 Grade 50 steel [129]

Yield stress	345 MPa
Ultimate Tensile Strength (UTS)	450 MPa
Elongation (in 2")	21 %

in water to room temperature to produce ∼100% martensite. The other three samples were austenitized first at 980°C for one hour and then intercritically annealed (see Figure 33) for one hour between A_1 and A_3 as described in Table V.

3.2.2 Metallographic Procedure and Volume Fraction Measurements

Separate specimens about 1 × 1 × 1 cm^3 were cut from each of the heat-treated specimens for microstructure analysis. They were prepared according to standard metallographic procedures to a surface finish of 1 μm and etched in a 2% Nital solution. Representative mi-

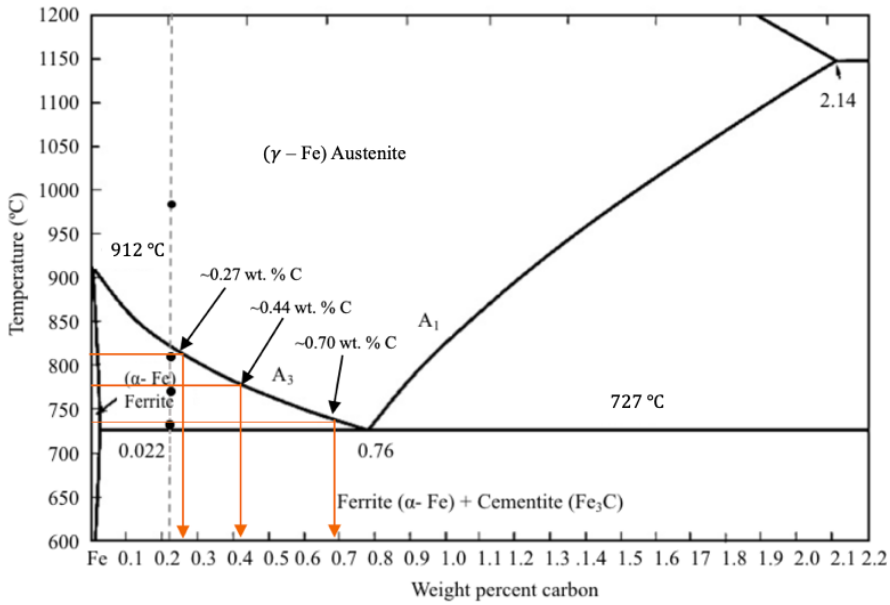

Figure 33. Partial Fe-Fe_3C equilibrium phase diagram depicting the four temperatures used for the heat treatments [130].

crographs were obtained from each of the samples using a Leica optical microscope to identify the microstructures corresponding to each heat treatment. Quantitative metallography was conducted using ImageJ software [115]. All the images were converted to 8-bit grayscale format as shown in Figure 34, and a threshold was applied afterwards (Figure 34b). Then, by using the Analyze tool the fraction of the black region (martensite) of the image was measured as seen in Figure 34c. More than fifteen (15) images at different magnifications were used to measure the volume fraction of ferrite and martensite. The theoretical amounts of these phases were determined by applying the Lever rule [130] in the Fe-C phase diagram in Figure 33.

TABLE V. Heat treatment applied to A572 Grade 50 steel specimens

Specimen Identification	**Heat treatment**	**Mean Measured Ferrite %**	**Theoretical Ferrite %**
980	980°C/1 hr./WQ	0	0
810	980°C/1 hr./810°C/1hr./WQ	31.88	27
770	980°C/1 hr./770°C/1hr./WQ	41.11	53
730	980°C/1 hr./730°C/1hr./WQ	74.30	70

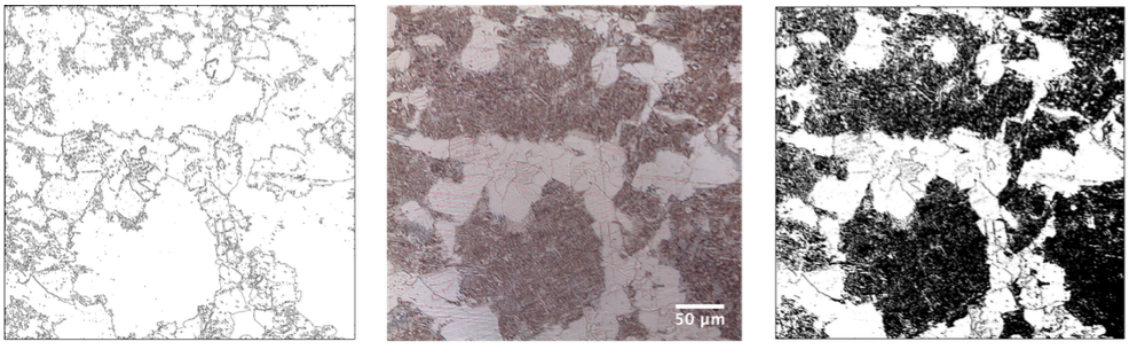

Figure 34. Processing of microstructure for sample 770 after heat treatment using ImageJ (a) original microscopic image, (b) image with threshold, (c) image ready for phase fraction analysis.

3.2.3 Mechanical Testing

To correlate the acoustoelastic coefficients and the wave velocity with the mechanical condition of the specimen, 5 Rockwell hardness measurements were performed on all samples after the heat treatment. In addition, the microhardness of the ferrite and martensite phases were measured for each heat-treated sample, to understand the effect of carbon content and phase volume fractions on each phase hardness.

Furthermore, each of the heat-treated samples were submitted to different elastic stress levels in the range 1 kN 100 kN at equivalent stress intervals to measure the acoustoelastic constant in each microstructural state.

3.2.4 Ultrasonic Testing

3.2.4.1 Immersion Linear Ultrasonics (Acoustic Microscope)

The test setup and the equipment used for the linear wave velocity measurement of A572 steel is exactly the same as section 2.2.3.1. For this purpose, 10 MHz transducers were used to measure TOF in the stress-free samples. Before any ultrasonic test the surface of all heat-treated samples were ground using 80-grit sandpaper to remove any surface oxide that might have formed and to ensure all samples have the same surface roughness. For each sample, waveforms were recorded from twelve points at the midsection of each plate to ensure the statistical randomness for velocity measurements. A MATLAB script was used to extract the arrival time or time of flight, relative to the input signal in time domain waveform. Figure 35 shows the schematic of the test-setup used in this experiment similar to Figure 15.

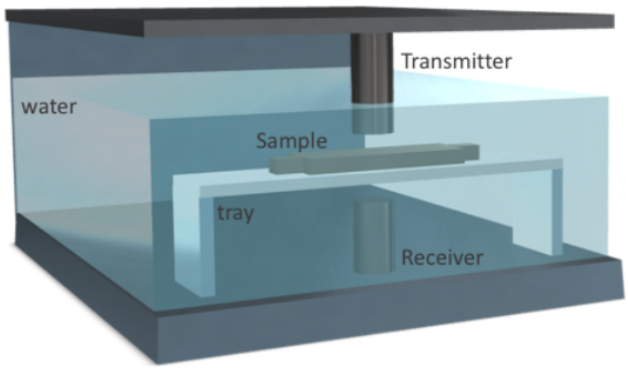

Figure 35. Schematic of the test-set up for linear ultrasonic measurement with Scanning Acoustic Microscope (SAM).

3.2.4.2 Nonlinear Acoustoelastic Measurements

Two types of data acquisition systems were used for the contact ultrasound tests: a handheld Pocket UT device manufactured by Mistras Group to generate the excitation signal, and a MSO2014 oscilloscope manufactured by Tektronix with 100 MHz frequency resolution to record the output of the ultrasonic transducer. The layout of the contact ultrasound is shown in Figure 36. This setup was selected based on the error estimation study [131], which showed consistent and repeatable results when the oscilloscope was used to record the ultrasonic signal compared to the handheld UT device. The ultrasonic transducers were coupled to the steel plate using oil and held in place using two clamp holders. A set of plexiglass wedges (variable angle beam wedges constructed by Olympus Inspection & Measurement Systems) was selected for wave generation. 1 MHz Panametrics A401S transducers were selected from Olympus to

match the variable angle wedges. The wedges were adjusted to 62.7° incident angle based on a previous investigation [60], and held at a relatively constant distance to prevent the elongation effect.

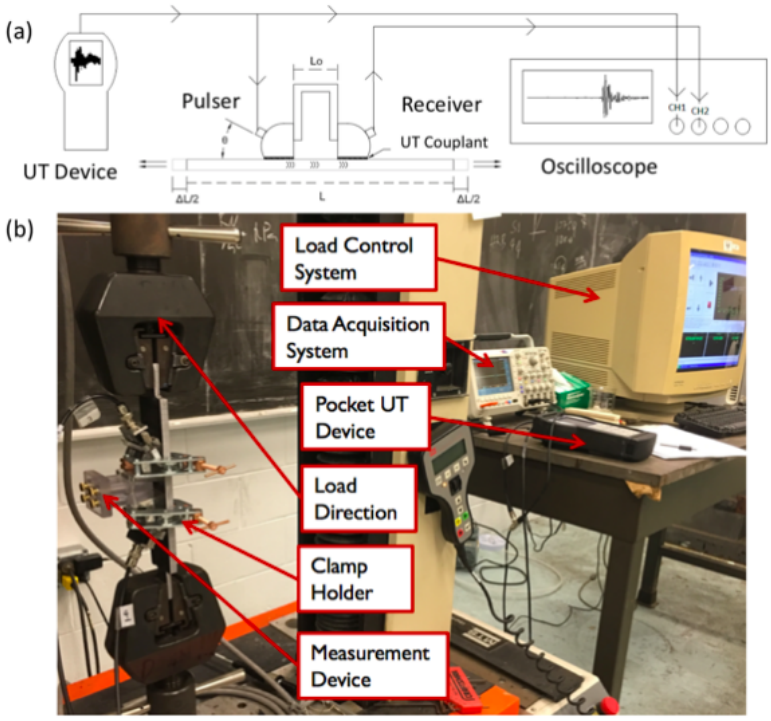

Figure 36. (a) Measurement system design layout for contact test in acoustoelastic measurement and (b) Test set up for nonlinear ultrasonic measurement with contact ultrasound.

In evaluating the effect of elastic strain on ultrasonic velocities, the heat-treated samples were elongated using an MTS tensile machine (model 1125) applying different elastic stresses. The tensile stress loading ranged from 1 kN to 100 kN in eleven evenly distributed loading steps. Figure 36b shows the test setup for the acoustoelastic measurements performed in-situ condition.

The ultrasonic data in the direction of stress was recorded for each applied stress to extract the acoustoelastic coefficient. The recorded time domain waveform was used to calculate the time of flight (TOF) of the ultrasonic wave which was further converted to velocity by having the exact thickness of the samples. By having the velocity at each stress level, the acoustoelastic coefficient was calculated for each sample.

3.3 Results and Discussion

3.3.1 Microstructural Characterization and Phase Volume Fraction

Figure 37 shows the microstructures attained for each of the four heat treatments. A fully martensitic microstructure was obtained in the sample heat treated at 980°C for 1 hour and water-quench to room temperature, as seen in Figure 37a. The samples which were intercritically heat-treated and quenched to room temperature, show a combination of martensite and ferrite as shown in Figure 37b, c, and d. The dark regions in all the micrographs correspond to the martensite and the light regions are pro-eutectoid ferrites that remain unchanged upon quenching.

As expected, the amount of martensite decreased with lower intercritical temperatures, since more of the prior austenite transforms to ferrite during the temperature drop from A_3

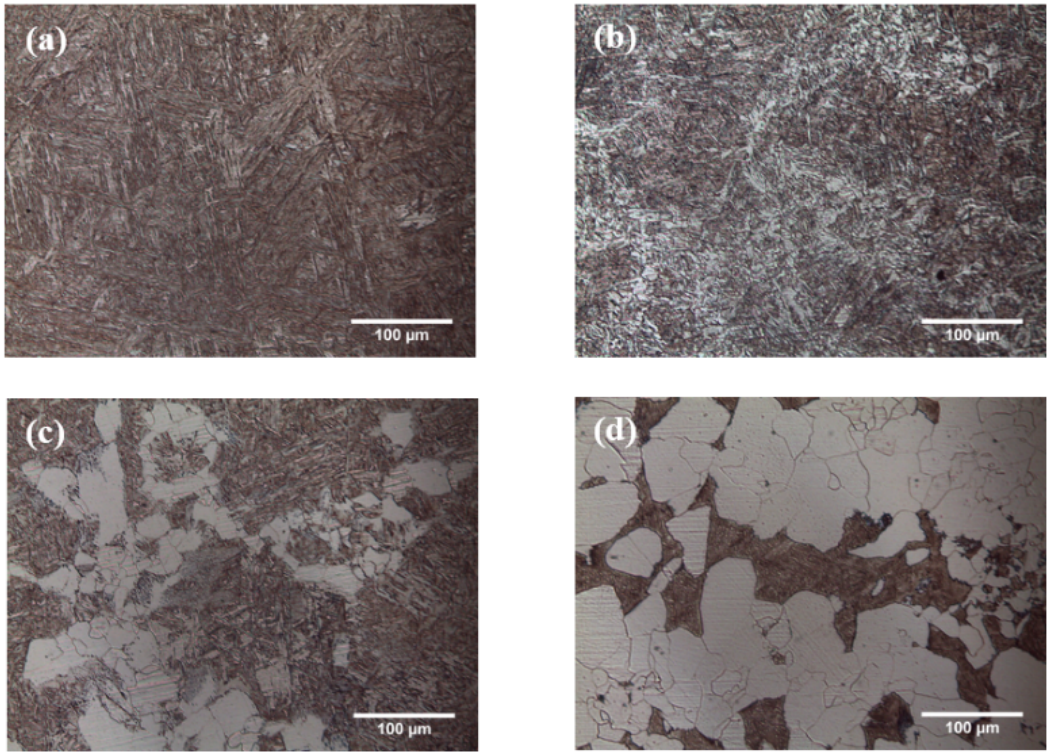

Figure 37. (a) Martensitic microstructure (sample 980); (b) Martensite and small amount of ferrite (sample 810); (c) Martensite and medium amount of ferrite (sample 770); (d) Martensite and high amount of ferrite (sample 730).

to A_1, leaving smaller volume fractions of austenite to transform to martensite on quenching. Note that all samples were initially austenitized at 980°C for the same duration of time to ensure all specimens are transformed entirely to austenite (γ phase) and have the same prior austenite grain size. In addition, all the samples were water quenched at the same temperature and therefore, the inevitable percentage of bainite in the microstructure is assumed to be the

same for all samples. Volume fractions measurements of martensite and ferrite phases for each specimen were conducted metallographically using ImageJ pro software.

Theoretical calculations of the phase amounts were also done using the Lever Rule [130] based on the ferrite and austenite carbon compositions obtained from partial phase diagram presented in Figure 33. Both, the experimental and theoretical measurements are plotted in Figure 38 as volume percentage of ferrite versus the heat-treat temperatures.

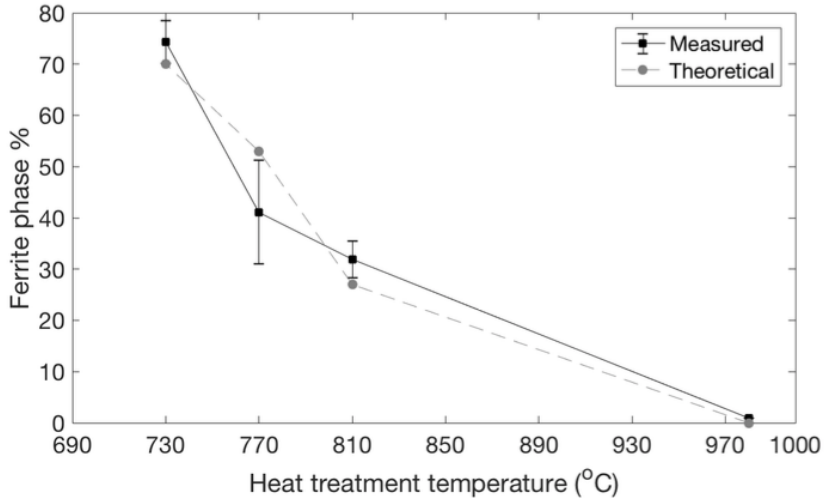

Figure 38. Measured and theoretical ferrite vol.% for different heat treatment temperatures.

Ferrite and martensite have different mechanical and physical properties, which would be expected to affect the linear and non-linear ultrasonic waves; hence, the volume fraction of each of the two phases would likely have an impact on such UT waves.

During microstructure analyses, the microhardness of the two phases in each of the heat-treated specimens was measured. This was performed to assess the subtle changes in hardness that would occur in the martensite due to the changes in the austenite carbon contents within the intercritical region, and to a lesser extent in the ferrite because of its limited solubility of carbon (0.022 wt.%C) as seen in Figure 33. Figure 39 shows the hardness of martensite as a function of carbon content for carbon steels containing 100% martensite [132]. The microhardness of sample 980 which is fully martensitic is consistent with the values reported for a 0.2 wt.%C steel in this figure.

Figure 40 shows the microhardness of martensite and pro-eutectoid ferrite, and the volume fractions of the martensite for each heat-treated specimen. The microhardness of ferrite, as the intercritical temperature drops, decreases significantly despite the minimum changes in carbon contents. Concurrently, the volume fraction of martensite in the specimens also decreases. This suggests that the microhardness of ferrite in the intercritically heat-treated specimens is affected by the straining caused by the residual stresses resulting from the martensite transformation. Note that no ferrite hardness is reported for the sample heat treated at 980°C, since the microstructure is fully martensitic.

The decrease in the martensite microhardness s influenced by the carbon concentration and the ferrite volume fraction. There is a drop in martensite microhardness of sample 810

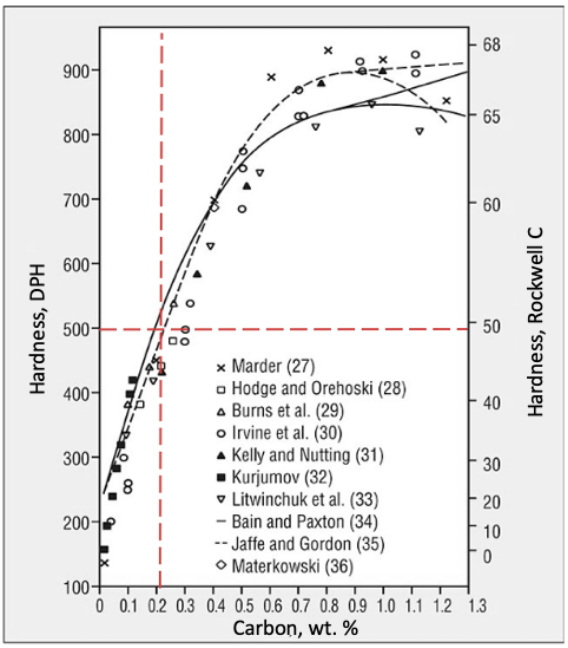

Figure 39. Martensite hardness as a function of carbon content of the steel. The dotted lines represent the carbon content and martensite microhardness of the specimen heat treated at 980°C and water quenched [132].

compared to sample 980 despite a small increase of about 17% in carbon content; however, the former specimen contains about ∼32% ferrite, implying that residual stresses introduced by the martensite transformation are being relaxed by the adjacent pro-eutectoid ferrite (see Figure 37b). Similar results are seen for the 770°C heat-treat sample, where there is about a two-fold increase in the austenite carbon content compared to sample 980. However, the pro-eutectoid ferrite is about 41%, which further reduces the straining caused by the martensite presence. The effect of the carbon content in the hardness of martensite is the predominant

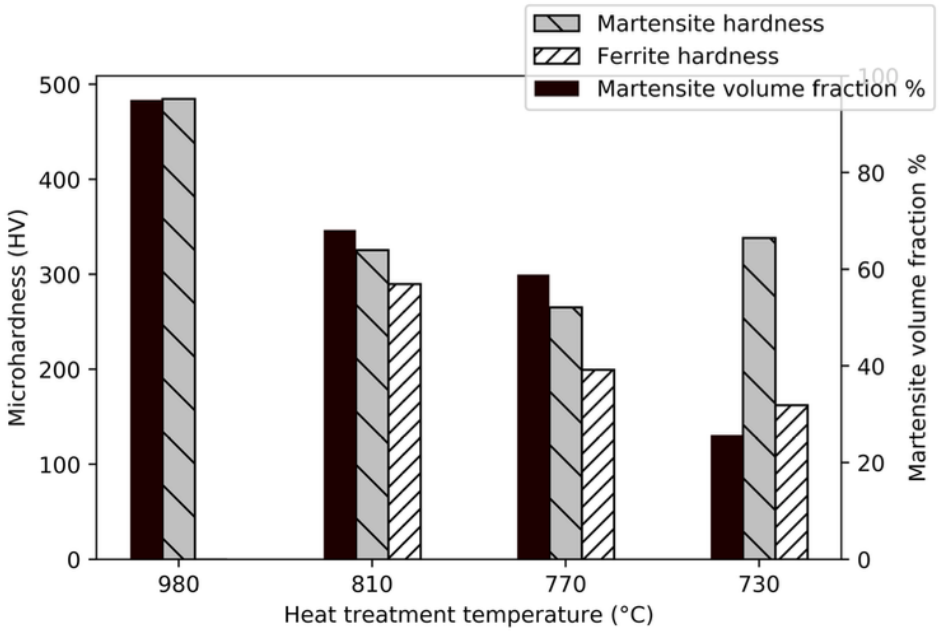

Figure 40. Dependency of ferrite and martensite hardness on martensite phase volume fraction.

factor in sample 730 compared to sample 770, where the carbon content increases by about 60% and the pro-eutectoid ferrite also increases to about 74%, but the microhardness increases from 265 HV to about 340 HV.

3.3.2 Linear Wave Velocity

The specimens thicknesses were measured initially to confirm their uniformity, despite being cut from the same plate. A total of ten measurements at different locations were performed for each sample that resulted in an average thickness of 9.0 ± 0.04mm (see Figure 41). The negligible variation in the specimen thicknesses implies that any possible changes in ultrasonic

properties are the result of the microstructural changes in the samples introduced by the heat treatments.

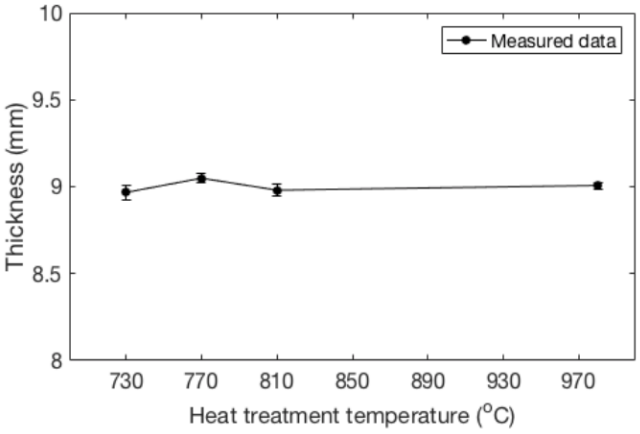

Figure 41. Average thickness of the A572 heat-treated samples at different intercritical temperatures.

The heat-treated specimens were first examined using immersion UT in the reflection mode with 10 MHz transducers. Figure 42 shows the received time domain waveforms for a measurement at a single location out of twelve locations tested. As mentioned earlier, the measured TOF corresponds to the wave path in the water, sample holder/tray, and test sample (Figure 35). Since the path distance of the wave propagation is constant in all three mediums, the

only variable affecting the arrival time is the microstructure in terms of the volume fractions of ferrite and martensite depending on the heat treatment experienced by the sample.

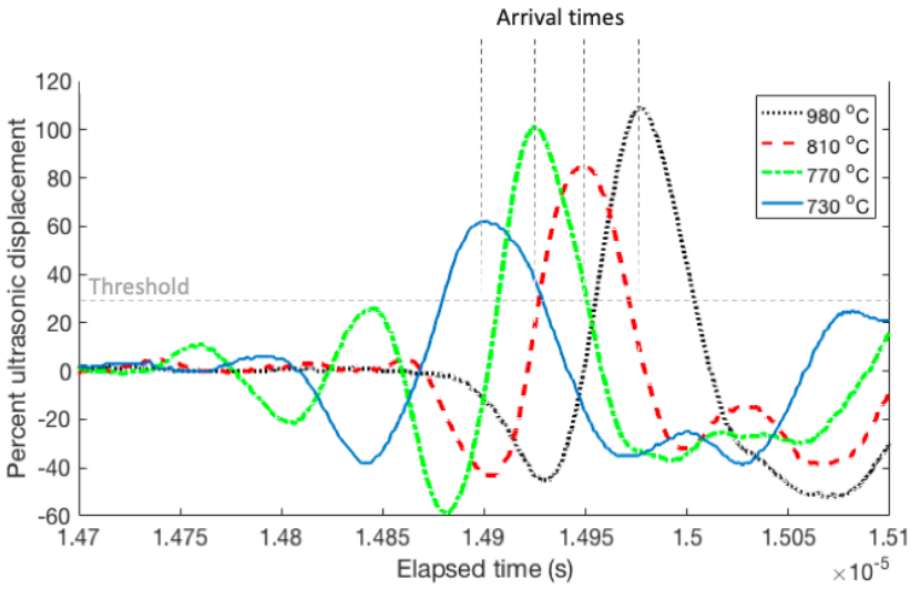

Figure 42. The received waveforms from a single data point for different intercritical temperatures.

As seen in Figure 42, the arrival times increase with higher heat treatment temperatures. The waveform corresponding to the fully martensitic microstructure, i.e. the sample 980, shows the longest TOF. TOF is used instead of linear velocity to reduce any other measurement errors.

The average time of flights measured for each of the samples is presented in Table VI and these are related to the heat-treating temperatures and ferrite volume fractions.

TABLE VI. The average TOF as a function of ferrite % in A572 steel

Heat treat temperature [°C]	**Ferrite %**	**Time of flight [μs]**
980	0	14.96
810	31.88	14.92
770	41.11	14.90
730	74.30	14.89

Figure 43 shows the time of flight and hardness change versus ferrite volume fraction. As indicated above, ferrite is much softer than martensite, hence by increasing the amount of martensite the hardness of the specimen increases. The time of flight, on the other hand decreases as the ferrite diminishes and martensite increases.

Obviously, the increase in the bulk hardness of the alloy delays the times of flight. Such delays are most likely the consequence of the interference caused by the increase in the dislocation density associated with the presence of martensite. In low carbon steels the martensite type is lath martensite, which is characterized by a high dislocation density. Martensite with carbon

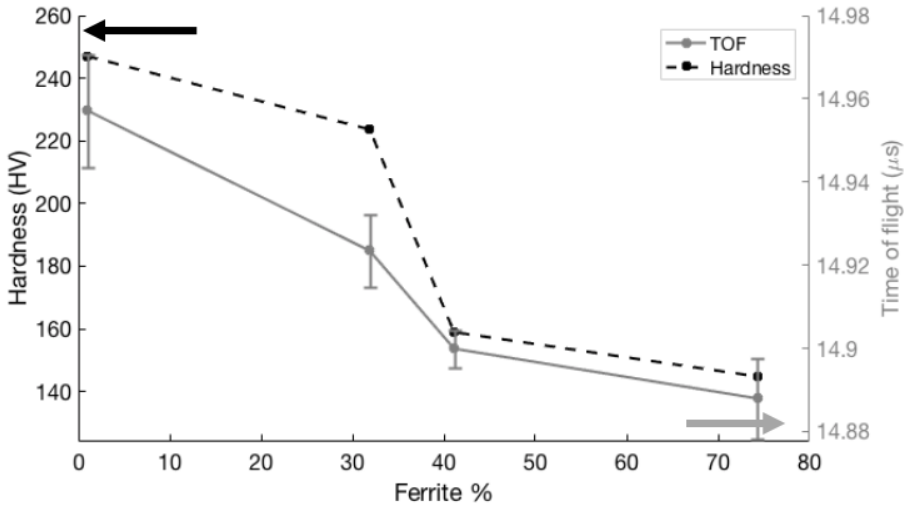

Figure 43. The variation of TOF and hardness with ferrite % in A572 steel .

content higher than 0.4 % carbon is referred to as twin martensite [132]. These findings are in agreement with the previously reported results in the literature which indicate that the hardness of the material has an inverse relationship with the velocity of the ultrasonic wave [133].

Another factor that may contribute to velocity changes are the interference caused by grain boundaries and thus grain size would have an effect on the wave velocity. This effect was eliminated by heat-treating all samples at the same initial austenitizing temperature and time. Furthermore, the intercritical temperatures are well below the temperature were significant grain growth can occur.

Previous studies [117, 125, 134, 135] showed that the lattice distortion and misorientation of the grains alter the elastic modulus in the direction of wave propagation which influences the wave velocity. The velocity decreases in the order of coarse pearlite/ferrite, bainite, and martensite microstructures. Martensite develops as a result of a diffusion-less shear transformation due to fast cooling or quenching, and it initiates at the prior austenite grain boundaries. The martensite consists of long and thin laths with different lattice orientations with respect to the prior austenite grains. The lath martensite produces a large tetragonal lattice distortion and high dislocation density comparable to cold-working a sample. In addition, martensite formation creates a high degree of randomization within the prior austenite boundaries, which results in an increase in elastic anisotropy of the prior austenite grains. Therefore, the decrease in velocity as alluded to before, is the result of the increase in dislocation density and lattice distortion [102,117,125,134,135]. The ferrite microstructure is less resistant to ultrasonic propagation due to the very low dislocation density, which in this case is introduced by the strain produced by the martensite. Furthermore, there is less variation in the orientation of the grains because of their equiaxed structure which makes the propagation of the wave easier [117].

Based on the linear ultrasonic results, the resolution of this NDE method to identify the changes in the microstructure of this carbon steel is relatively limited because of the small variations in the TOF's when substantial fluctuations in the proeutectoid ferrite and martensite were measured. This has led to utilize non-linear ultrasonics to determine if the later technique provides a better microstructural resolution.

3.3.3 Acoustoelasticity Coefficients (Non-linear Ultrasonics)

This alternative technique is based on changes of the sound velocity in an elastic material when subjected to an initial static stress. The relative time of flight (TOF) change as a function of stress state was used to obtain the acoustoelastic coefficient according to Equation 1.9. A MATLAB script extracts the second zero crossing after the peak amplitude in the time domain waveform [136] to calculate the variation of arrival time with stress. Figure 44 shows the shift in time domain waveform (close-up in Figure 44 inset) as one of the A572 as-received samples was subjected to four different stress values and corresponding strains. The microstructure of the as received sample consists of ferrite and pearlite. Therefore, this initial test was done only with the purpose of verifying the acoustoelastic coefficients obtained by the experimental procedure and comparing them to the theoretical value calculated by the mechanical properties of the as received sample.

To demonstrate the repeatability of the method, four as-received samples were tested using this procedure. The acoustoelastic coefficients for each sample as represented by the linear fit of the experimental data (relative TOF change versus stress) are -8.55$\times 10^{-7}$, -9.31$\times 10^{-7}$, -8.03$\times 10^{-7}$ and -8.86$\times 10^{-7}$ MPa^{-1}. Figure 45 shows the relative time of flight change with stress for these samples, which are close to the theoretical value for the shear wave velocity propagating in the direction of stress with polarization perpendicular to the stress direction. The K_T coefficient (acoustoelastic coefficient for shear wave) was calculated using Equation 1.8 and the second and third order elasticity constants reported for A572 in Table VII. For a steel plate with these properties the K_T is -8.89$\times 10^{-7}$ MPa^{-1}.

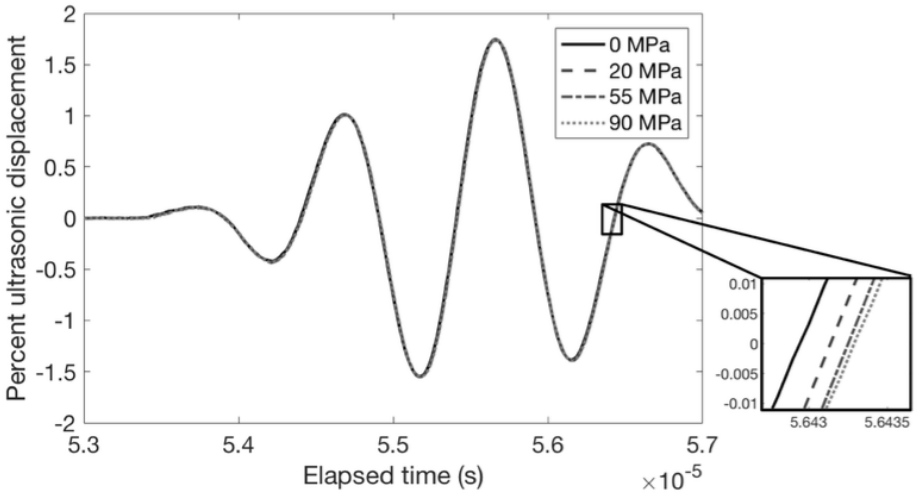

Figure 44. The time domain waveforms at four stress states recorded for as-received A572 sample.

The same procedure was repeated for four heat-treated samples and the results are summarized in Figure 46. The acoustoelastic coefficients for each sample as the ferrite phase content decreases are -1.06×10^{-6}, -1.26×10^{-6}, -2.07×10^{-6}, and -2.41×10^{-6} MPa^{-1}. The results show that with the decrease of the intercritical heat-treatment temperature, the ferrite phase increases which causes the slope (absolute value of acoustoelastic coefficient) to decrease. This observation demonstrates that the third order elasticity constants are affected by the characteristics of the microstructure which depends on the heat treatment procedure that results in changes in the ferrite and martensite volume fractions.

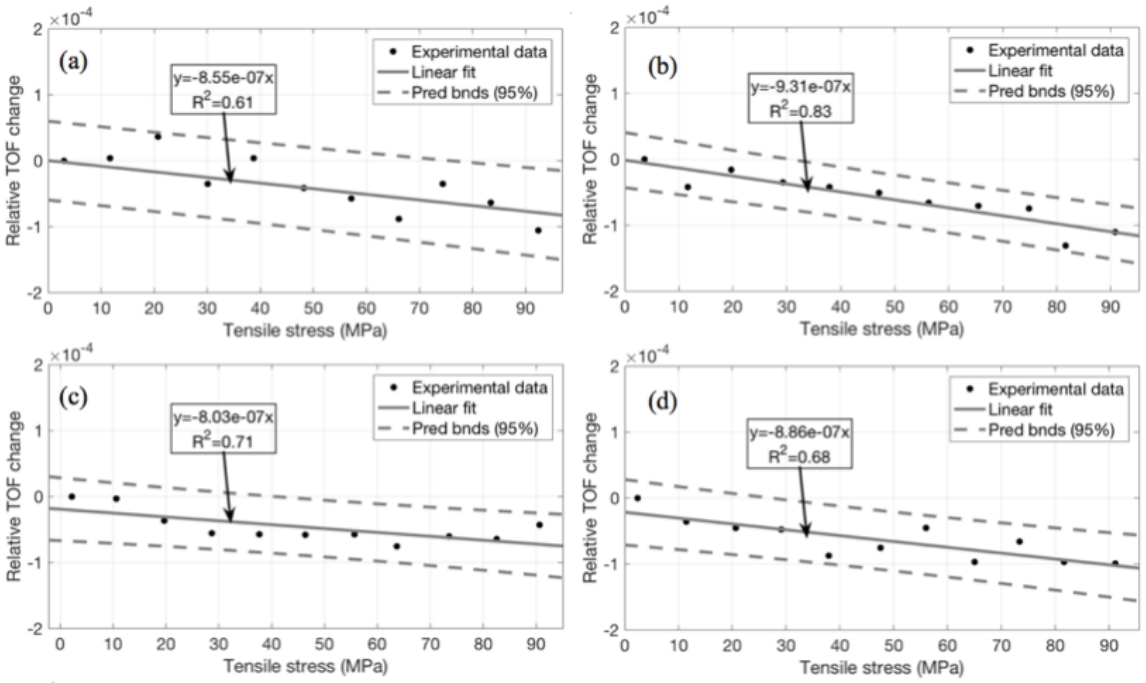

Figure 45. Relative time of flight (TOF) change with stress for four pristine samples (a-d).

TABLE VII. A572 material constants [60, 68]

Property	**A572 Grade 50 Steel**
Density [kg/m^3]	7850
Young's modulus [MPa]	200E03
Poisson's ratio	0.33
Lame constants [MPa]	λ = 150E03, μ = 75E03
Murnaghan constants [MPa]	l = -300E03, m = -620E03, n = -720E03

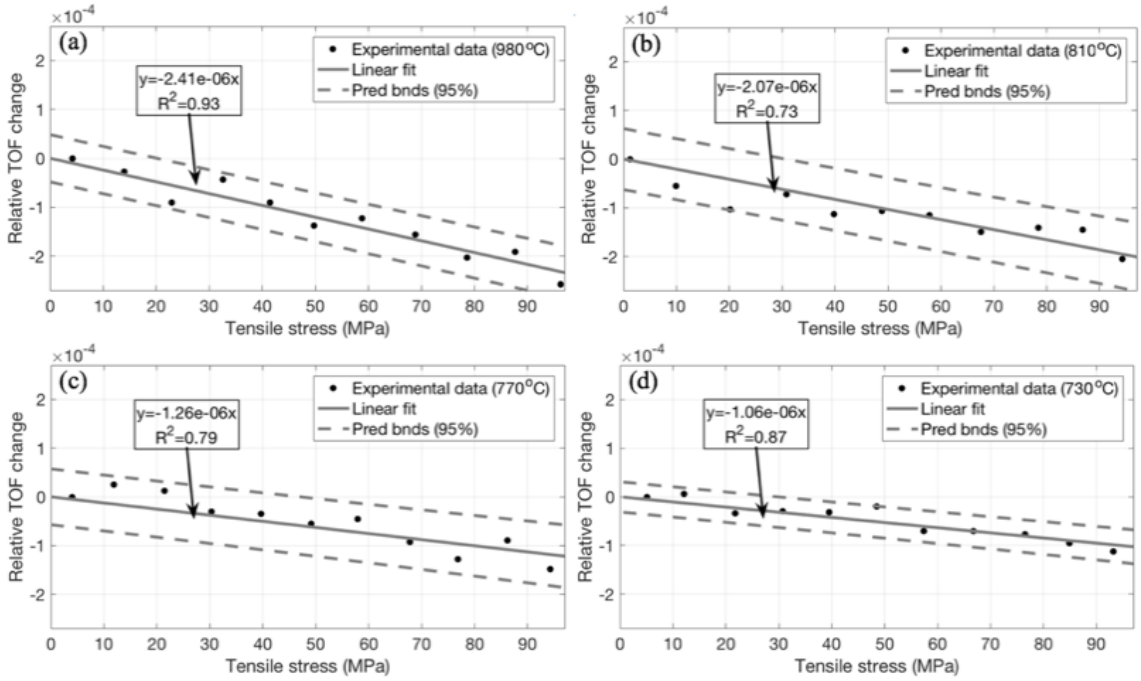

Figure 46. Relative time of flight (TOF) change with stress for samples (a) 980, (b) 810, (c) 770, (d) 730.

There is also a correlation between the variation of absolute acoustoelastic coefficients and the hardness data. Figure 47 shows decrease of the absolute acoustoelastic coefficients and hardness as the ferrite percentage for each specimen increase. The changes in hardness and acoustoelastic coefficient with change in ferrite content have similar trends. For plain carbon steels with ferrite/martensite microstructures, Figure 47 can be used as a reference chart. The hardness can be measured in the field, and then the acoustoelastic coefficient representing the

actual volume fractions of the phases of a low-carbon ferritic/martensitic steel plate can be identified.

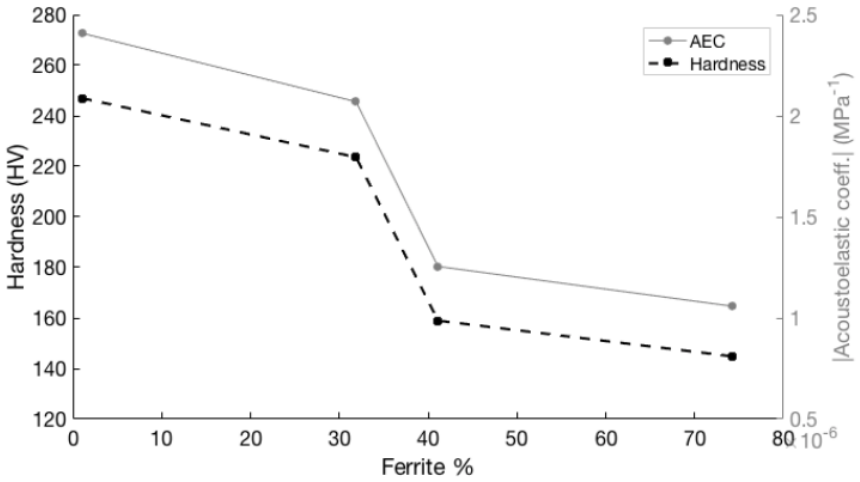

Figure 47. The variation of absolute value of acoustoelastic coefficient and hardness with ferrite volume fraction for heat treated A572 low-carbon steel.

3.3.4 Sensitivity of the Linear Wave Velocity and the Acoustoelastic Coefficient to the Change of Ferrite Phase C..ontent

Figure 47 compares the sensitivity of the linear wave velocity (time of flight - TOF), nonlinear ultrasonic property (acoustoelastic coefficient - AEC) measurements, and hardness with change in ferrite content. It shows that the change in the nonlinear ultrasonic property is sig-

nificantly larger than the linear ultrasonic property, which implies that the nonlinear ultrasonic wave velocity has higher sensitivity to changes in ferrite content.

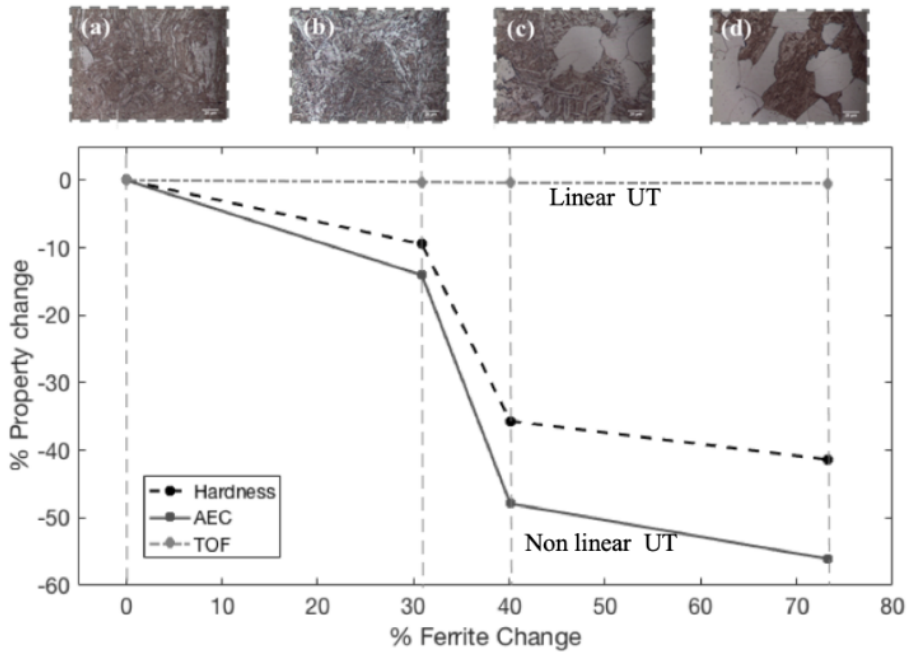

Figure 48. The sensitivity of change in time of flight, acoustoelastic coefficient and hardness with ferrite content change for samples: (a) 980, (b) 810, (c) 770, and (d) 730.

For instance, for 73% change in ferrite, the acoustoelastic coefficient increases about 56%, while the change in TOF is about 0.47%, similar to the values reported in the literature [109]. These results are expected since TOF only depends on second order elasticity constants which

are almost the same for the different heat treatment conditions. The acoustoelastic coefficient depends on both the second and third order elasticity constants, and the third order elasticity constants of the material are much more sensitive to the changes in the material microstructure, such as the change in the ferrite volume fraction with heat treatment [127]

CHAPTER 4

CREEP DAMAGE DETECTION IN 410 STAINIESS STEEL USING LINEAR AND NONLINEAR ULTRASONICS

4.1 Background

As mentioned in 1.1, the urge to understand the evolution of creep damage and need to extend the service life of structural components exposed to elevated temperatures, demands an accurate in situ NDE assessment of the metallurgical and mechanical conditions of the material. Among the NDE methods, ultrasonic testing has undergone significant research and improvements in the past decades. Thus, the ultrasonic technique is a key method to predict the remaining life of the components or prevent the premature retirement of components in service, such as in power generating plants. During the past few decades, most of the research was focused on damage detection mainly using linear ultrasonic methods by means of wave velocity measurements. One of the earliest investigations on UT-creep damage assessment using wave velocity was done by Brthe [137] which showed a 15% decrease in velocity for the pure copper samples under different levels of creep damage at 250°C. However, they could not include the effect of cavity formation on the wave velocity variation. In another experiment by Stigh et al. [138],they observed an 8% velocity decrease for the highest creep damage after 7800 hours in AISI 316 austenitic stainless steel. The same material (316 SS) was tested by Berthaud [139] at 600°C but for a shorter time, 54 hours, which led to much smaller change in velocity compared

to Stigh [138]. Ohtani et al. [140] studied the microstructural evolution of 2.25 Cr-1Mo steels during creep at 650°C using shear wave attenuation and velocity by electromagnetic acoustic resonance (EMAR) method. In their work, attenuation showed a peak after 60% of the creep life regardless of the applied stress. They interpreted this change in attenuation as the change in dislocation mobility and rearrangement, which absorbs more ultrasonic energy by transforming to subgrain boundaries.

Nonlinear ultrasonic measurements have proved to be more sensitive to damages in the material at early stages, which led to a shift in UT research from linear to nonlinear ultrasonic measurements in the recent years [35, 46, 141, 142]. It has been shown that this method is capable of detecting small microstructural changes, such as micro void nucleation and growth, especially during fatigue damage. A study on fatigue damage detection was presented by Yost et al. [46, 143] in which they showed a strong interaction between the acoustic waves and dislocation dipoles during the fatigue damage in precipitation hardened 2024 aluminum alloy. Fatigue damage was also investigated in a high strength Al-Cu-Zn-Mg alloy using harmonic generation method by Jaya Rao et. al. [142]. They observed two peaks for at two different life cycles of the sample. They explained such observation based on the dislocation dynamics and dislocation-crack interaction during the fatigue process and it was further shown to have a good correlation with the fatigue life progression. Ogi et. al. [35] studied the ability of the nonlinear ultrasonics for fatigue damage detection in steels using noncontact ultrasonic surface waves. The same study on the fatigue metallic samples was done by Campos-Pozuelo and Gallego-Juarez [144] using a new experimental procedure which showed a notable increase in

β compared to the intact samples. In addition, they showed the higher sensitivity of the third harmonics in fatigue damage detection compared to the second harmonics. Another study done on fatigue damage detection was conducted by Sagar et. al [15] showing the increase of the second harmonic to a value close to the first harmonic (95%) during fatigue crack initiation in high cycle fatigue. Nagy et al. [16] conducted cyclic bending to generate fatigue damage in different materials such as plastics, metals, composites and adhesives, and concluded that NLUT can be utilized as a more sensitive technique to detect early fatigue damage in materials.

Based on this review of the literature, significant research has been done on nonlinear ultrasonics to assess fatigue damage detection in conjunction with the dislocation increase. However, research on the microstructure evolution of metal alloys for long-term exposure at high temperatures under stress, i.e. creep, is significantly less. The assessment of creep damage is complicated due to the combination of an initial strain hardening, followed by a recovery/recrystallization phenomenon accompanied by microstructural changes under elevated temperatures. In the recent years, increasing number of researches have been done on creep damage detection using various nondestructive evaluation methods, including linear and nonlinear ultrasonics, as summarized in the following paragraph.

The accumulation of the creep damage in boiler exchange tubes of a fossil fuel power plants weldments was investigated by Ohtani et al. [36] which showed an increase in the amplitude of the ultrasonic wave around the heat-affected zone (HAZ) which was attributed to the areas of high creep void density in those samples. In another study [19] he assessed the change in the wave attenuation using electromagnetic acoustic resonance (EMAR) to detect the creep

damage in Cr-Mo-V steel at 650°C under various stresses using creep times between 25 and 50 hours. Their results showed maximum attenuation occurring at 30% creep life and the minimum at 50%. This change in attenuation was attributed to the dislocation damping that happens during the creep damage for the mobile dislocations. The presence of equiaxed cell structures and high dislocation density was reported as the reason for high attenuation while the formation of sub-grains and decrease in the dislocation density was accounted for the decrease in attenuation using EMAR method. Raj et al. [12] showed that in 9Cr-1Mo thermally aged samples, the formation and coarsening of the precipitates is an important aspect of the creep process that eventually leads to cavity formation and micro cracks. Their results showed that the precipitation formation has a stronger effect on wave velocity than voids and wave velocity changes non-monotonically with the aging time, therefore making the interpretation of the data harder. While it has been shown that the ultrasonic velocity is more sensitive than the attenuation, the limitation of the conventional ultrasonic features is that the defects generated by the creep should be significant such that the method can be sensitive to. The problem becomes more pronounced when the creep damage is in the early stage and reveals initial microstructural changes [22]. Valluri et al. [7] investigated the effect of creep damage in 99.98% pure copper using both linear and nonlinear ultrasonics. They found out that the nonlinear ultrasonic parameter can change up to 1200% for the fractured creep samples compared to their pristine sample, while the linear velocity only increased about 10-30% for the same creep damage level. In the investigation by Baby et. al. [22], they assessed the effect of creep damage on the second harmonics of a titanium alloy which showed that β increases to a maximum level

with increasing creep, while it decreases at final stage towards rupture. The overall change in β was 200% compared to the pristine condition; this shows a significant sensitivity of nonlinear UT compared to the linear UT measurements. In addition, they observed a change in β along the gage length and they attributed it to the variation in creep damage along the gage length of the specimen. Xiang et al. [145] used the nonlinear ultrasonic measurement to investigate the creep degradation of titanium alloy at 600°C. Their result showed an "N" shape response of β as the creep time increased. They further associated this change in β with the microstructural variations during the creep for this specific material. They concluded that the precipitate-dislocation interaction is the most dominant factor governing the change in β during the creep. More recently, Balasubramaniam et al. [28] employed a low-amplitude nonlinear ultrasonic technique and higher harmonics to characterize the creep damage in copper They showed that the nonlinear response increases as the creep damage accumulates. In addition, they proved that the third harmonic response is the most sensitive parameter to the creep-generated dislocation during creep damage.

AISI 410 stainless steel is a commercial low carbon martensitic stainless steel with a wide application due to its high toughness, strength, and corrosion resistance. 410 stainless steel can be fully transformed to lath martensite even in a very low cooling rate such as air cooling [146]. The creep damage in 410 SS was previously studied at UIC by Polar et al. [13, 147] using magnetoelastic NDE method which monitors the changes in the magnetic properties of the ferromagnetic material due to the internal stress state. They showed that the strain in the martensitic lattice of the 410 stainless steel is decreasing with the progress of creep due to the

tempering effect. In addition, they observed that this material becomes magnetically softer as the creep damage develops due to the fact that the highly strained lattice or the excess carbon atoms in the martensite microstructure act as the pinning points which makes the material harder to magnetize. Furthermore, they observed a magnetic flux drop for the samples that went through necking, although these samples were experiencing more damage. The reason behind this drop was found to be the presence of the voids in the matrix in addition to the coarsened carbides compared to the uniform creep samples.

From this review of literature on the UT research conducted on creep, there are two important factors that seems to have been ignored in previous studies: (1) the initial state of the materials microstructure, which in the case of a low-carbon alloy steel, can vary considerably for an annealed condition to a hardened or hardened and tempered state, especially for martensitic steels. This initial microstructure affects the nonlinearity response of the ultrasonic wave significantly since other factors such as tempering of the martensite, carbide formation, and release of lattice strains contribute to the change in β response. (2) Most of the previous researches have evaluated the β response based on the creep time rather than creep strain or strain rate, assuming that all the samples are following the same master creep curve.

In the current research, not only the creep damage behavior of 410 SS has been investigated with both linear and nonlinear ultrasonics, but also these two additional factors have been taken into account corresponding to a more realistic situation that can be applied to the components servicing under the stress at high temperature for extended periods.

4.2 Technical Approach

4.2.1 Materials and Sample Preparation

AISI 410 stainless steel (SS) is a commercial low carbon martensitic stainless steel with a wide application due to its high toughness, strength and corrosion resistance. 410 SS can be fully transformed to lath martensite even in a very low cooling rate such as air cooling [146]. This material was chosen to investigate the changes in the linear and nonlinear ultrasonic produced by creep damage at different strain levels. Table 8 and Table 9 show the typical composition and mechanical properties for this alloy according to the standard ASTM A240.

TABLE VIII. Chemical composition of 410 stainless steel [148]

410 SS	**C**	**Mn**	P	**S**	**Si**	**Cr**	**Ni**
Weight %	0.08-0.15	1	0.04	0.03	1.00	11.5-13.5	0.75

Several 410SS samples were submitted to 10 different heat treatment sequences and the microstructures were characterized. The objective was to precipitate different carbide sizes by tempering the material since the presence of carbides in the matrix can act as source of void formation during creep, and thus accelerate creep in the samples. The microstructure of the samples before tempering was martensitic since they were austenitized and quenched. The heat treatment procedure consisted of austenitizing all samples at 980°C for 30 minutes followed by

air cooling to generate a uniform martensitic structure and tempering at 650°C for two hours to precipitate carbides in the lath martensite matrix. The carbides are expected to be of the $M_{23}C_6$ type [149].

TABLE IX. Mechanical properties of AISI 410 stainless steel [148]

Yield stress	205 MPa
Ultimate Tensile Strength (UTS)	450 MPa
Elongation (l_0 = 2")	20 %

The creep samples were machined from a 7.1 mm (0.28") thick to the dimensions shown in Figure 49 according to the ASTM E139 standard [150].

4.2.2 Generation of Different Levels of Creep Damage in 410 SS

Heat treated samples were cleaned with grit size 400 sand paper. The samples were set up in the creep machine, placing an extensometer at the center of the gage length to measure the strain during the creep test. The whole setup was placed inside the furnace in the creep machine and three external thermocouples, type K, were attached to the gage length of the sample inside the furnace to get a real reading of temperature and to ensure the uniformity of the temperature along the gage length. The creep tests were carried out using an ATS 2710 creep testing machine connected to a DATAQ DI-245 data acquisition system. Windaq software

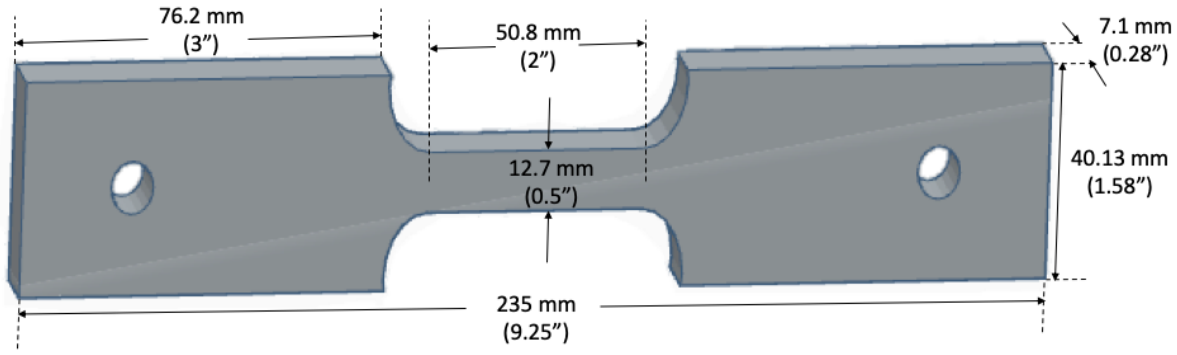

Figure 49. Creep sample dimensions.

was used to acquire the voltage from the transducer connected to the extensometer and was transformed to micrometer using a calibration system. Initially, three trial creep-rupture tests were performed up to failure at 620°C and three different stresses to attain a complete creep curve showing the three stages of the creep while minimizing the rupture time. These three initial creep test conditions and their corresponding rupture times are summarized in Table X. Figure 50 shows the creep curve for the first two failed trials with short creep duration. As seen in this figure, the first two trials led to a short creep rupture with an immediate transition to the tertiary stage.

Based on these initial tests, the stress of 150 MPa and the temperature of 620°C were chosen as the desirable creep condition to generate a creep curve representing gradual changes in the strain and thus producing specimens with different levels of damage.

In addition to the creep samples, rectangular samples 76.2×12.7×7.1 mm^3 (with the same width as the gage length of the creep sample) were also inserted inside the furnace as shown in Figure 51. The samples were aged at the same temperature as the creep sample for the same amount of time but without any loading. In this case, changes in the microstructure of the samples due to aging at the creep temperature and time can be monitored without the presence of any stress and thus changes only due to temperature and time exposure can be assessed separately, e.g. grain growth and carbide precipitation.

TABLE X. Creep-rupture times of 410 SS at 620°C and 3 different stress levels

Trial #	**Temperature (°C)**	**Stress (MPa)**	**Rupture Time (hrs.)**
1	620	200	42
2	620	170	92
3	620	150	725

Based on the creep-rupture curve of 410 SS at 150 MPa and 620°C, 5 other creep samples were tested under the same condition but for fractions of the rupture time. The purpose was to have samples corresponding to different stages of creep, particularly steady-state creep and the very beginning of the tertiary creep. It should be noted that in some cases, the tests were stopped earlier than the scheduled duration because the samples were creeping at a much faster rate compared to the initial tested reference sample. Although the material and the initial (pre-

creep) heat treatment were the same for all the samples, their creep curves were not following the exact same trend. This can be due to the internal defects of the material, surface defects, manufacturing process (i.e. samples coming from different heats or different rollings), and due to the complexity of the creep procedure. All the samples were furnace cooled after interrupting the creep loading.

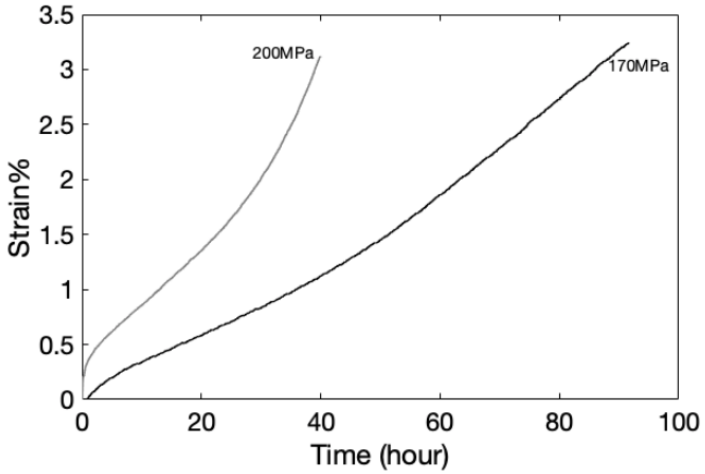

Figure 50. Creep curve of the first two trials at 200MPa and 170MPa, and 620°C.

Figure 51. Locations of creep and aged sample inside the furnace for creep rupture test.

4.2.3 Ultrasonic Testing

4.2.3.1 Immersion Linear Ultrasonics (Acoustic Microscope)

The test setup and the equipment used for the linear wave velocity measurement of A572 steel is exactly the same as section 2.2.3.1 In the case of creep samples, reflection mode was selected using 15 MHz transducers for mapping the change in thickness and thus, localized damage. Before the UT test, the thin oxide film formed on surfaces of all the samples during creep were ground using a 400-grit sandpaper. This was done to create a smooth surface and prevent wave distortion.

4.2.3.2 Nonlinear Ultrasonics Measurements

The test setup used for the Nonlinear Ultrasonic measurements of the creep samples are also the same as section 2.2.3.2. The only difference was the use of Tablet UT device (Figure 52) manufactured by Mistras Group Inc. which is a more powerful tool compared to the pocket UT used in the previous sections. The input signal was a 10-cycle tone burst input signal at the frequency of 2.25 MHz and the amplitude of 100 V. The received time-domain signal is recorded by the same Tablet UT device at a sampling rate of 100 MHz. A band pass filter of 0.5-20 MHz is applied to the received signal. To improve the signal to noise ratio, 200 received signals are averaged this time, recorded by the UT system, and then the averaged signal is processed using MATLAB software. The acoustic nonlinearity parameter was extracted using FFT on the time domain waveform.

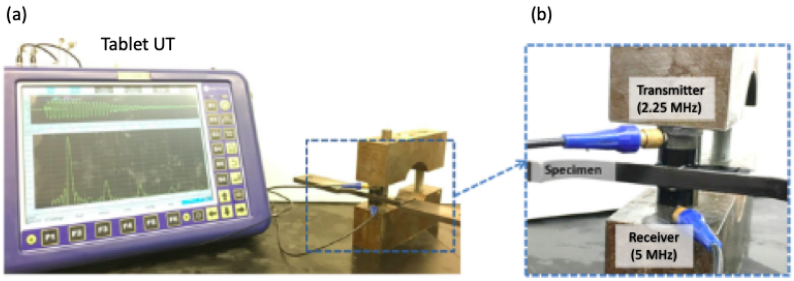

Figure 52. Test setup for NLUT experiment of creep samples, using Tablet UT.

4.2.4 Microstructure Characterization and Void Measurement

Following creep test and ultrasonic measurements, both aged and creep samples were sectioned and prepared following standard metallography procedure according to ASTM-E3 [151]. Optical microscopy was done using a Leica DMLM microscope. The etchant used to reveal the microstructure for 410 SS was Kalling' No. 2 (12 grams cupric chloride, 20 grams of Hydrochloric acid, and 225 ml of alcohol).

4.3 Results and Discussion

4.3.1 Creep Damage Assessment in 410 SS

Figure 53 shows the creep-rupture curve of 410 SS that failed after 725 hours under applied stress of 150 MPa at 620°C. The figure demonstrates different creep stages, rupture time, and strain at fracture. The plot depicts the three typical creep stages, with a total strain of about 7.9 %. From this creep curve, approximate test creep times and strains were selected corresponding to the secondary and tertiary stages of creep as noted in Figure 53. The proposed creep times are shown as red dots on the plot.

During the interrupted creep tests, the strain was closely monitored since it is very unlikely that identical creep plots can be obtained for the same material. This can be observed in Figure 54 were none of the partial creep curves could be superimposed over the referenced creep-rupture curve. It needs to be recalled that all samples were heat treated following the same procedure, so the starting microstructure is the same for all test specimens. These results are evidence of the complexity of the creep mechanisms and the impact of any heterogeneities in composition, microstructure, or localized defects on the final outcome. The creep strain

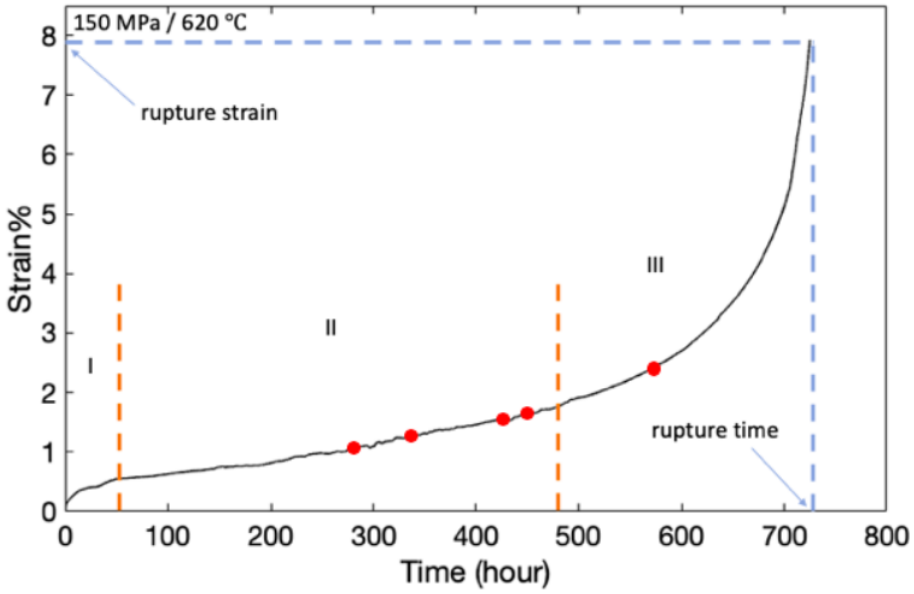

Figure 53. Creep-rupture curve of 410 SS at 150 MPa and 620°C, showing three stages of creep, the creep rupture strain, and the time to failure.

monitoring was done such that both creep stage and strain level were considered. Table XI summarizes the test durations and the corresponding strain percentage of each sample tested at 150 MPa and 620°C.

In order to discriminate between the secondary and tertiary stage of creep experienced by samples, the creep **rate** corresponding to each specimen was plotted as a function of time, shown in Figure 55. In this figure, the transition from the secondary to the tertiary stage of creep was faster for sample C2, C3, C4 and they did not follow the same trend as the Ruptured sample, sample C1, and sample C5. These samples entered the tertiary stage after about 200

TABLE XI. Partial creep strain of the test samples at different creep rupture fractions at 150 MPa and 620°C

Sample	**Time (hrs.)**	**Time ($t/t_{rupture}$)**	**Strain (%)**
Ruptured	725	1	7.92
C5	580	0.8	2.00
C4	450	0.62	3.04
C3	437	0.6	3.59
C2	335	0.46	2.01
C1	290	0.4	0.81
HT (heat treated sample)	0	0	0

hours which led to termination of the test earlier than scheduled. For example, sample C2 was stopped after 335 hours but at the same strain (2%) as sample C5. In this case, the variations of ultrasonic results for two samples with similar strain levels but different creep durations are comparable. The slightly larger damaged part in sample C2 can be due to early entrance into the tertiary stage. Samples C2, C3, C4 were made from the same material and went through the similar heat treatment process but was cut from a second plate (different heat) produced by the same manufacturer. Therefore, there may be some processing parameters affecting the creep performance under the same condition which is an important concern in creep life prediction, and this makes the case for the relevancy of in-situ monitoring of the damage level.

Figure 56 shows the strain and strain rate of different creep samples alongside each other, which helps to interpret the results in the next sections not only based on the strain level,

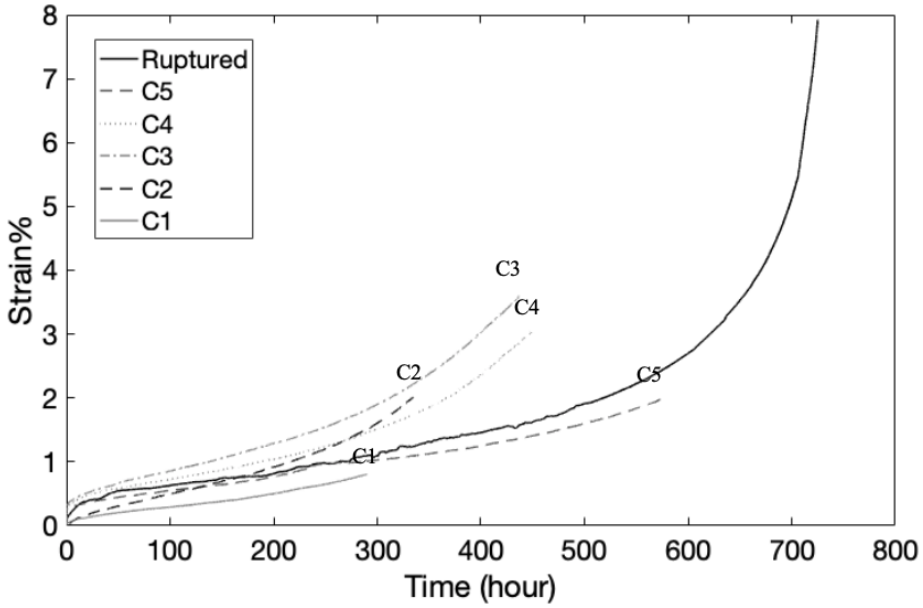

Figure 54. Relative creep curves of the samples stopped at different strain levels.

but also based on the creep strain rate. This is presented to assess the balance between work hardening and recovery mechanisms active in each sample.

As mentioned earlier, to separate the mechanical straining from the microstructural changes that the specimen undergoes, dummy samples were placed next to the creep samples for the duration of each creep test. This would also help to provide more insights into interpreting the results obtained from the UT tests.

Furthermore, Rockwell hardness measurements were made for both the aged and creep samples in their pristine condition and have been plotted in Figure 57. Based on the hardness

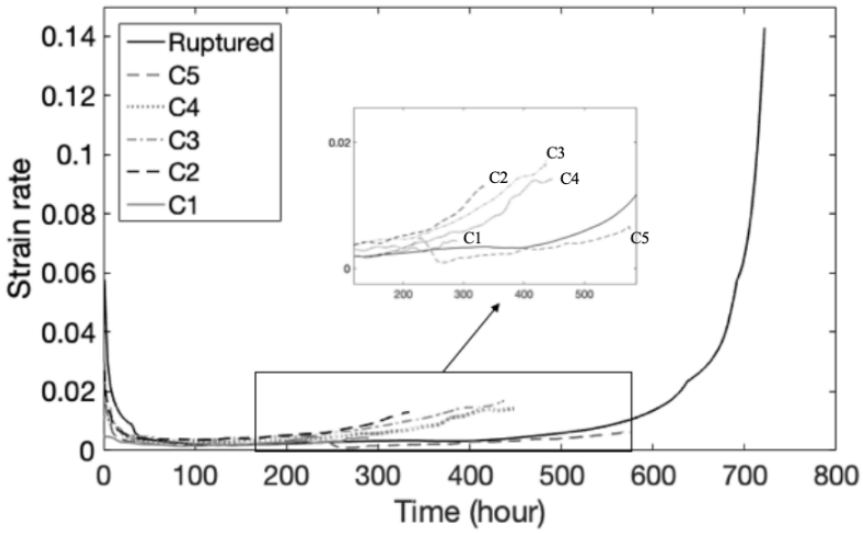

Figure 55. Relative strain rates of the samples stopped at different strain levels.

results, it seems that all samples prior to creep test had almost the same hardness, indicating the same microstructures.

4.3.2 Creep Damage Detection in 410 SS with Ultrasonics

4.3.2.1 Linear Wave Velocity

Figure 58 shows the corresponding images of time of flight (TOF) variations for each creep sample, C1 to C5, exposed to different levels of creep as well as the sample after heat treatment and the pristine sample. The exact TOF was extracted from at least 10 points along the gage length to find the maximum change of TOF along the gage length and thus calculate velocity. The color changes observed in different specimens are related to the time of flight measurements.

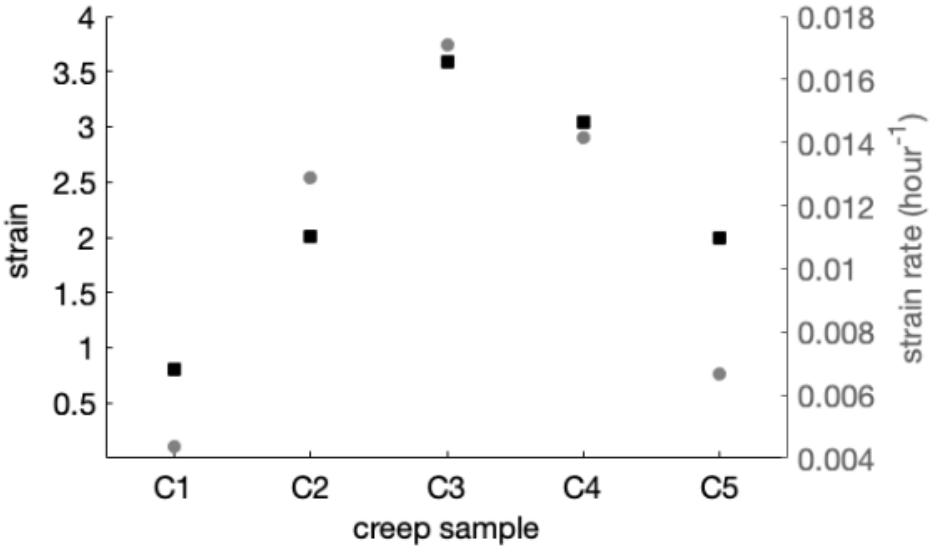

Figure 56. Strain level and the strain rate for different creep samples in Table XI.

Note that the pristine and heat-treated samples present a uniform color throughout the gage length. This is expected since no deformation (applied creep) was applied to either specimen; however, the difference in uniform color might be a reflection of possible residual stresses still present in the heat-treated sample due to the martensite formation despite undergoing tempering. The negligible variation of about 0.016 μs in TOF along the gage length of the heat-treated sample can be due to surface preparation. Sample C1 was exposed to the lowest creep damage and displays a uniform color throughout the gage length, which again is an indication of a uniform deformation. It is also observed that C1 presents a darker color than the pristine and

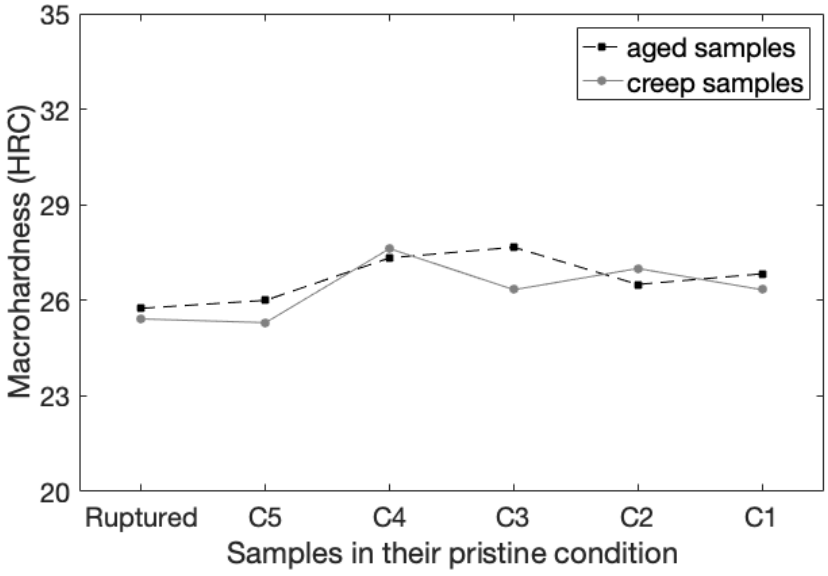

Figure 57. Macro-hardness measurements for the creep and aged samples after the initial heat treatment and before starting the creep process.

heat-treated samples, and it shows the minimal change of TOF (0.021 μs) through the gage length. The color changes observed for all other creep samples, i.e., orange, yellow, and green colors are not only an indication of an increase in TOF, but also signal localized damage in these samples. As is seen in Figure 58, sample C3 shows the longest TOF with a difference of 0.105 μs between the center of the gage length and the grips. It was also observed that even though samples C5 and C2 both underwent creep for different durations of 580 and 335 hours, respectively, they both reached a comparable strain level and thus, similar change in TOF as observed along the gage length in Figure 58.

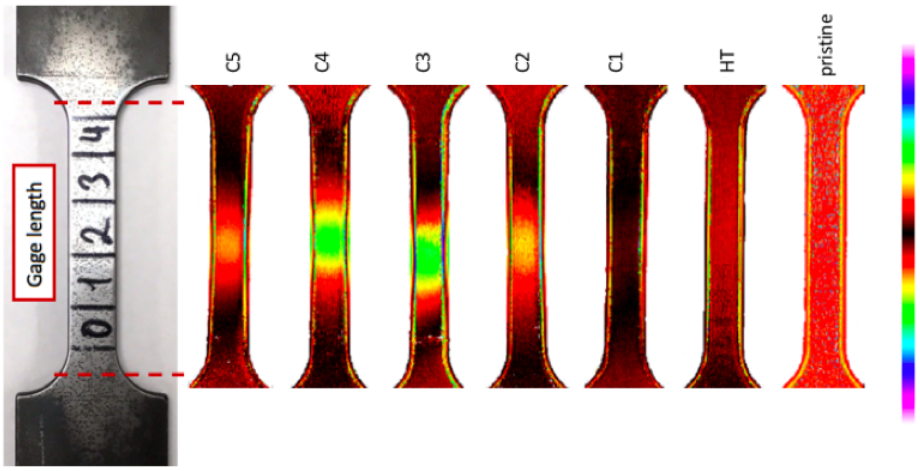

Figure 58. Color map of time of flight (TOF) change for all the creep samples, the sample after heat treatment, and the pristine sample.

The 3D images of the same specimens shown in Figure 59 demonstrate the variations in TOF along the gage length better. The 3D demonstration shows the duration of time that the wave travels between the bottom surface of the sample and the bottom of the acoustic microscope as shown in Figure 60. Thus, these images are depicting the bottom surface of the sample which is moving inward due to the localized damage during the creep. It should be noted that this localized damage or necking is not observable by visual inspection; however, the precise measurement of TOF in a matter of microseconds can resolve these differences.

Thus far, only the variation of TOF was considered. However, TOF measurement alone cannot be an indication of change in the microstructure after different levels of creep dam-

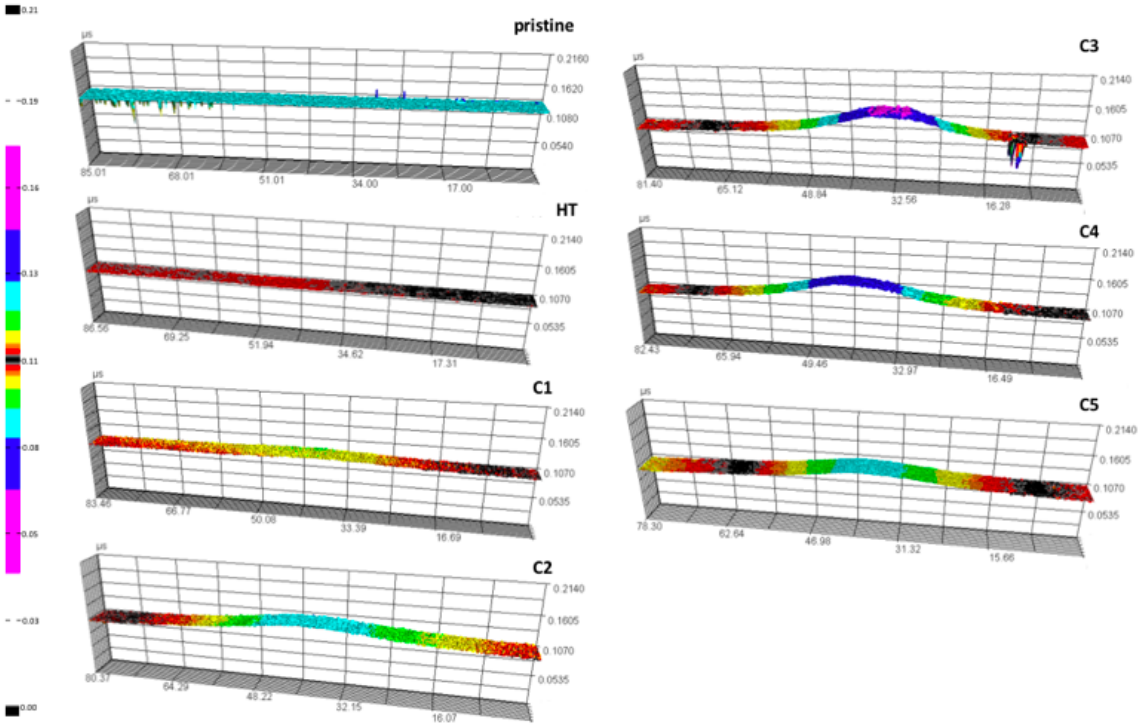

Figure 59. 3D Color map of time of flight change for all the creep samples, the sample after heat treatment, and the pristine sample.

age. Thus, it is important to distinguish between the effect of thickness and microstructural variations on TOF. For this purpose, the thickness along the gage length of the samples was measured at 5 mm increments to the precision of 0.0254 mm.

Having the TOF and thickness of the same points, the velocity was calculated for at least 10 points along the gage length to reveal the effect of the microstructure on the wave velocity. Figure 61a, b, and c show the change of thickness, TOF, and velocity, respectively. By compar-

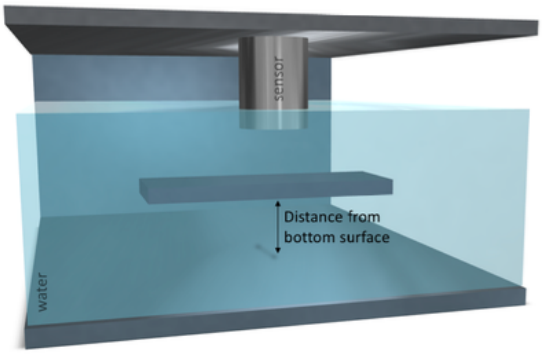

Figure 60. Schematic of the acoustic microscope showing the distance from the bottom surface of the sample to the bottom of the equipment.

ing the pristine with the HT sample, a small thickness variation is observed (Figure 61a), which can be attributed to the grinding of the surface of the HT sample with 400-grit sandpaper after heat treatment and before the ultrasonic measurements to remove the oxide layer formed on the surface and produce a consistent surface for all the samples.

Ignoring this small variation in specimen thicknesses and looking at the steel microstructure between the as-received and heat-treated condition (see Figure 62),the as-received specimen presents a microstructure with a ferritic matrix and small spherical carbides corresponding to 170 BHN hardness; on the other hand, the HT specimen shows a tempered lath martensitic structure with small carbides with 275 BHN hardness. Figure 61c and Figure 63 show a significant difference in velocity between these two microstructures which shows a large decrease

from 6100 m/s in the pristine (as-received) specimen to 5950 m/s in the HT sample, equal to 2.5% decrease.

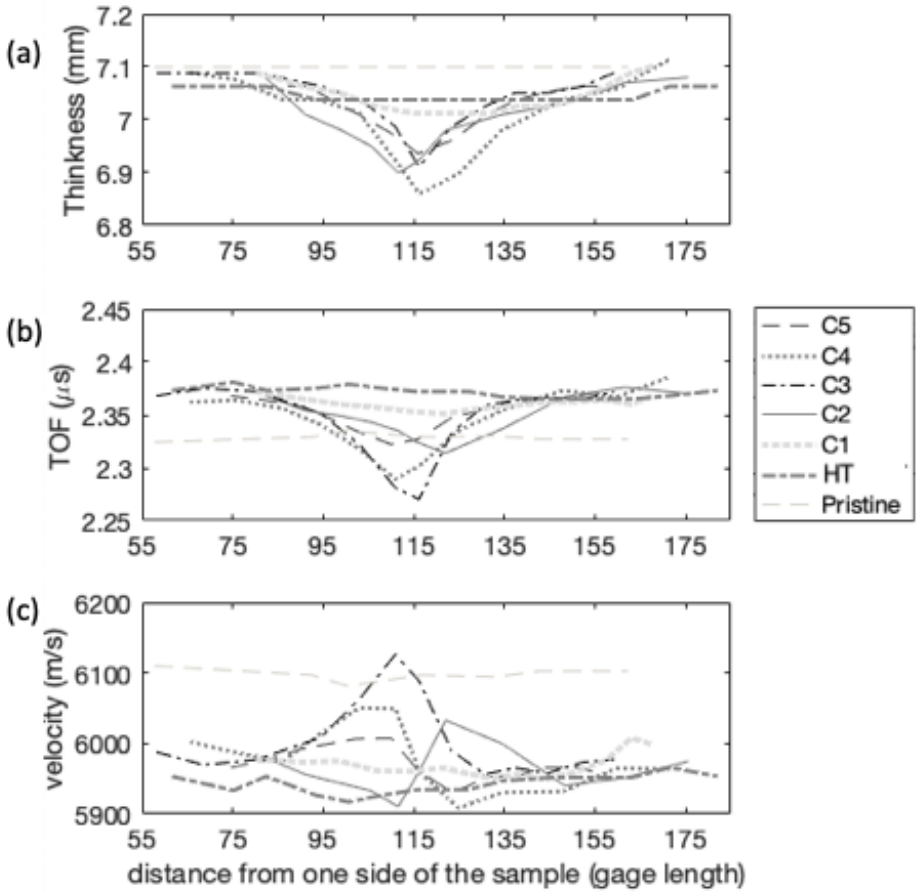

Figure 61. The change of (a) thickness, (b) TOF, and (c) velocity along the gage length for different creep samples, heat treated, and the pristine sample.

One of the important characteristics of the lath martensite is their tendency to align themselves parallel to each other in the parent austenite grains [13] along with the high density of dislocations. While the pristine sample was in annealed condition as reported by the manufacturer, showing no sign of martensitic microstructure. As explained in the previous chapter, martensite is a metastable phase supersaturated with carbon atoms, with high dislocation density and considerable lattice strain caused by the Base Centered Tetragonal (BCT) phase transformation. BCT corresponds to the strained BCC structure along the c-axis. This high degree of randomization and miss-orientation introduced in the matrix and the presence of dislocations lead to the decrease in wave velocity. This effect can be seen clearly in the Figure 61c between the Pristine and HT sample.

The change of velocity along the gage length for other crept samples is also shown in Figure 61. The maximum velocity along the gage length corresponding to the most damaged spot is depicted for each strain level in Figure 63. In this figure, a good correlation between the velocity and the strain level is established, which shows the increase of velocity with creep strain regardless of the duration of the creep test. The fact that the creep samples have higher velocity than the heat-treated sample is an indication of the stress relief and aging experienced by each sample during creep. The stress relief happens because of the tempering effect of creep at the high creep temperature for long periods of time.

The total increase from HT sample to C3 sample is 2.66% which makes the C3 sample velocity almost the same as the annealed pristine sample. It seems that by increasing the strain level, the increase in velocity is more pronounced e.g. the increase in creep strain from 2.01%

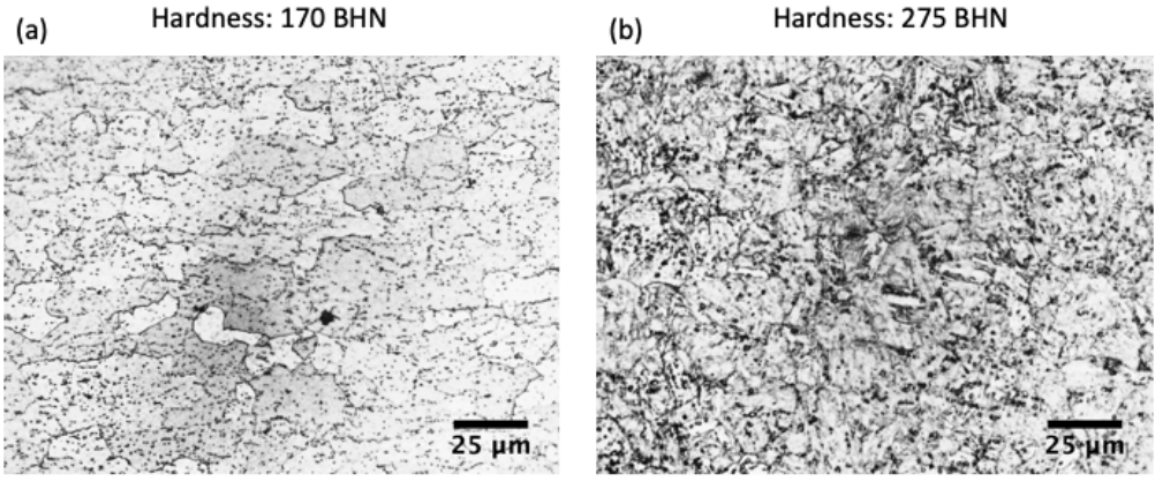

Figure 62. Microstructure of 410 Martensitic stainless in (a) as received condition, fully tempered, and (b) after 1-h HT at 980°C / AC / 2-h. tempered at 650°C/ AC.

to 3.04% produced a raise of 0.28% in velocity, yet for even smaller increase in creep strain, 3.04% to 3.59%, the velocity increased for 1.22%.

Recall that any strain in the lattice, increases dislocation density that decreases the wave velocity. But, the exposure of the steel to creep resulted in tempering of the sample leading to the annihilation of some dislocations while the lath martensite morphology remains. The higher the creep strain, the more annihilation of the dislocations takes place and coarsening of alloy carbides that softens the material relative to its initial condition after heat treatment.

This can be explained better by looking at the stage of the samples in the creep curve. In other words, the strain rate of the sample before stopping the creep test should be investigated

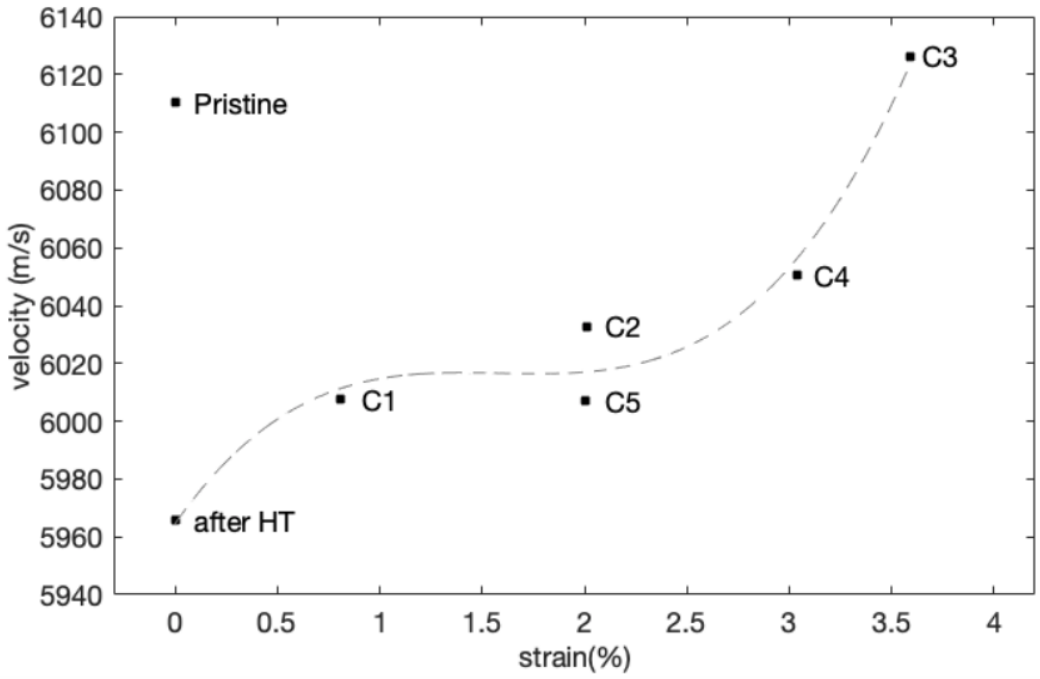

Figure 63. Change of velocity with strain for different creep samples.

to understand the reason for increasing the velocity. Figure 64 shows the change of wave velocity with the strain rate of the samples. Based on this figure, it is observed that the two samples of C1 and C5 which have not entered the tertiary stage are showing the minimum velocity, even though their creep duration is completely different. However, the other three samples are showing a significant increase in velocity as their strain rate is increasing rapidly upon entering the tertiary stage.

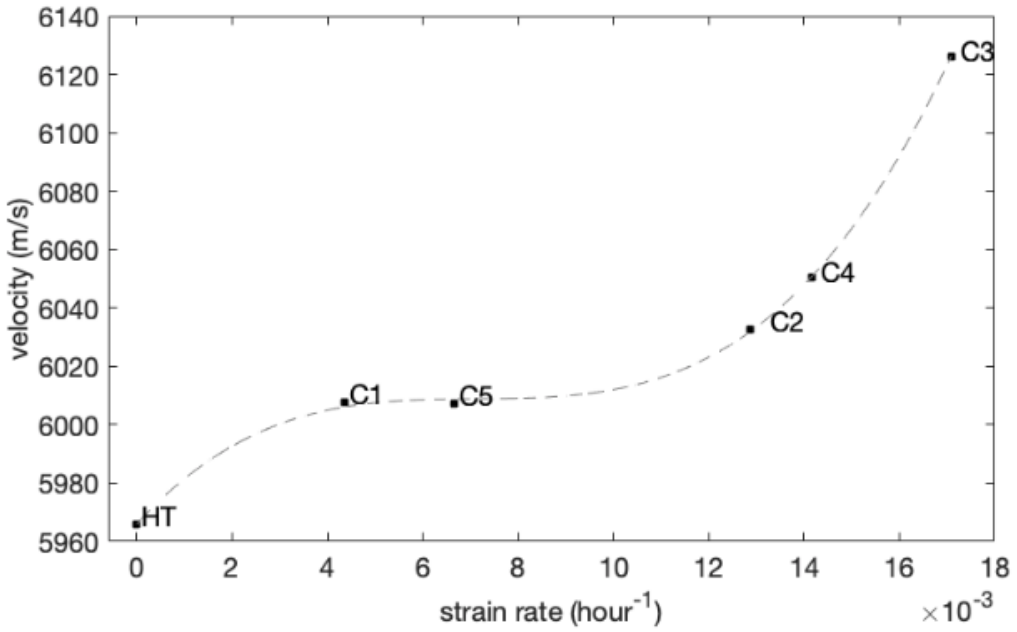

Figure 64. Change of velocity with strain rate for different creep samples.

As mentioned in section 1.4, the strain rate ($\dot{\varepsilon}$) depends on both recovery rate and work hardening (Equation 1.16). For the samples that are in the steady state stage, there is a balance of these two mechanisms (dislocation creation and annihilation), while the samples that have entered the tertiary stage have the recovery process as their predominant process. That is why these samples are showing a sudden increase in their wave velocity.

The similar wave velocity for C1 and C5 shows that regardless of the designed life span of a component, if the strain is increasing due to any unpredictable source, there is a chance to detect the damage with the immersion ultrasonic measurement, even if the sample is in the

beginning of the steady state. Nevertheless, the presence of a reference sample representing the initial condition is always required for analyzing the in-situ situation of the samples.

While the localized damage in the creep samples is apparent in the acoustic micro-graphs, the aged samples do not show any variation in time of flight throughout their full length as shown in Figure 65 and Figure 66.

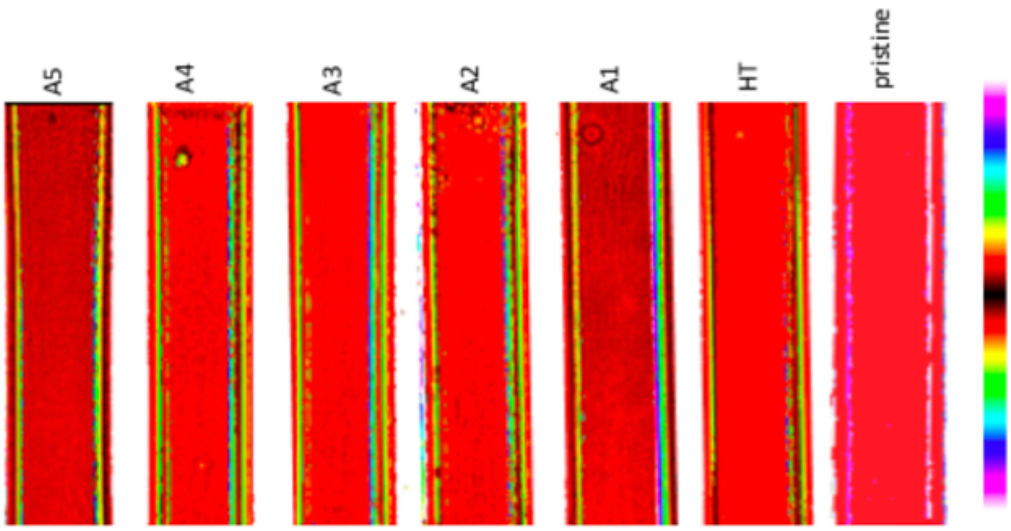

Figure 65. Color map of time of flight (TOF) change for all the aged samples, the sample after heat treatment, and the pristine sample.

The average velocity along the length of the aged samples is plotted in Figure 67, which shows a higher velocity for the pristine sample and almost a similar value with the rest of the

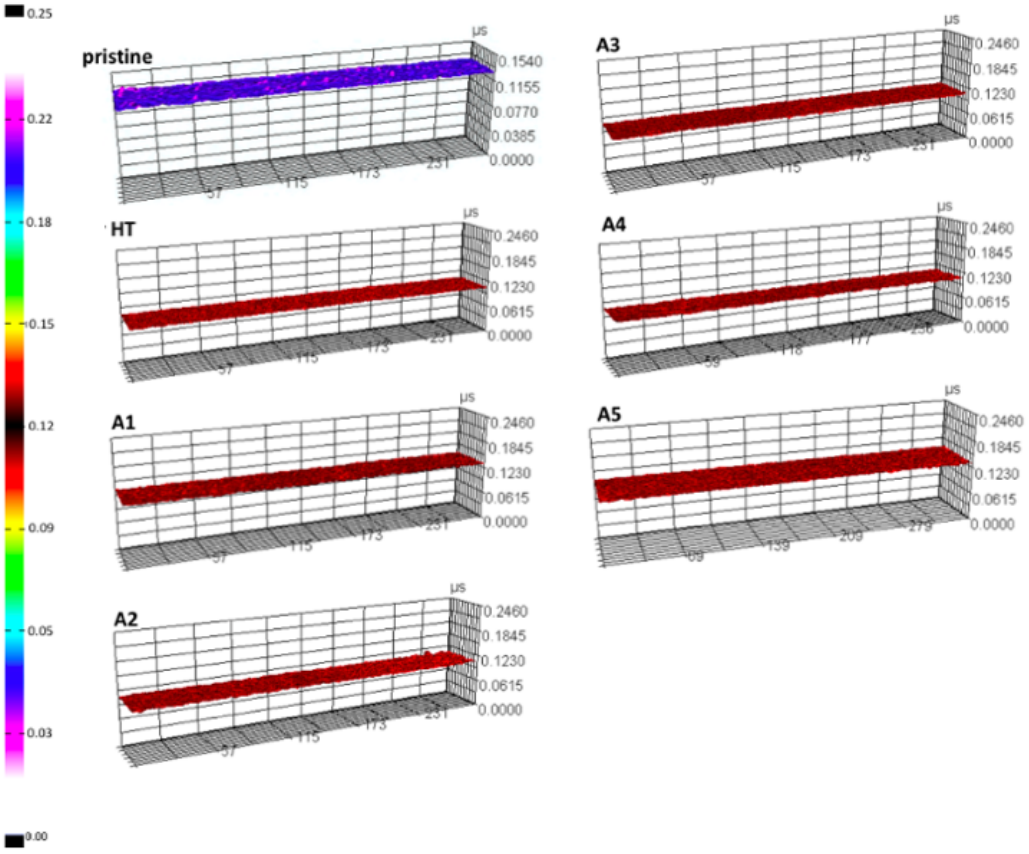

Figure 66. 3D Color map of time of flight change for all the creep samples, the sample after heat treatment, and the pristine sample.

aged samples. This shows that the change in the microstructure of the 410 SS with time at this temperature, is small enough to not to be detected with the velocity measurements using linear ultrasonics.

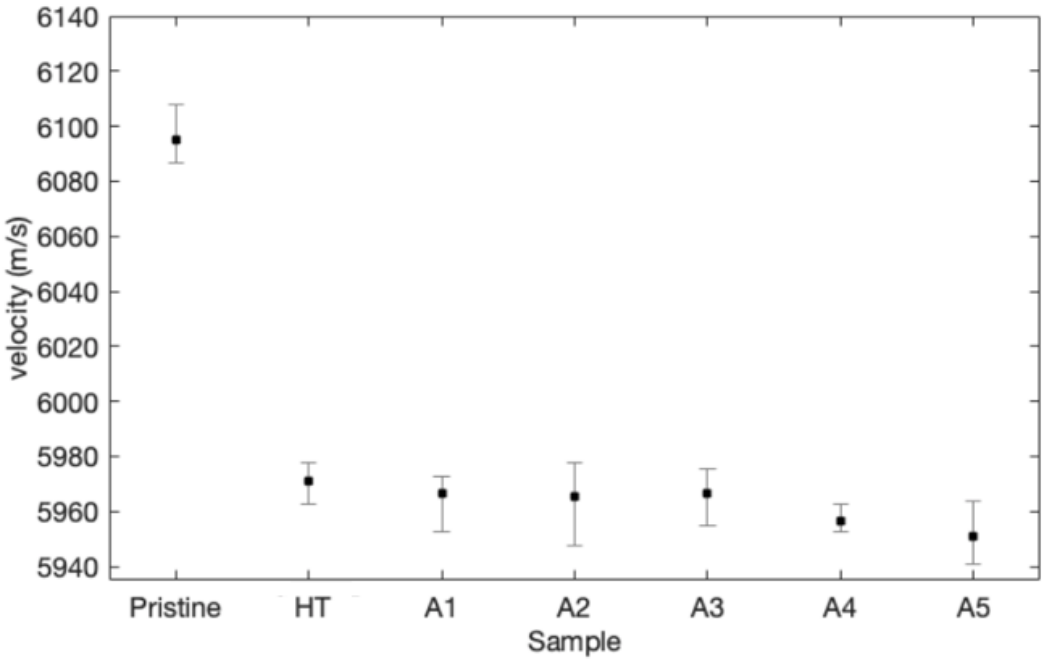

Figure 67. Change of velocity for the rectangle sample in pristine condition, after heat treatment, and different thermal age durations.

4.3.2.2 Ultrasonics Nonlinearity Parameter β

As mentioned before, the nonlinear effect will be generated in the ultrasonic wave upon its propagation through the material due to the nonlinear elastic properties of that material. This nonlinearity in the microstructure is detectable by measuring the nonlinearity of the ultrasonic wave compared to its non-damaged condition [22]. Harmonic generation, which is measured as the relative change of A_2 over ${A_1}^2$ (β parameter), was used in this research to assess the creep damage progress as the exposure time increases. All the non-linear UT tests were carried out

for five different points along the gage length to find the damage location at different stages of creep. These points are shown as No. 0 to 4 in Figure 58. Since there is a minute change in the thickness due to the localized damage in some samples (Figure 58), the thickness of the samples was included in calculating the β parameter.

The results of the nonlinearity parameter versus the location tested along the gage length is shown in Figure 68. The results of the points 0 and 4 are ignored in this figure due to the high error that may have been caused by the geometry closer to the shoulder of the dog bone sample.

Firstly, it is seen that for samples HT, C1, and C2, β is uniform along the gage length. This is acceptable for HT and C1 samples which experienced no or very small plastic deformation. However, the results from Figure 58 showed that there is a small localized damage in sample C2 and C5 at point 2 which raise the expectation to see some fluctuations in β at different points. It should also be considered that these fluctuations may not be apparent due to the larger scale of this plot. There is also an increase in β at point 3 of sample C5 which do not correspond to the localized damage location shown in Figure 58.

Ignoring point 2 (which seems to be the location of the localized damage for all samples) for the time being, β parameter tends to decrease for longer creep durations in other locations. This can be clearly seen at point 1 in Figure 68 which shows the HT sample to have the highest β and agrees to the martensitic state of the material after hardening and tempering for a short amount of time (2 hours). This sample also showed the lowest wave velocity as discussed in section 4.3.2. Exposure to the creep temperature for 290 hours (C1) then resulted

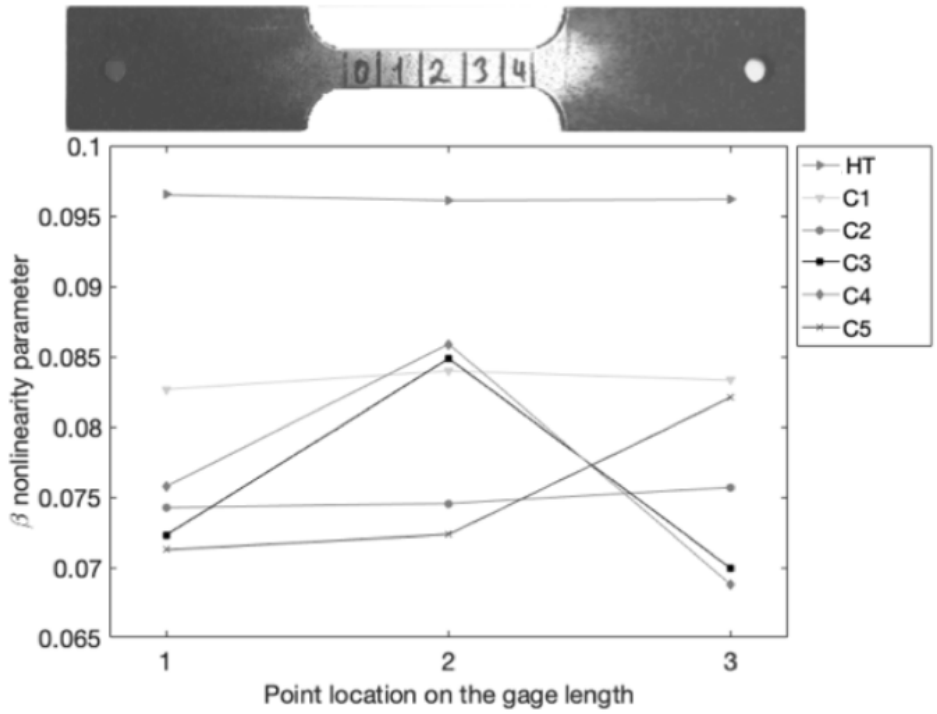

Figure 68. The change of nonlinearity parameter β for different creep samples at different locations along the gage length.

in a small decrease in β for point 1 due to the release of some strains (i.e., dislocations) in the hardened martensitic microstructure. Accordingly, the rest of the samples also showed smaller but comparable value of β.

Up to this point, only the general variation in the microstructure was evaluated after long exposure to high temperature. However, based on the Figure 58, it was shown that the creep damage became localized at point 2 starting with sample C2. This localized damage is also

observable for point 2 in Figure 68. In order to investigate the effect of this localized creep damage on nonlinearity parameter, β value for point 2 is plotted versus strain and strain rate in Figure 69 and Figure 70.

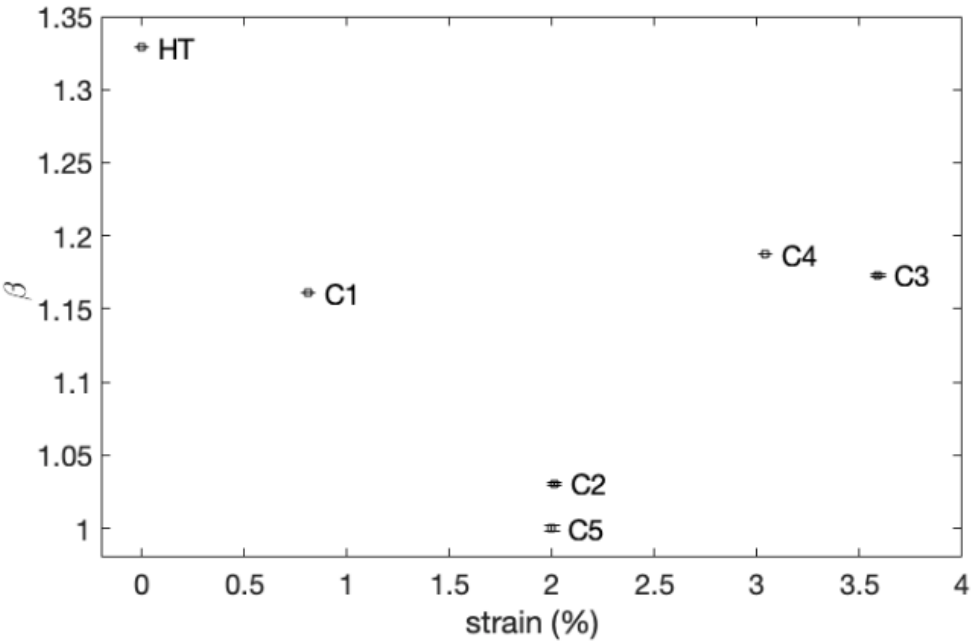

Figure 69. β nonlinearity parameter variation with creep strain for point 2.

Based on Figure 69, it is observed that β decreases from the initial value recorded for HT sample, to C1, and to C2 and C5 samples, making C2 and C5 the lowest recorded β values.

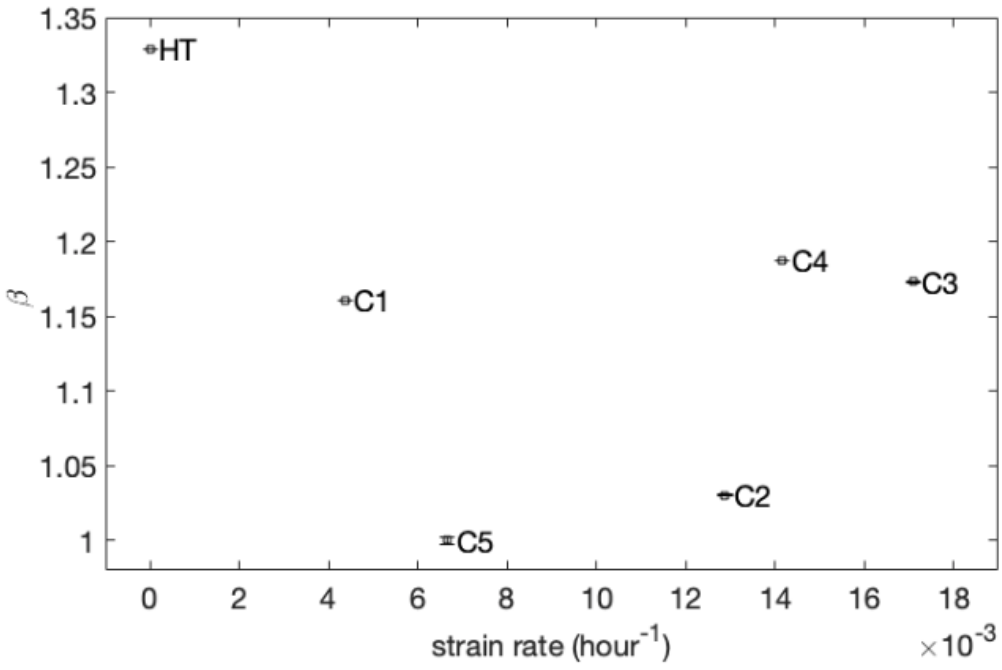

Figure 70. β nonlinearity parameter variation with creep strain rate for point 2.

However, it experiences an increase again for C3 and C4, yet lower than the value recoreded for the HT specimen.

In the previous section, the linear wave velocity appeared to increase continuously with increase in the strain level which was attributed to the softening of the matrix during the creep damage. Increase in β is a sign of increase in the nonlinearity in the material microstructure which contradicts the increase in the velocity. This contradiction however, can be the indication of the sensitivity of β to some microscopic damages which the wave velocity could not

detect. Several competing metallurgical reactions can happen during the creep damage including (1) strain hardening, (2) softening processes such as recovery, recrystallization, precipitate coarsening or overaging, and (3) cavity or void formation, their coalescence and eventually cracking [147, 152]. Figure 71 shows the evolution of some of these microscopic changes in the microstructure during the creep procedure. If the strain hardening is the dominant factor, the strain rate during the creep should decrease, whereas all the other factors increase the strain rate and the balance between them forms the shape of the creep curve of a certain material [147].

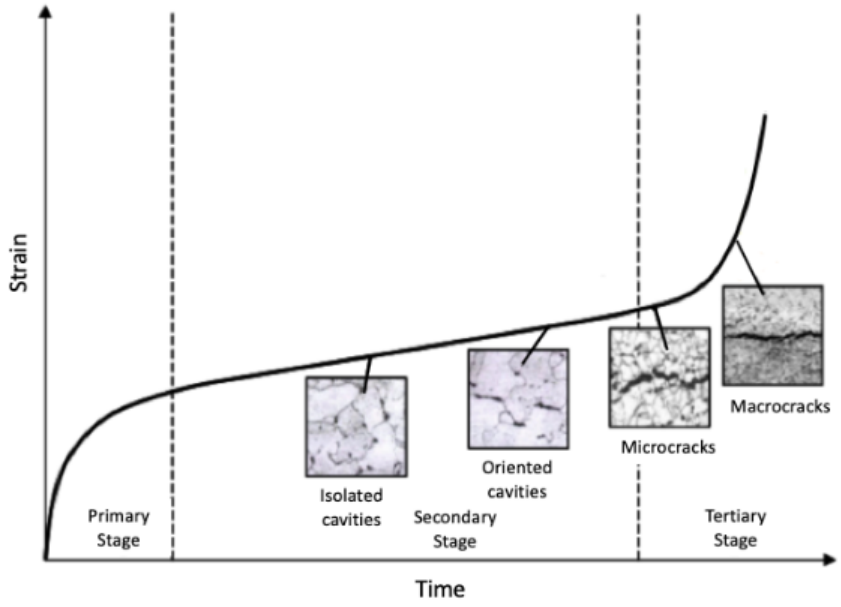

Figure 71. Typical creep curve with evolution of microstructural damage [24].

If it is assumed that the formation of microcracks happens at the beginning of the tertiary stage, the increase in β for samples C2, C3, and C4 can be justified considering the fact that they have entered the tertiary stage based on their creep curves. It can be stated that starting from a hardened and briefly tempered condition for HT sample, β parameter decreases with increasing the creep duration as long as the sample is in the steady stage region or has a low strain rate. At this stage the change in the microstructure includes the release of some stresses due to the tempering of the martensite matrix, and the balance between the recovery and work hardening due to creep process. There might be some micro-cavity formation happening at this stage, but this factor seems to be overcome by the tempering effect of martensite for 410 SS in this research. However, for the samples entering the tertiary stage and with higher strain rate, β starts to increase again. This is better shown in Figure 70 based on the strain rate of the samples.

From Figure 69 and Figure 70, the difference between C2 and C5 despite having the same strain can be establish by looking at their variation in strain rates. This is an important point in creep damage detection and life assessment of service components which indicates that the creep damage cannot only be assessed based on the strain level, but also on the strain **rate** of samples or components. There is always a high chance that some high stress concentration conditions may be present in the material, such as precipitation of a brittle phase during heat treatment in the manufacturing process or non-uniform stress distribution under the service. These points can be potential factors to change the creep behavior of the same material from C5

to C2 which need to be detected and addressed in a timely manner to prevent any catastrophic failure.

Another point that needs to be addressed is the smaller β value obtained for sample C3 compared to C4 when both the strain level and strain rate of C3 are higher than C4. This may seem to contradict what was mentioned before, however the color map image of time of flight (TOF) in Figure 58 can explain this small variance. As mentioned in the experimental setup of the nonlinear ultrasonic testing in 2.2.3.2, the diameter of the piezoelectric transducers used in this experiment is 0.95 cm and the testing area of each point from 0 to 4 on the creep sample is about 1×1.2 cm^2. Based on Figure 58, the maximum point corresponding to the localized damage in sample C3 seems to be on the border of point 1 and 2 which means that the very maximum point of the damage for this sample may have been missed in NLUT measurements. This is observed even better in the 3D image of the TOF in Figure 59. The possibility of missing a highly damaged point due to the size and testing location of the piezoelectric sensors highlights the application of the acoustic microscope along with the NLUT. In this case, the former technique can give information about the uniformity or localization of the damage and the latter reveals the minute sources of nonlinearity which is not detectable by LUT.

Figure 72 shows the effect of strain rate on wave velocity and β parameter for point 2 for all creep samples. In addition, the change in microhardness for the same point has been measured and plotted in this figure. The microhardness was measured five times on the cross section of gage length in the middle of point 2 for each sample. As seen in this figure, hardness decreases as the strain rate increases. This trend in hardness proves the fact that an overall softening is

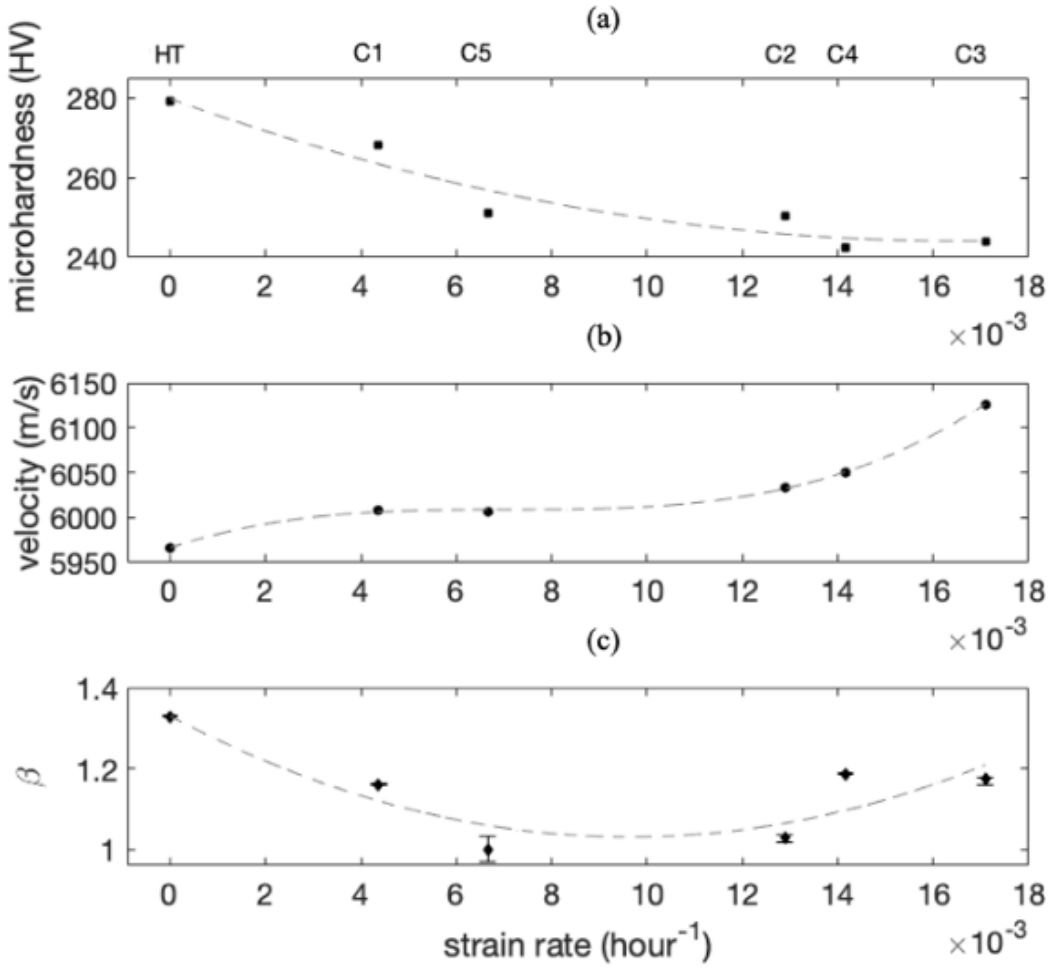

Figure 72. The effect of creep strain rate on (a) hardness, (b) linear wave velocity, and (c) β nonlinear parameter for point 2 along the gage length of 410 SS

happening in the microstructure which implies an increase in strain rate and also shows a very good correlation with the change in velocity. This was also confirmed using multiple macro-

hardness measurements on the surface of the samples. As mentioned before, this softening in the microstructure correlates with a decrease in β as long as the materials is in the secondary stage i.e. the tempering effect of the microstructure is the primary factor. Upon entering the tertiary stage, β does not follow the same trend as hardness and velocity anymore and it increases due to the void formation and coalescence, and/or carbide precipitation.

The same changes in the microstructure were also observed by Baby et al [22] for the titanium alloy and it was attributed to void nucleation and growth during the creep deformation. In their work, the maximum value of β was observed after about 0.6 creep fraction life followed by a drop after about 0.8 of creep life. It was stated that there may be an optimal scale of damage providing the highest nonlinear ultrasonic response and any further damage will cause a reduction in β. While this conclusion may be applicable in case of Titanium alloy in their research, it is not believed to be the reason for the reduction of β for the sample C5 in this research. One important note to be emphasized is that in this research, although the samples are interrupted at different strain levels, they did not follow the same master creep curve and therefore, they cannot be analyzed just based on their creep life fraction. In addition, one other important factor in this research is the initial condition of the samples before the creep deformation, which is the hardened and tempered for 2 hours whereas most of the materials used in the previous researches started in annealed condition. Polar et al. [147] also observed the same damage process during the creep damage detection of 410 SS by magnetoelastic method. They found out the presence of voids in the tertiary stage decreases the magnetic flux.

The change in β behavior before and after entering the tertiary stage is a powerful tool to understand the material creep stage and it also shows the NLUT potential to detect the transition from the steady stage to the more dangerous tertiary stage. This capability satisfies the main goal of this research to find a technique that can detect the transition to tertiary stage of the creep while the material has a complicated initial condition i.e. hardened vs. annealed and provides enough time for replacement of the damaged component to prevent any catastrophic failure.

Similarly, the variation of hardness, linear velocity, and average measured β for two points along the length of the aged samples are presented in Figure 73. In this figure, it is seen that the hardness, both macro and micro, decreases as aging time increases. This decrease of hardness is due to the tempering or aging of martensitic microstructure at the high temperature (620°C). However, as mentioned in section 4.3.2.1, the change in the velocity is not significant enough to account for the changes in the microstructure, since these changes are within the range of error bars. Despite that, a small decrease in velocity can be observed for samples A4 and A5.

It was mentioned before that the velocity increases for the creep samples that have an increase in strain rate or strain level due to the softening of the microstructure during the creep damage. It can be concluded that although there is a decrease in dislocation density due to tempering in the aged samples, the softening of the microstructure is not comparable to the one experienced by the creep specimens and thus, it could not be detected by the linear velocity.

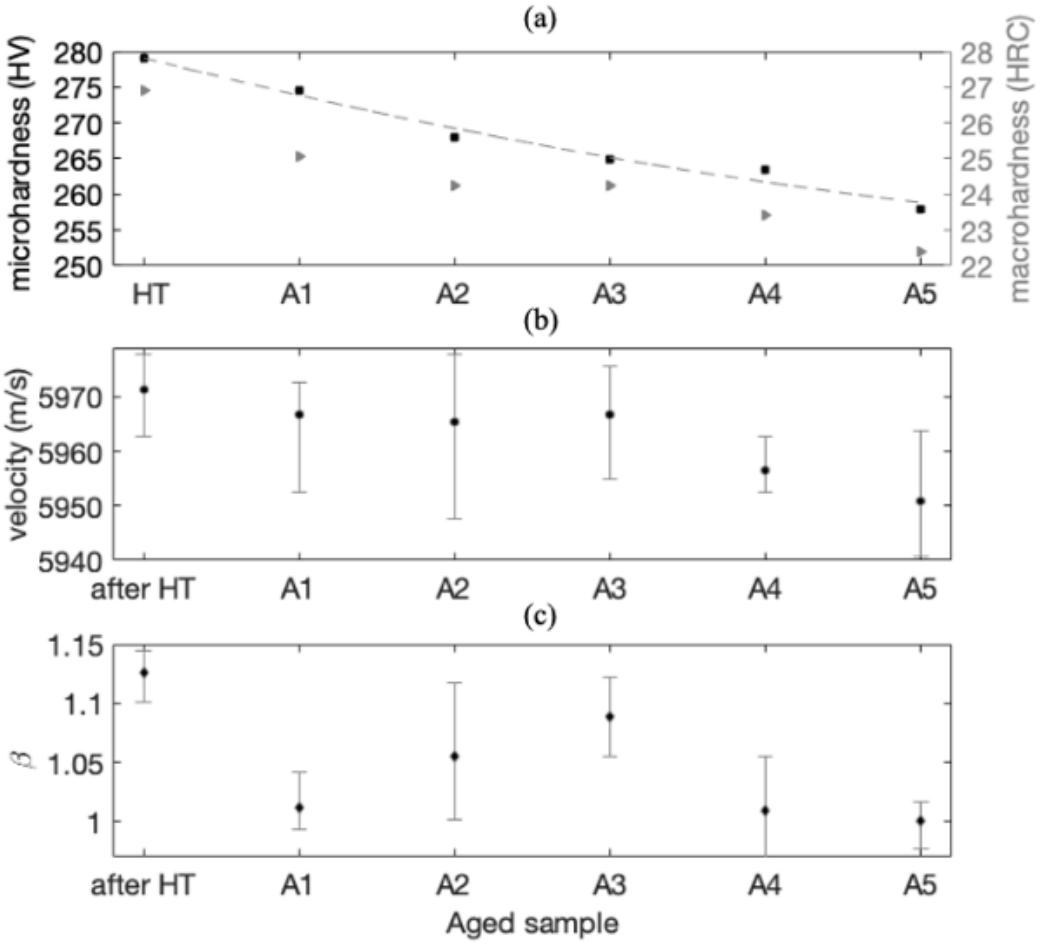

Figure 73. The effect of ageing time on (a) hardness, (b) linear wave velocity, and (c) β nonlinear parameter for average of two points along the gage length of 410 SS

Almost the same situation could be applied to β since the change in the nonlinearity parameter is not remarkable for different ageing times. However, the HT sample shows the highest β

which can be due to its martensitic microstructure, with high dislocation density compared to the other aged samples where dislocations are being annihilated due to tempering. The other trend seen in Figure 73, where β increases for samples A2 and A3 and decreases for sample A4 and A5, could be related to the precipitation of carbides, which is also connected with the tempering of martensite in alloy steels. The initial decrease in β observed in sample A1 could be related to the significant decrease in dislocation density, which is known to be the initial stage of tempering. The subsequent increases in samples A2 and A3 can be associated with the precipitation of alloy carbides, where A3 represents the optimum size and volume fraction of carbides. The decrease observed in samples A4 and A5 can be correlated to the next stage of tempering which is the coarsening of the carbides. Considering Figure 73b, the slight decrease in linear velocity can also be an indication of large enough carbides to be detected by linear velocity.

It should be noted that although the change in β was attributed to the presence of carbides, an increase in the microhardness was not observed for these samples while the macro-hardness of the sample A3 which covers a much larger area of the sample under the indentation showed a minute increase for this sample.

The larger error bars shown in Figure 73 compared to Figure 72 is due to the fact that the results generated in Figure 72 are obtained only from one point in the middle of the creep sample which was believed to be the point of localized damage. Whereas in the case of aged samples, the results are representing the average value of the whole sample length (76 mm) for linear wave velocity measurement, and the average of two points for the β measurement.

Therefore, there are more scattering in the data both due to testing at different locations and possible associated experimental errors such as surface condition, applying the couplant, and attaching the sensors.

4.3.3 Microstructural Characterization

All the creep samples were sectioned from the middle of the point 2 as shown in Figure 74 for further metallographic analysis. Figure 75 shows the optical micrographs of the samples after different duration of creep damage.

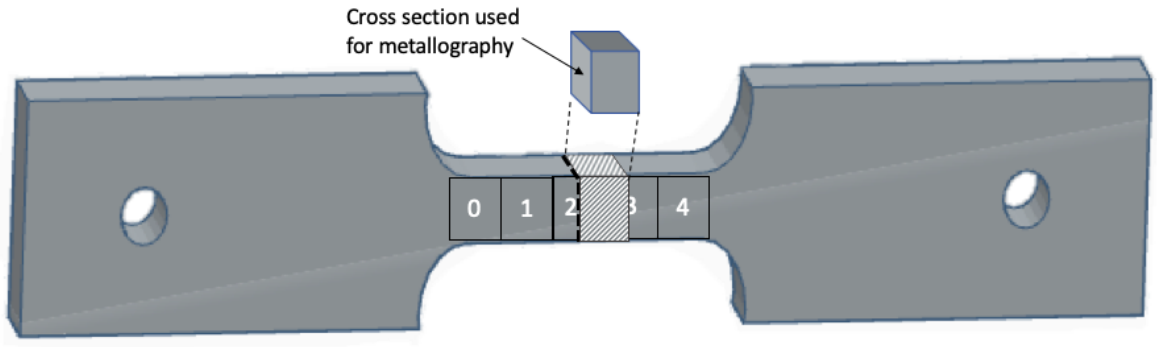

Figure 74. The metallography location along the gage length of the creep samples.

The microstructures of samples C1 and C5 show similar degrees of tempering which corresponds to their similar higher hardness and lower velocities shown in Figure 72, and both are experiencing secondary creep. However, due to higher recovery and initial recrystallization in

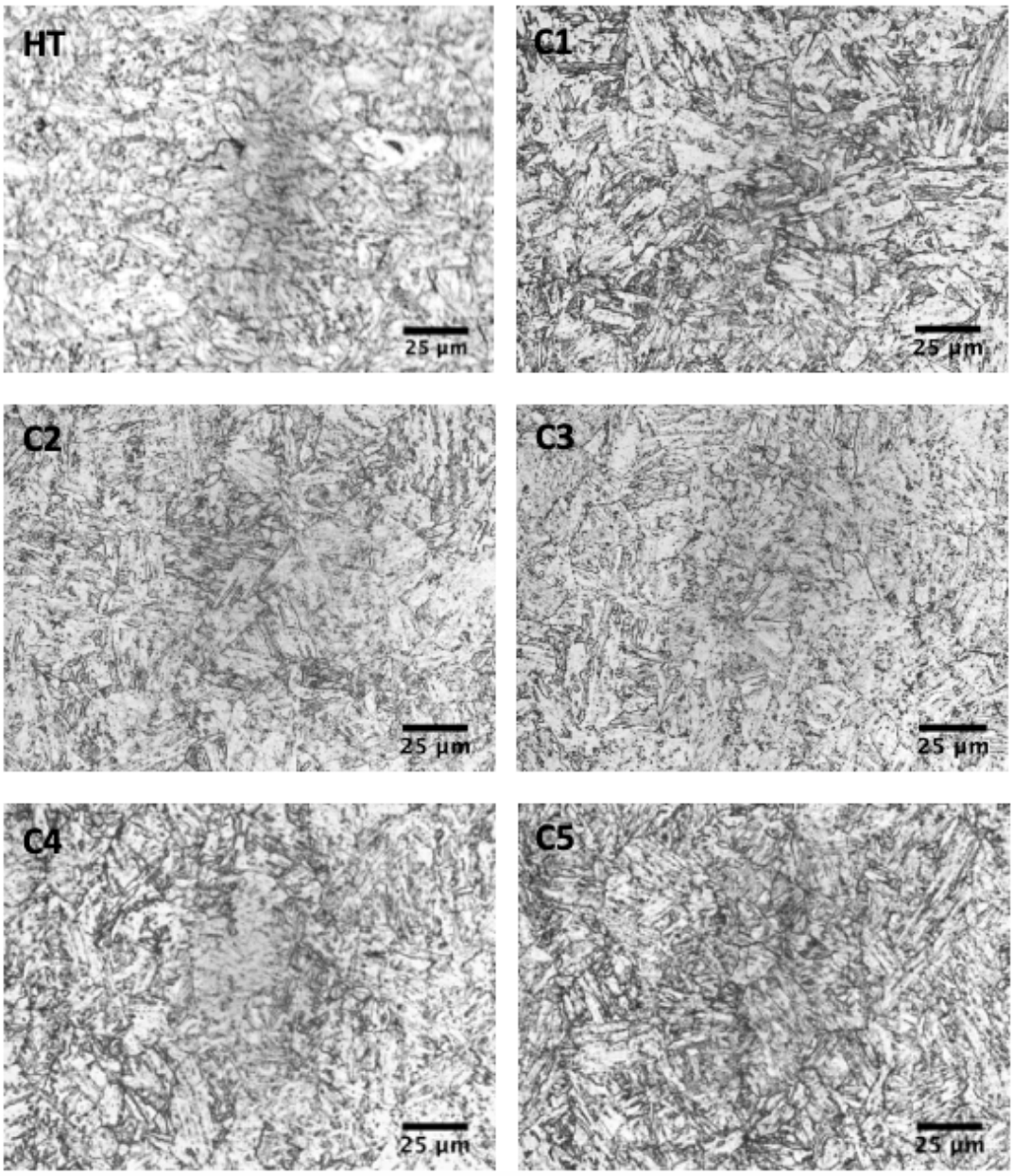

Figure 75. Optical micrographs of the HT, C1, C2, C3, C4, C5 samples at 500X magnification.

the matrix of C3 and C4, their microstructures appear to have some equiaxed grains and some degree of carbide precipitation are observed. This is in good correlation with the results presented in Figure 72a and b. It is also important to point out that the presence of voids or carbides in sample C2, C4, and C3 could overshadow the effect of matrix softening which led to the increases the β.

In addition, the micrographs of the aged samples are presented in Figure 76 These micrographs show a more tempered martensitic microstructure compare to the creep samples, and the decrease in the lath martensite structure is clearly seen for samples A4 and A5 which corresponds to the decrease of hardness for these samples. In the tempered martensite microstructure, a redistribution of carbon and carbide former elements such as Cr happens in the matrix. In addition, the transformation of matrix to the ferrite phase which is an equilibrium phase happens after exposure to high temperature. Ferrite is a solid solution of C atoms in Fe which transforms the crystal structure of the matrix from BCT to body centered cubic (BCC) i.e. a more relaxed state. The presence or change in carbide population was not easily detectable with optical microscopy for these samples.

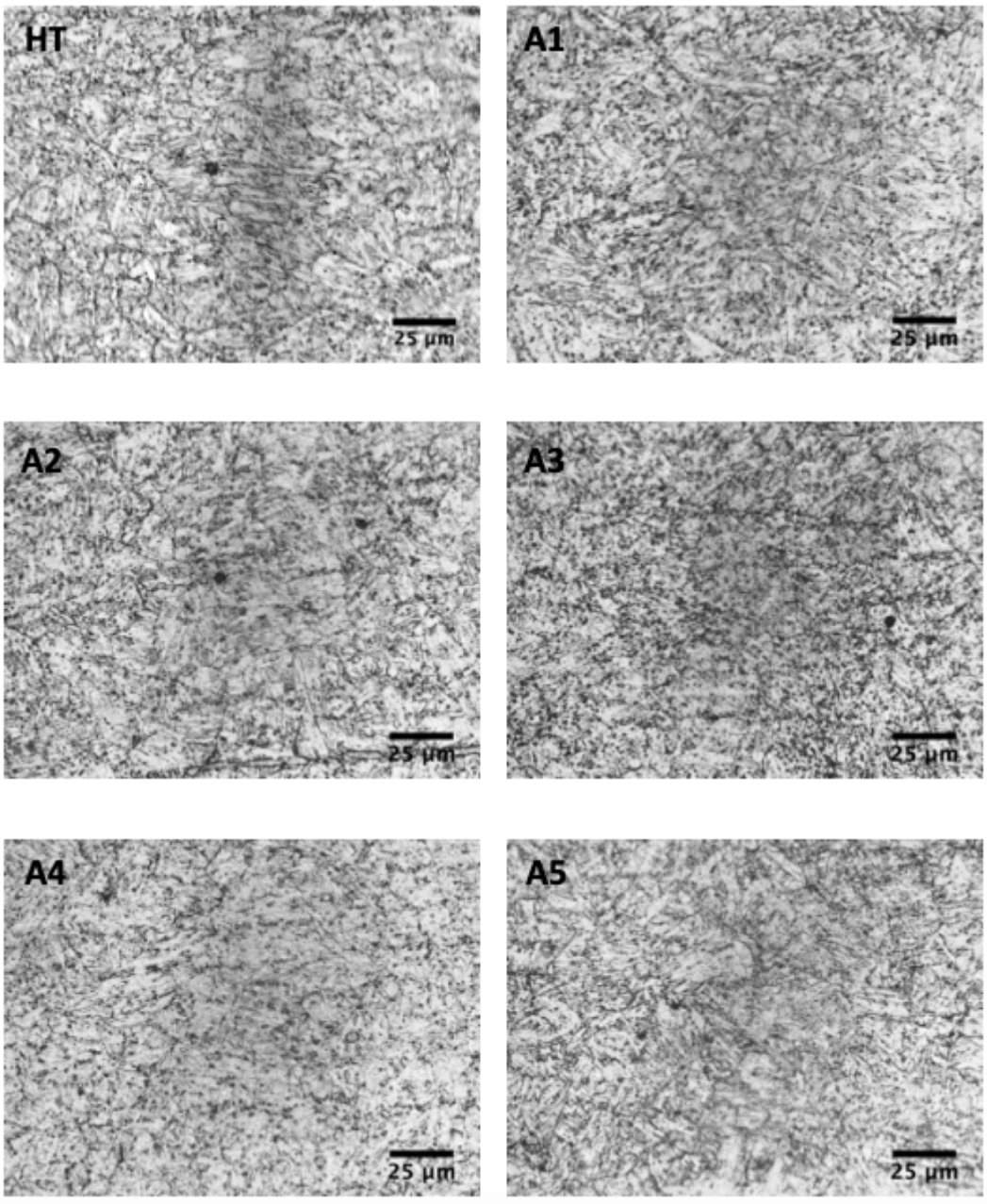

Figure 76. Optical micrographs of the HT, A1, A2, A3, A4, A5 samples at 500X magnification.

CHAPTER 5

SUMMARY, CONCLUSIONS AND SCOPE OF FUTURE WORK

5.1 Summary

The effect of three different damages on the linear and nonlinear ultrasonic wave properties was investigated. Damages were introduced in the materials by (i) mechanical plastic deformation, (ii) intercritical heat treatment, and (iii) creep damage as a combination of thermal and mechanical damage over time. The goal was to understand the capability of linear and nonlinear ultrasonics to detect these damages in three different materials of Al1100, A572 steel, and AISI 410 stainless steel, respectively. In addition, the sensitivity of the linear and nonlinear ultrasonics was assessed for each damage type to find the best method or a combination, to detect the damage as early as possible in order to prevent unpredictable damages in the structures.

In chapter 2, plastically deformed samples to different strain levels were assessed by the immersion test using Scanning Acoustic Microscope (SAM) to measure the change in the wave velocity. Further on, the same samples were tested in through transmission mode to identify the second harmonics generated in waveform due the change in strain level i.e. dislocation density in the material microstructure. The NDE results were then verified by XRD measurements of the residual strains in the crystals produced by the plastic deformation. Furthermore, the effect of geometry was assessed for two sections of the dog-bone sample in the middle of the gage

length and the shoulder area. It was believed that in these two sections, the ultrasonic response should reveal different results due to the presence of the nonuniform plastic deformation in the shoulder area.

The results of the experiments on plastic deformation of Al1100 showed the wave velocity variation of only 0.12% for 2% change in plastic deformation. While the β nonlinearity parameter increased 19% for the same 2% change, or the overall of 40% for 4% strain in Al1100. This confirms the very less sensitivity of the wave velocity to assess the small changes in the microstructure which can also be attributed to measurement and instrumental errors. However, the SAM has the capability to show the smallest changes in the thickness due to the localized damage. This can be a helpful to determine the most susceptible spots for testing and to make sure about the uniformity of the damage.

Measurement of β in the shoulder area compared to the middle of the gage length confirmed the presence of nonuniform plastic deformation in this section. The nonuniform plastic deformation contributes to higher nonlinearity in the microstructure and thus, manifest as higher β value. The change in β for the shoulder area was shown to be 2.7 times larger than the middle of the gage length. These results emphasize on the fact that care should be given to the position of the testing spot and the geometry of the component since more complex geometry can produces stress concentration points in the components. Therefore, it is important to have a reference for the initial (pristine) condition of the component which resembles the same geometry and stress concentrations as the component under the test.

Chapter 3 described how the changes in the ferrite and martensite phase volume fraction in A572 steel affect the linear and nonlinear properties of the wave, this time using wave velocity and acoustoelastic coefficient (AEC) measurements, respectively. The measurement of the wave velocity was the same as in chapter 2, whereas the acoustoelastic coefficient was measured by monitoring the change in the wave velocity under stress.

Two phases with different volume fractions were generated using intercritical heat treatment according to the Fe-C phase diagram. The differences in the physical and mechanical properties of the ferrite and martensite phases were expected to be the source of the change in the wave velocity and acoustoelastic coefficients. In addition, the macro and micro-hardness of the material and its phases were measured for all the samples after the intercritical heat treatment to verify the changes in UT properties.

In the case of the heat-treated samples, the thickness of the sample was constant and similar for all the samples. Therefore, any change in the velocity was attributed to the changes in the microstructure. It was observed that the arrival time of the wave was increasing as the amount of martensite increased in the microstructure, which is equivalent to decrease in the wave velocity. This also showed a good correlation with increase in the hardness. The reason behind was explained as the influence of dislocation density, high degree of randomization, lattice distortion produced by the martensitic microstructure. Acoustoelastic coefficient however, showed much higher sensitivity to the change in the martensite volume fraction. For 73% increase in ferrite amount, AEC decreased 56% compared to the 0.47% change in the linear wave velocity. This

higher sensitivity stems from the dependency of AEC on third order elasticity constant of the materials in addition to the second order elasticity constants.

Chapter 4 investigated the effect of creep damage at 150 MPa and 620°C for AISI 410 stainless steel by both linear and nonlinear ultrasonic testing with the same test setup as chapter 2. Five different levels of creep damage were generated in the samples based on the creep strain. Another set of samples were also inserted inside the furnace to experience the same thermal condition as the creep samples, but without the presence of stress (aged samples) to distinguish between the effect of thermal damage via changes in microstructure, and the addition of the stress. The LUT and NLUT results were assessed both based on the creep strain, and the variation in the strain rate to monitor the creep stage. An important element in this research was the initial hardened and tempered (for 2 hours) condition of the creep samples.

The results indicated a continuous increase of 2.61% in the wave velocity when creep strain increases 3.59%. This change was attributed to the softening of the microstructure for the samples that enter the tertiary stage of creep. The same as aluminum samples in chapter 2, the SAM colormaps of TOF could reveal the location of the localized damage, although the overall change in velocity is not large.

However, β nonlinearity parameter showed another trend with increase in strain or strain rate. It was observed that β decreases for the samples in the steady-state stage due to the effect of high temperature and tempering of the martensitic microstructure due to the balance between work hardening and softening in this stage. While for the samples which entered the

tertiary stage, β increased again with increase in strain rate which is attributed to the void formation and carbide precipitation in these samples. Therefore, the void/carbide formation was found to be undetectable by linear wave velocity at the very beginning of the tertiary stage.

For the aged samples, the increase in the ageing time resulted in decrease in the hardness, an almost constant value for velocity with some fluctuations, and a peak in β after 437 hours of aging. The presence of carbides and their growth are the primary reasons behind these changes for the aged samples.

In this research, it was shown that the sensitivity of the nonlinear ultrasonics, by both higher harmonics and acoustoelastic coefficient measurement, is much higher than the linear velocity method. However, by using SAM, it was possible to detect the localized damage and have a more accurate target for nonlinear evaluation.

It was also shown that β is sensitive to the change in the dislocation density and lattice distortion due to either plastic deformation or the presence of martensite phase. The creep damage detection by β was shown to be more complicated and is affected by various factors such as tempering of martensite matrix, softening mechanisms, carbide precipitation and growth, and void formation. A combination of linear immersion technique to detect the localized damage in addition to the nonlinear measurement was found to be the best method to detect the damage in components.

5.2 Conclusions

- The sensitivity of the nonlinear ultrasonic testing is much higher than the linear velocity measurement in all three forms of damage investigated in this research, showing up to

150 times more change than the linear velocity for the material tested. However, the utilization of scanning acoustic microscope found to be helpful along with the nonlinear testing in determination of the localized damage for further testing.

- The overall of 40% change in β for 4% plastic strain in the Al1100, 56% increase in AEC with 73% increase in martensite phase in A572 steel, and a 32% change in β for 3.6% creep strain in 410 stainless steel was observed.
- The geometry of the test spot was found to have a great impact on the β nonlinearity parameter where resulted in 2.7 times higher β value for the shoulder of the dog bone in Al-1100 samples compared to the middle of the gage section.
- It was shown that the initial condition of the material, especially for the martensitic steels, can have a large impact on the β behavior, and the initial annealed vs. hardened condition should be distinguish with appropriate references for further testing in the component to assess the remaining life.

5.3 Future Work

The future work can be focused on calculating the exact amount of change in the dislocation density by Transmission Electron Microscopy (TEM) for the plastically deformed and creep samples. Scanning Electron Microscopy (SEM) is also required to further assess the carbide and void formation in 410 SS after different creep levels.

In addition, one of the final researches using the Scanning Acoustic Microscope was the Quantitative B-Scan Analysis Mode (Q-BAM) scan of the thickness of the creep samples. The

purpose was to find voids or carbides, if detectable by linear wave velocity, throughout the thickness. Figure 77 shows one example of the Q-BAM scan for C2 creep sample. It was found that some particles/voids are detectable through the surface scan, which will be revealed in the thickness scan over the cross section (yellow line). This can be a great tool to understand the 3D location of voids or particles. However, the attempts to cut the sample at the exact location and do metallography was not enough to find the nature of the spot. Some techniques such as X-ray radiography can have the potential to reveal the presence of these spots. If proved, ultrasonic test would be a much easier technique to detect the presence of particles compared to X-ray.

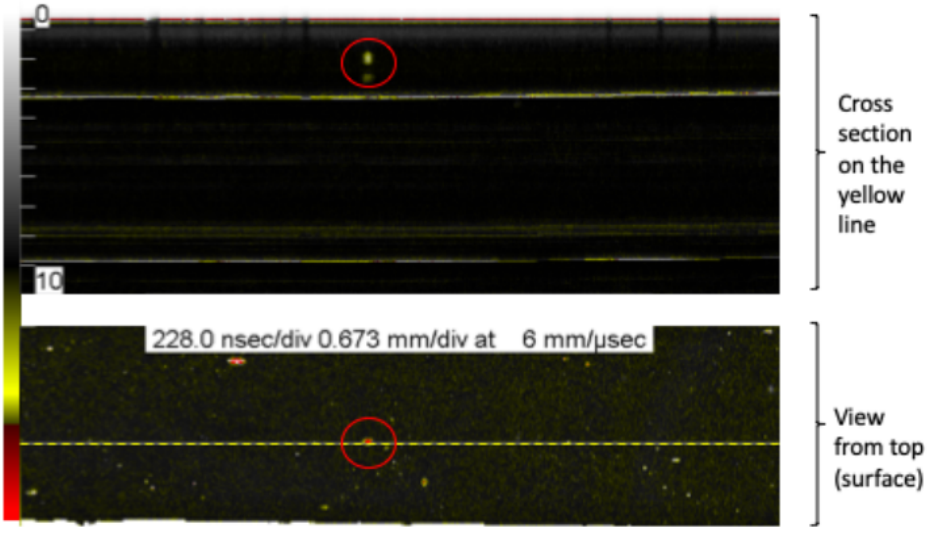

Figure 77. Q-BAM scan of the C2 creep sample.

5.4 Acknowledgment

This research is based upon work supported by the National Science Foundation (NSF) under award number CMMI 1463501 entitled Assessing Microstructural Damage Using Nonlinear Ultrasonics and Multiscale Numerical Modeling.

APPENDICES

.1 Journal of Measurement Copyright policy

For subscription articles: Authors transfer copyright to the publisher as part of a journal publishing agreement, but have the right to:

- share their article for Personal Use, Internal Institutional Use and Scholarly Sharing purposes, with a DOI link to the version of record on ScienceDirect (and with the Creative Commons CC-BY-NC- ND license for author manuscript versions)
- retain patent, trademark and other intellectual property rights (including research data).
- proper attribution and credit for the published work.

.2 Journal of Nondestructive Evaluation Copyright policy

Clear guidelines on submission of the work:

- that the work has not been published before (except in the form of an abstract or as part of a published lecture, review or thesis)
- that the work is not under consideration elsewhere
- that copyright has not been breached in seeking its publication
- that the publication has been approved by all co-authors and responsible authorities at the institute or organization where the work has been carried out

CITED LITERATURE

1. Kamali, N., Tehrani, N., Mostavi, A., Didem, S.-w. C., and Ernesto, O. J.: Influence of Mesoscale and Macroscale Heterogeneities in Metals on Higher Harmonics Under Plastic Deformation. Journal of Nondestructive Evaluation, 38(2):1–13, 2019.

2. Mostavi, A., Kamali, N., Tehrani, N., Chi, S.-W., Ozevin, D., and Indacochea, J. E.: Wavelet Based Harmonics Decomposition of Ultrasonic Signal in Assessment of Plastic Strain in Aluminum. Measurement, 2017.

3. Chassignole, B., El Guerjouma, R., Ploix, M. A., and Fouquet, T.: Ultrasonic and structural characterization of anisotropic austenitic stainless steel welds: Towards a higher reliability in ultrasonic non-destructive testing. NDT and E International, 43(4):273–282, 2010.

4. Hirsekorn, S., Van andel, P., and Netzelmann, U.: Ultrasonic Methods To Detect and Evaluate Damage in Steel. Nondestructive Testing and Evaluation, 15(6):373–393, dec 1998.

5. Ebrahimkhanlou, A., Dubuc, B., and Salamone, S.: Damage localization in metallic plate structures using edge-reflected lamb waves. Smart Materials and Structures, 25(85035.):0–44, 2016.

6. Herrmann, J., Kim, J. Y., Jacobs, L. J., Qu, J., Littles, J. W., and Savage, M. F.: Assessment of material damage in a nickel-base superalloy using nonlinear Rayleigh surface waves. Journal of Applied Physics, 99(12), 2006.

7. Valluri, J. S., Balasubramaniam, K., and Prakash, R. V.: Creep damage characterization using non-linear ultrasonic techniques. Acta Materialia, 58(6):2079–2090, 2010.

8. Ohtani, T., Ogi, H., and Hirao, M.: Acoustic damping characterization and microstructure evolution in nickel-based superalloy during creep. International Journal of Solids and Structures, 42(9-10):2911–2928, 2005.

9. Kussmaul, K., Blind, D., and Jansky, J.: Formation and growth of cracking in feed water pipeds and RPV nozzles. Nuclear Engineering and Design, 81:105–119, 1984.

10. Iida, K.: A review of fatigue failures in LWR plants in Japan. Nuclear Engineering and Design, 138(3):297–312, 1992.

11. Ruiz, A., Ortiz, N., Medina, A., Kim, J. Y., and Jacobs, L. J.: Application of ultrasonic methods for early detection of thermal damage in 2205 duplex stainless steel. NDT and E International, 54:19–26, mar 2013.

12. Raj, B., Choudhary, B. K., and Singh Raman, R. K.: Mechanical properties and non-destructive evaluation of chromium - Molybdenum ferritic steels for steam generator application. International Journal of Pressure Vessels and Piping, 81(6):521–534, 2004.

13. Polar, A., Indacochea, J. E., and Wang, M. L.: Sensing Creep Evolution in 410 Stainless Steel by Magnetic Measurements. Journal of Engineering Materials and Technology, 132(4):041004, 2010.

14. Ezechidelu, J. C., Enibe, S. O., Obikwelu, D. O., Nnamchi, P. S., and Obayi, C. S.: Effect of Heat Treatment on the Microstructure and Mechanical Properties of a Welded AISI 410 Martensitic Stainless Steel. Iarjset, 3(4):6–12, 2016.

15. Palit Sagar, S., Das, S., Parida, N., and Bhattacharya, D. K.: Non-linear ultrasonic technique to assess fatigue damage in structural steel. Scripta Materialia, 55(2):199–202, jul 2006.

16. Nagy, P. B.: Fatigue damage assessment by nonlinear ultrasonic materials characterization. Ultrasonics, 36(1-5):375–381, 1998.

17. Kumar, A., Torbet, C. J., Jones, J. W., and Pollock, T. M.: Nonlinear ultrasonics for in situ damage detection during high frequency fatigue. Journal of Applied Physics, 106(2), 2009.

18. Kumar, A., Mathuriya, S., and Shilpi, S.: Detection of Creep Damage and Fatigue Failure in Thermal Power Plants and Pipelines by Non-Destructive Testing Techniques. A Review. International Journal of Engineering Research & Technology (IJERT), 3(11):1147–1152, 2014.

19. Ohtani, T., Ogi, H., and Hirao, M.: Electromagnetic acoustic resonance to assess creep damage in Cr-Mo-V steel. Japanese Journal of Applied Physics, Part 1: Regular Papers and Short Notes and Review Papers, 45(5 B):4526–4533, 2006.

20. Raj, B., Vaidhianathasamy, M., T.Jayakumar, and Bhanu sankara rao, K.: Assessment of microstructures and mechanical behaviour of metallic materials through non-destructive characterisation. International Materials Reviews, 48:273, 2003.

21. Ohtani, T., Ogi, H., and Hirao, M.: . Japanese Journal of Applied Physics, 48, 2009.

22. Baby, S., Nagaraja Kowmudi, B., Omprakash, C. M., Satyanarayana, D. V. V., Balasubramaniam, K., and Kumar, V.: Creep damage assessment in titanium alloy using a nonlinear ultrasonic technique. Scripta Materialia, 59(8):818–821, 2008.

23. Willems, H. and Dobmann, G.: Early detection of creep damage by ultrasonic and electromagnetic techniques. Nuclear Engineering and Design, 128(1):139–149, 1991.

24. Sposito, G., Ward, C., Cawley, P., Nagy, P. B., and Scruby, C.: A review of non-destructive techniques for the detection of creep damage in power plant steels. NDT and E International, 43(7):555–567, 2010.

25. Dobmann, G., Krning, M., Theiner, W., Willems, H., and Fie, U.: Nondestructive characterization of materials (ultrasonic and micromagnetic techniques) for strength and toughness prediction and the detection of early creep damage. NDT & E International, 30(5):326, 1997.

26. A. dos Santos, A. and Bray, D. E.: Comparison of Acoustoelastic Methods to Evaluate Stresses in Steel Plates and Bars. Journal of Pressure Vessel Technology, 124(3):354, 2002.

27. Ohtani, T., Ogi, H., and Hirao, M.: Evolution of microstructure and acoustic damping during creep of a Cr-Mo-V ferritic steel. Acta Materialia, 54(10):2705–2713, 2006.

28. Balasubramaniam, K., Valluri, J. S., and Prakash, R. V.: Creep damage characterization using a low amplitude nonlinear ultrasonic technique. Materials Characterization, 62(3):275–286, 2010.

29. Gómez Alvarez-Arenas, T., Riera-Franco de Sarabia, E., and Gallego-Juárez, J. A.: Ultrasonic evaluation of creep damage in steel. Ultrasonics, 31(3):155–159, 1993.

30. Ohtani, T.: Acoustic damping characterization and microstructure evolution during creep of a martensitic stainless steel. Zairyo/Journal of the Society of Materials Science, Japan, 56(2):114–120, 2007.

31. Stigh, U.: Influence of damage on ultrasonic velocity and strength - analysis and experiments. Engineering Fracture Mechanics, 28(1):1–12, 1987.

32. Hirao, M., Morishita, T., and Fukuoka, H.: Ultrasonic velocity change with creep damage in copper. Metallurgical Transactions A, 21(6):1725–1732, 1990.

33. Hurley, D. C., Balzar, D., and Purtscher, P. T.: Nonlinear ultrasonic parameter in quenched martensitic steels. MRS Proceedings, 591(9):4584–4588, 1999.

34. Gomez, T., Gallego, J., Riera, E., Martinez-Oña, R., and Lopez, V.: Ultrasonic Study of Damage Evolution on Creeped Steel. Ultrasonics International 91, 31(December):503–506, 1991.

35. Ogi, H., Hirao, M., and Aoki, S.: Noncontact monitoring of surface-wave nonlinearity for predicting the remaining life of fatigued steels. Journal of Applied Physics, 90(1):438–442, 2001.

36. Ohtani, T., Kawashima, K., Drew, M., and Guagliard, P.: Nonlinear acoustic evaluation of creep damage in boiler heat exchange tubes. Japanese Journal of Applied Physics, Part 1: Regular Papers and Short Notes and Review Papers, 46(7 B):4577–4582, 2007.

37. Cartz, L.: Nondestructive testing: radiography, ultrasonics, liquid penetrant, magnetic particle, eddy current. ASM International, 1995.

38. Hijazi, D. A.: Introduction to Non-Destructive Testing Techniques.

39. Jhang, K.-y.: Nonlinear Ultrasonic Techniques for Non- destructive Assessment of Micro Damage in Material : A Review. International Journal of Precision Engineering and Manufacturing, 10(1):123–135, 2009.

40. Birks, A. S., Green, R. E., and MacIntire, P.: ASNT Nondestructive Testing Handbook: Ultrasonic Testing. Nondestructive Testing Handbook, Vol 7. American Society for Nondestructive Testing, American Society for Metals, 1991.

41. North Central Collaboration for Education in Nondestructive Testing: NDT Resource Center.

42. Carlin, B.: Ultrasonics. Textbook Publishers, 2003.

43. Fei, D., Hsu, D. K., and Warchol, M.: Simultaneous velocity, thickness and profile imaging by ultrasonic scan. Journal of Nondestructive Evaluation, 20(3):95–112, 2001.

44. Smith, R. L.: Ultrasonic materials characterization. NDT International, 20(1):43–48, 1987.

45. Pruell, C., Kim, J.-Y., Qu, J., and Jacobs, L. J.: Evaluation of fatigue damage using nonlinear guided waves. Smart Materials and Structures, 18(3):035003 (7 pp.), 2009.

46. Cantrell, J. H. and Yost, W. T.: Nonlinear Ultrasonic Characterization of Fatigue Microstructures. International Journal of Fatigue, 23:487–490, 2001.

47. Cantrell, J. H. and Yost, W. T.: Effect of precipitate coherency strains on acoustic harmonic generation. Journal of Applied Physics, 81(7):2957–2962, apr 1997.

48. Barnard, D. J., Dace, G. E., Rehbein, D. K., and Buck, O.: Acoustic Harmonic Generation at Diffusion Bonds. Journal of Nondestructive Evaluation, 16(2):77–89, jun 1997.

49. Murnaghan, F. D.: Finite Deformations of an Elastic Solid. American Journal of Mathematics, 59(2):235–260, 1937.

50. Gedroits, A. and Krasilnikov, V.: Finite-amplitude elastic waves in solids and deviations from Hooke's law. Soviet Phys. JETP, 16(5):1122–1126, 1963.

51. Breazeale, M. A. and Ford, J.: Ultrasonic studies of the nonlinear behavior of solids. Journal of Applied Physics, 36(11):3486–3490, 1965.

52. Matlack, K. H., Bradley, H. A., Thiele, S., Kim, J.-y., Wall, J. J., Joon, H., Qu, J., and Jacobs, L. J.: Nonlinear ultrasonic characterization of precipitation in 17-4PH stainless steel. NDT and E International, 71:8–15, 2015.

53. Buck, O.: Nonlinear Acoustic Properties of Structural Materials — A Review. In Review of Progress in Quantitative Nondestructive Evaluation, eds. D. O. Thompson and D. E. Chimenti, volume 9, pages 1677–1684. Boston, MA, Springer US, 1990.

54. Lanza di Scalea, F., Rizzo, P., and Seible, F.: Stress measurement and defect detection in steel strands by guided stress waves. Materials in Civil Engineering, 15(3):219–227, 2003.

55. Chaki, S. and Bourse, G.: Stress level measurement in prestressed steel strands using acoustoelastic effect. Experimental Mechanics, 49(5):673–681, 2009.

56. Bartoli, I., Nucera, C., Srivastava, A., Salamone, S., Phillips, R., Lanza di Scalea, F., Coccia, S., and Sikorsky, C. S.: Nonlinear ultrasonic guided waves for stress monitoring in prestressing tendons for post-tensioned concrete structures. Proceedings of SPIE, 7292:729220–729220–11, 2009.

57. Gokhale, S.: Determination of Applied Stresses in Rails Using the Acoustoelastic Effect of Ultrasonic Waves. Doctoral dissertation, M.SC Thesis. Texas A &M University, 2007.

58. Javadi, Y., Akhlaghi, M., and Najafabadi, M. A.: Using finite element and ultrasonic method to evaluate welding longitudinal residual stress through the thickness in austenitic stainless steel plates. Materials & Design, 45:628–642, 2013.

59. Hughes, D. S. and Kelly, J. L.: Second-Order Elastic Deformation of Solids. Phys. Rev., 92:1145, 1953.

60. Abbasi, Z. and Ozevin, D.: Acoustoelastic Coefficients in Thick Steel Plates under Normal and Shear Stresses. Experimental Mechanics, 56(9):1559–1575, 2016.

61. Chaki, S., Corneloup, G., Lillamand, I., and Walaszek, H.: Combination of Longitudinal and Transverse Ultrasonic Waves for In Situ Control of the Tightening of Bolts. Journal of Pressure Vessel Technology-transactions of The Asme - J Pressure Vessel Technology, 129, 2007.

62. Dace, G., Thompson, R., Brasche, L., Rehbein, D., and Buck, O.: Nonlinear Acoustics, a technique to determine microstructural changes in materials. Quantitative Nondestructive Evaluation, 10B:1685–1692, 1991.

63. Qozam, H., Chaki, S., Bourse, G., Robin, C., Walaszek, H., and Bouteille, P.: Microstructure effect on the Lcr elastic wave for welding residual stress measurement. Experimental Mechanics, 50(2):179–185, 2010.

64. Castellano, A., Fraddosio, A., Marzano, S., and Daniele Piccioni, M.: Some advancements in the ultrasonic evaluation of initial stress states by the analysis of the acoustoelastic effect. Procedia Engineering, 199:1519–1526, 2017.

65. Kim, N. and Hong, M.: Measurement of axial stress using mode-converted ultrasound. NDT and E International, 42(3):164–169, 2009.

66. Sgalla, M. and Vangi, D.: A device for measuring the velocity of ultrasonic waves: An application to stress analysis. Experimental Mechanics, 44(1):85–90, feb 2004.

67. Buenos, A. A., Pereira, P., Mei, P. R., and dos Santos, A. A.: Influence of Grain Size on the Propagation of LCR Waves in Low Carbon Steel. Journal of Nondestructive Evaluation, 33(4):562–570, 2014.

68. Bray, D. E. and Egle, D. M.: Measurement of acoustoelastic and third-order elastic constants for rail steel. Acoustical Society of America, 60(3):741–744., 1976.

69. Johnson, G., C. Holt, A., and Cunningham, B.: Ultrasonic Ultrasonic Method for Determining Axial Stress in Bolts. Journal of Testing and Evaluation, 14:253–259, 1986.

70. Cantrell, J. H.: Substructural organization, dislocation plasticity and harmonic generation in cyclically stressed wavy slip metals. Proceedings of the Royal Society A: Mathematical, Physical and Engineering Sciences, 460(2043):757–780, 2004.

71. Cantrell, J. H.: Quantitative assessment of fatigue damage accumulation in wavy slip metals from acoustic harmonic generation. Philosophical Magazine, 86(11):1539–1554, 2006.

72. Kim, J.-Y., Qu, J., Jacobs, L. J., Littles, J. W., and Savage, M. F.: Acoustic Nonlinearity Parameter Due to Microplasticity. Journal of Nondestructive Evaluation, 25(1):28–36, mar 2006.

73. Salama, K.: Nondestructive ultrasonic characterization of two-phase materials. Technical report, 1987.

74. Rao, V. V. S. J., Kannan, E., Prakash, R. V., and Balasubramaniam, K.: Observation of two stage dislocation dynamics from nonlinear ultrasonic response during the plastic deformation of AA7175-T7351 aluminum alloy. Materials Science and Engineering A, 512:92–99, 2009.

75. Pruell, C., Kim, J. Y., Qu, J., and Jacobs, L. J.: Evaluation of plasticity driven material damage using Lamb waves. Applied Physics Letters, 91(23), 2007.

76. Shui, G., Wang, Y. S., and Gong, F.: Evaluation of plastic damage for metallic materials under tensile load using nonlinear longitudinal waves. NDT and E International, 55:1–8, apr 2013.

77. Breazeale, M. A. and Thompson, D. O.: Finite-amplitude ultrasonic waves in aluminum. Applied Physics Letters, 3(5):77–78, 1963.

78. Kim, J.-Y., Jacobs, L. J., Qu, J., and Littles, J. W.: Experimental characterization of fatigue damage in a nickel-base superalloy using nonlinear ultrasonic waves. Journal of the Acoustical Society of America, 120(3):1266–1273, sep 2006.

79. Xiang, Y., Deng, M., Liu, C. J., and Xuan, F. Z.: Contribution of mixed dislocations to the acoustic nonlinearity in plastically deformed materials. Journal of Applied Physics, 117(21), 2015.

80. Walker, S. V., Kim, J. Y., Qu, J., and Jacobs, L. J.: Fatigue damage evaluation in A36 steel using nonlinear Rayleigh surface waves. NDT and E International, 48:10–15, jun 2012.

81. Zeitvogel, D. T., Matlack, K. H., Kim, J.-Y., Jacobs, L. J., Singh, P. M., and Qu, J.: Characterization of stress corrosion cracking in carbon steel using nonlinear Rayleigh surface waves. In 39th Annual Review of Progress in Quantative Nondestructive Evaluation (AIP Conf. Proc. 1511), volume 32, pages 144–152, mar 2013.

82. Lim, H. J., Song, B., Park, B., and Sohn, H.: Noncontact fatigue crack visualization using nonlinear ultrasonic modulation. NDT and E International, 73:8–14, 2015.

83. Nucera, C. and Lanza Di Scalea, F.: Nonlinear wave propagation in constrained solids subjected to thermal loads. Journal of Sound and Vibration, 333(2):541–554, jan 2014.

84. Viswanath, A., Rao, B. P. C., Mahadevan, S., Parameswaran, P., Jayakumar, T., and Raj, B.: Nondestructive assessment of tensile properties of cold worked AISI type 304 stainless steel using nonlinear ultrasonic technique. Journal of Materials Processing Technology, 211(3):538–544, mar 2011.

85. Evans, R. W., Wilshire, B., and of Metals, I.: Creep of Metals and Alloys. Book (Institute of Metals). Institute of Metals, 1985.

86. Hardesty, F.: Creep and fatigue in high temperature alloys. Journal of Mechanical Working Technology, 8(4):373–374, 1983.

87. Dobrzański, J.: Internal damage processes in low alloy chromium-molybdenum steels during high-temperature creep service. Journal of Materials Processing Technology, 157-158(SPEC. ISS.):297–303, 2004.

88. Sklenička, V., Kuchaová, K., Svoboda, M., Kloc, L., Buršík, J., and Kroupa, A.: Long-term creep behavior of 9-12%Cr power plant steels. Materials Characterization, 51(1):35–48, 2003.

89. Nabarro, F. R. N. and de Villiers, F.: Physics Of Creep And Creep-Resistant Alloys. CRC Press, 2018.

90. Smallman, R. E. and Ngan, A. H. W.: Modern Physical Metallurgy. Oxford, UNITED KINGDOM, Elsevier Science & Technology, 2013.

91. Kassner, M. E.: Fundamentals of Creep in Metals and Alloys. Elsevier Science, 2015.

92. Pelleg, J.: Creep in ceramics. Solid Mechanics and its Applications, 241(i):41–61, 2017.

93. Ashby, M.: A first report on deformation-mechanism maps. Acta Metallurgica, 20(7):887 – 897, 1972.

94. Porter, D. A., Easterling, K. E., and Sherif, M.: Phase Transformations in Metals and Alloys (Revised Reprint). CRC Press, 2009.

95. Singulani, A. P.: Advanced Methods for Mechanical Analysis and Simulation of Through Silicon Vias. Doctoral dissertation, Technischen Universität Wien, 2014.

96. MOTT, N. F.: Dislocations, Work-Hardening and Creep. Nature, 175:365, feb 1955.

97. Herring, C.: Diffusional Viscosity of a Polycrystalline Solid. Journal of Applied Physics, 21(5):437–445, 1950.

98. Mott, N. F. and Nabarro, F. R. N.: Dislocation Theory and Transient Creep, Report of a Conference on the Strength of Solids. In Phys Soc London, volume 1, 1948.

99. Hosford, W. F.: Mechanical Behavior of Materials. Cambridge University Press, 2009.

100. Chang, H. C. and Grant, N. G.: Mechanism of intercrystalline fracture. Trans. Am. Inst. Min. Metall. Eng., (206):544–551, 1956.

101. Sharpe, R. S.: Research Techniques in Nondestructive Testing. Number v. 6 in Research Techniques in Nondestructive Testing. Academic Press, 1982.

102. Prasad, R. and Kumar, S.: Study of the influence of deformation and thermal treatment on the ultrasonic behaviour of steel. Journal of Materials Processing Tech., 42(1):51–59, 1994.

103. Palanichamy, P., Vasudevan, M., Jayakumar, T., Venugopal, S., and Raj, B.: Ultrasonic velocity measurements for characterizing the annealing behaviour of cold worked austenitic stainless steel. NDT and E International, 33(4):253–259, 2000.

104. Salinas, V., Aguilar, C., Espinoza-González, R., Lund, F., and Mujica, N.: In situ monitoring of dislocation proliferation during plastic deformation using ultrasound. International Journal of Plasticity, 97:178–193, 2017.

105. Hikata, A. and Elbaum, C.: Generation of ultrasonic second and third harmonics due to dislocations. I. Physical Review, 144(2):469–477, 1966.

106. Granato, A. and Lücke, K.: Theory of mechanical damping due to dislocations. Journal of Applied Physics, 27(6):583–593, jun 1956.

107. Koehler, J. S.: Imperfections in nearly perfect crystals. New York, Wiley, 1952.

108. S. Razvi, P. Li, K. S.: Nondestructive characterization of Aluminum Alloys. pages 259–279, 1987.

109. Salama, K.: Nondestructive ultrasonic characterization of engineering materials. Technical report, 1985.

110. Zhang, J. F., Xuan, F.-Z., Xiang, Y. X., and Yang, F. Q.: Non-linear ultrasonic response of plastically deformed aluminium alloy AA 7009. Materials Science and Technology, 29(11):1304–1309, 2013.

111. Espinoza, C., Feliú, D., Aguilar, C., Espinoza-González, R., Lund, F., Salinas, V., and Mujica, N.: Linear Versus Nonlinear Acoustic Probing of Plasticity in Metals: A Quantitative Assessment. Materials, 11(11), 2018.

112. Lugo, M., Jordon, J., Horstemeyer, M., Tschopp, M., Harris, J., and Gokhale, A.: Quantification of damage evolution in a 7075 aluminum alloy using an acoustic emission technique. Materials Science and Engineering: A, 528(22-23):6708–6714, 2011.

113. ASTM: Standard Test Methods for Tension Testing of Metallic Material. i:1–28, 2013.

114. ASTM International: ASTM B221-14 Standard Specification for Aluminum and Aluminum-Alloy Extruded Bars, Rods, Wire, Profiles, and Tubes., 2014.

115. N.I.H. ImageJ: Image processing and analysis in Java, 2017.

116. Liu, S., Croxford, A. J., Neild, S. A., and Zhou, Z.: Effects of experimental variables on the nonlinear harmonic generation technique. IEEE Transactions on Ultrasonics, Ferroelectrics, and Frequency Control, 58(7):1442–1451, jul 2011.

117. Freitas, V. L. d. A., de Albuquerque, V. H. C., Silva, E. d. M., Silva, A. A., and Tavarese, J. M. R.: Nondestructive characterization of microstructures and determination of elastic properties in plain carbon steel using ultrasonic measurements. Materials Science and Engineering A, 527(16-17):4431–4437, 2010.

118. Badidi Bouda, A., Lebaili, S., and Benchaala, A.: Grain size influence on ultrasonic velocities and attenuation. NDT and E International, 36(1):1–5, 2003.

119. Carreon, H., Ruiz, A., Medina, A., Barrera, G., and Zarate, J.: Characterization of the alumina-zirconia ceramic system by ultrasonic velocity measurements. Materials Characterization, 60(8):875–881, 2009.

120. Ahn, B., Seok Lee, S., Taik Hong, S., Chul Kim, H., and Kang, S.-J. L.: Application of the acoustic resonance method to evaluate the grain size of low carbon steels. NDT & E International, 32(2):85–89, 1999.

121. Badidi Bouda A., Benchaala, A., and Alem, K.: Ultrasonic characterization of materials hardness. Ultrasonics, 38(1-8):224–7, 2000.

122. Murthy, G. V., Sridhar, G., Kumar, A., and Jayakumar, T.: Characterization of intermetallic precipitates in a Nimonic alloy by ultrasonic velocity measurements. Materials Characterization, 60(3):234–239, 2009.

123. Grayeli, N. and Kino, G. S.: Effect of Grain Size and Preferred Crystal Texture on Acoustic Properties of 304 Stainless Steel. (October 1979), 1981.

124. Ahn, B. and Lee, S. S. L.: Effect of microstructure of low carbon steels on ultrasonic attenuation. IEEE transactions on ultrasonics, ferroelectrics, and frequency control, 47(3):620–9, 2000.

125. Gür, C. H. and Kele, Y.: Ultrasonic characterisation of hot-rolled and heat-treated plain carbon steels. Insight: Non-Destructive Testing and Condition Monitoring, 45(9):615–620, 2003.

126. Papadakis, E.: Ultrasonic attenuation and velocity in three transformation products in steel. Journal of applied physics, 35(5):1474–1482, 1964.

127. Heyman, J. S., Allison, S. G., and Salama, K.: Influence of Carbon content on higher order ultrasonic properties in steels. Ultrasonic Symposium, pages 991–994, 1983.

128. Allison, S. G., Heyman, J. S., and Salama, K.: Ultrasonic Measurement of Residual Deformation Stress in Thin Metal Plates Using Surface Acoustic Waves. In 1983 Ultrasonics Symposium, IEEE, pages 995–999, 1983.

129. Standard Specification for High-Strength Low-Alloy Columbium-Vanadium Structural Steel, 2015.

130. Mangonon, P. L.: The Principles of materials selection for engineering design. Prentice Hall, 1998.

131. Abbasi, Z., Cunningham, M., and Ozevin, D.: The Quantification of Errors in the Measurement of Nonlinear Ultrasonics. SAE Conference, Michigan, 2015.

132. Krauss, G.: Martensite in steel: strength and structure. Materials Science and Engineering: A, 273-275:40–57, 1999.

133. El Rayes, M. M., El-Danaf, E. A., and Almajid, A. A.: Characterization and correlation of mechanical, microstructural and ultrasonic properties of power plant steel. Materials Characterization, 100:120–134, 2015.

134. Gür, C. H. and Tuncer, B. O.: Investigating the microstructure-ultrasonic property relationships in steels. 16th WCNDT-World Conference on NDT, 2004.

135. Hakan Gür, C. and Tuncer, B. O.: Characterization of microstructural phases of steels by sound velocity measurement. Materials Characterization, 55(2):160–166, 2005.

136. Shi, F., Michaels, J. E., and Lee, S. J.: In situ estimation of applied biaxial loads with Lamb waves. Journal of the Acoustical Society of America, 133(2):677–687, 2013.

137. Bråthe, L.: Macroscopic measurements of creep damage in metals. Stand. J. Metal, 7:199–203, 1978.

138. Stigh, U., Jansson, S., Bråthe, L., and Dyne, A.: Ultrasonic measurement of creep damage in steel. Revue d'acousrique, 66:202–204, 1983.

139. Berthaud, Y.: Etude des possibilités de mesure de l'endommagement par des techniques ultrasonores, 1983.

140. Ohtani, T., Ogi, H., and Hirao, M.: Dislocation damping and microstructural evolutions during creep of 2.25Cr-1Mo steels. Metallurgical and Materials Transactions A, 36(February):411–420, 2005.

141. Burke, E., Ashbaugh, N., Sathish, S., Freed, S., and Rosenberger, A.: A precursor for fatigue damage in a Nickel-based superalloy. jan 2005.

142. Jaya Rao, V. V. S., Kannan, E., Prakash, R. V., and Balasubramaniam, K.: Fatigue damage characterization using surface acoustic wave nonlinearity in aluminum alloy AA7175-T7351. Journal of Applied Physics, 104(12):123508, dec 2008.

143. Yost, W. T. and Cantrell, J. H.: The effects of fatigue on acoustic nonlinearity in aluminum alloys. In IEEE 1992 Ultrasonics Symposium Proceedings, pages 947–955 vol.2, 1992.

144. Campos-Pozuelo, C., Vanhille, C., and Gallego-Juarez, J.: Nonlinear Elastic Behavior and Ultrasonic Fatigue of Metals. jan 2006.

145. Xiang, Y., Zhu, W., Liu, C.-J., Xuan, F.-Z., Wang, Y.-N., and Kuang, W.-C.: Creep degradation characterization of titanium alloy using nonlinear ultrasonic technique. NDT & E International, 72:41–49, 2015.

146. Tsai, M. C., Chiou, C. S., Du, J. S., and Yang, J. R.: Phase transformation in AISI 410 stainless steel. Materials Science and Engineering A, 332(1-2):1–10, 2002.

147. Polar, A., Indacochea, J. E., Wang, M. L., Singh, V., and Lloyd, G.: Measurement and Microstructural Evaluation of Creep-Induced Changes in Magnetic Properties of a

410 Stainless Steel. Journal of Engineering Materials and Technology, 126(4):392, 2004.

148. American Society of Testing Materials: ASTM A240 Standard Specification for Chromium and Chromium-Nickel Stainless Steel Plate, Sheet and Strip for Pressure Vessels and for General Applications. ASTM International, I:12, 2004.

149. Chakraborty, G., Das, C., Albert, S., Bhaduri, A., Thomas Paul, V., Panneerselvam, G., and Dasgupta, A.: Study on tempering behaviour of AISI 410 stainless steel. Materials Characterization, 100:81–87, 2015.

150. Methods, S. T.: Standard Test Methods for Conducting Creep , Creep-Rupture , and Stress-Rupture. Order A Journal On The Theory Of Ordered Sets And Its Applications, (August 2000), 2003.

151. ASTM International: ASTM E3-11(2017) Preparation of Metallographic Specimens 1. Area, 03(July):1–17, 2001.

152. Garofalo, F.: Fundamentals of creep and creep-rupture in metals. Macmillan series in materials science. Macmillan, 1965.

VITA

NAME: Niloofar Nabili Tehrani

EDUCATION:

Ph.D., Materials Engineering,
University of Illinois at Chicago, Chicago, IL, United States, 2019

B.Sc., Materials & Metallurgical Engineering,
Iran University of Science and Technology, Tehran, Iran, 2014.

PROFESSIONAL EXPERIENCE:

Part-time Faculty - Instructor of ENGR 325 - Materials Engineering, Loyola University Chicago, Chicago, IL, Jan 2019 - May 2019

Research and Development Intern, ArcelorMittal Global R&D, East Chicago, IN, May 2018 - August 2018.

Graduate Research Assistant, NSF Funded project, UIC, Chicago, IL, June 2015 - June 2018.

Teaching Assistant for the CME 260/261 - Properties of Materials/Materials for Manufacturing, UIC, Chicago, IL, (2015-2016, 2016-2017, 2017-2018, 2018-2019).

Laboratory Instructor, CME 470 - Physical and Mechanical Properties of Materials, UIC, Chicago, IL, (Fall 2017).

Laboratory Instructor, CME 480 - Welding Metallurgy, UIC, Chicago, IL, (Fall 2018).

PUBLICATIONS:

N. Tehrani, Z. Abbasi, D. Ozevin, and J. E. Indacochea. Metallurgical Characterization of a Low-carbon Steel Microstructure Using Linear and Nonlinear Ultrasonics, 2019, Journal of Materials Engineering and Performance, Under Review

Tehrani, N., Abbasi, Z., Mostavi, A., Kamali, N., Ozevin, D., Chi, Sh.W. and Indacochea, J. E.: Creep damage detection in 410 Stainless Steel with nonlinear ultrasonic test, 2019, Under Preparation

Mostavi, A. , Kamali, N.,Tehrani, N., Indacochea, E.,Ozevin, D. and Chi, Sh.W. : A wavelet-based harmonics decomposition of ultrasonic signal in assessment of plastic strain in aluminum, Measurements Journal, 2017.

Abbasi, Z., Yuhas, D., Zhang L., Basantes, A., Tehrani, N., Ozevin, D., and Indacochea, J.E.: "The Detection of Burn-Through Weld Defects Using Noncontact Ultrasonics." Materials 2018, 11(1), 128.

Kamali, N., Tehrani, N., Mostavi, A., Ozevin, D., Chi, Sh.W. and J.E. Indacochea: "Influence of Mesoscale and Macroscale Heterogeneities in Metals on Higher Harmonics Under Plastic Deformation", Journal of Nondestructive Evaluation, 38(2):1–13, 2019.

Gattu, V. K., Ebert, W. L., Tehrani, N., Indacochea, J. E. (2018, July 20). Electrochemical Measurements of Steel Corrosion for Modeling H2Generation. NACE International.

AWARDS: Chancellors Student Service and Leadership Award

EXTRACURRICULAR ACTIVITIES:
Grad SWE UIC Vice-President, 2019
Grad SWE UIC President and Founder of WEMENTOR (mentorship program at UIC), 2018
Grad SWE UIC Co-Founder, 2017
GSC CME Department Co-Representative, 2016